Heterogeneous Ice Nucleation by Biomolecules

By

SARAH ALSALHI

H. H. Wills Physics Laboratory
UNIVERSITY OF BRISTOL

A dissertation submitted to the University of Bristol in accordance with the requirements of the award of degree DOCTOR OF PHILOSOPHY in the Faculty of Science.

DECEMBER 2022

Word count: c. 31717

ABSTRACT

In recent research, the role of biomolecules in heterogeneous ice nucleation has gained prominence, as they serve as models for atmospheric ice nucleating agents. While established methods for biomolecule synthesis exist, distinguishing ice nucleation efficiencies from their oligomers poses challenges. This study demonstrates that the constant cooling rate approach is inadequate for accurately assessing Apoferritin subforms' ice nucleation rates due to data uncertainties. Isothermal measurements are employed to differentiate ice nucleating efficiencies of Apoferritin subforms using serial-diluted samples. Furthermore, this approach extends to investigating the ice nucleating efficiency of DNA origami tiles, a novel biomolecular model. By fitting data to classical nucleation theory (CNT), plausible model parameters are derived for both Apoferritin and DNA origami tiles. Finite element simulations are used to explore the influence of temperature gradients on isothermal freezing rates inside droplets of varying characteristics. Frozen fraction analysis of microlitre and nanolitre droplets highlights Apoferritin oligomers as the most effective ice nucleation particles (INPs), followed by dimers and monomers. Determining CNT parameters for each Apoferritin subform was challenging due to data ambiguities. However, through isothermal measurements, CNT parameters for each Apoferritin subform are successfully determined such as the free energy barrier constant, kinetic factor, and shape factor. These parameters show Apoferritin clusters as the most efficient subform, attributed to their complex shape, which contains active sites like pores, cavities, and a larger surface area. Isothermal measurements further confirm that DNA origami tiles have a higher ice nucleation efficiency over Apoferritin dimers and monomers due to their larger surface area and smaller contact angle with water. Notably, factors such as droplet volume, contact angle with the substrate, and cooling rate should be considered for an accurate freezing rate depiction; neglecting them leads to skewed results. With an increase in these factors, the measured isothermal freezing rate also increases over time, requiring more time for droplets to achieve a uniform inner temperature. In conclusion, isothermal measurements are a valuable tool for distinguishing ice nucleation efficiencies, even for mixed molecules like Apoferritin subforms. DNA origami tiles emerge as efficient INPs, holding promise as intriguing candidates for future ice nucleation research, particularly in designing tailored INPs for focused studies.

AKNOWLEDGMENTS

I would like to express my thanks to my kind and patient supervisor Prof. Walther Schwarzacher. Throughout my PhD project, Walther provided continuous encouragement and was always eager and happy to assist in any way he could. The meetings and discussions motivated me to consider issues from various angles in order to provide a thorough and objective analysis.

I would like to express my sincere gratitude to PNU Scholarships, Princess Norah Bint Abdulrahman University, for their generous financial support of the research project.

I would like to thank our University of Oxford collaborators, Jonathan Bath and Andrew Turberfield for supplying us with the DNA Origami samples.

Finally, I'd like to express my gratitude to my family for the unending enthusiasm and unwavering support they've shown me during this journey.

AUTHOR'S DECLARATION

I declare that the work in this dissertation was carried out in accordance with the requirements of the University's Regulations and Code of Practice for Research Degree Programmes and that it has not been submitted for any other academic award. Except where indicated by specific reference in the text, the work is the candidate's own work. Work done in collaboration with, or with the assistance of, others, is indicated as such. Any views expressed in the dissertation are those of the author.

SIGNED: *Sarah Alsalhi.* DATE: *17/12/2022*

TABLE OF CONTENTS

LIST OF TABLES

LIST OF FIGURES

1. THEORETICAL FRAMEWORK

1.1. Introduction

In the past several decades, research into the processes that lead to the formation of ice from liquid water has gained significant attention. Many different areas of study, such as those dealing with food, cell, and organ preservation, have begun to focus on it. Furthermore, studies are being carried out into the effects of freezing on aircraft wings, as well as how freezing could damage pipes and cables [1–4]. However, in terms of ice in the atmosphere, nucleation has attracted the greatest focus and study effort, with the goal of improving our knowledge of how clouds form and how that affects the amount of precipitation they produce. Ice nucleation is especially significant in mixed phase clouds since in these clouds supercooled water droplets can exist and the transformation of water into ice take place, at temperatures ranging from 0 to –38 ºC [5–7]. This is intriguing since ice nucleation in this temperature range requires ice nucleating agents (INAs), also known as ice nucleation particles (INPs), to commence freezing.

The atmospheric system includes an abundance of aerosol particles that serve as cloud condensation nuclei (CCN) or INPs, despite the fact that INPs are rare and scarce in comparison to CCNs. Cloud glaciation is seasonally and geographically dependent on the quantity of INPs present [8]. In general, these particles can be divided into two categories: inorganic INPs and organic INPs. Examples of inorganic INPs include mineral dusts, volcanic ash, and silver iodide, whereas organic INPs include both proteinaceous and non-proteinaceous particles, such as bacteria, fungi, and pollen. Nonetheless, it is still not clear exactly what properties of an aerosol, such as its surface characteristics or micro/nano size, make it a strong INP. In contrast to organic aerosols, the significance of inorganic aerosols as INPs has been actively studied in recent years [9,10]. Therefore, further experimental effort should be devoted to comprehending the role and contribution of organic aerosols as INPs in the atmosphere [11,12]. This thesis will be dedicated to researching the effectiveness of proteins and DNA as INPs, two important examples of INPs that are helpful for understanding the process of ice nucleation caused by organic aerosols.

1.2. Review on Ice Nucleation Particles

Mineral dust particles are among the factors that can have a significant impact on the ice nucleation mechanism of mixed clouds. The investigation of immersion freezing ice nucleation in various mineral dust types indicated that characteristics such as particle size, composition, and surface area significantly impact their ice nucleation efficiency [13]. The aerosol concentration in the atmosphere, as well as temperature, humidity, and dust particle coatings also affect mineral dust ice nucleation efficiency [14]. According to recent studies, both mineral dust surrogates and mineral dusts mixed with sulfate can nucleate ice at temperatures comparable to those found in cirrus clouds [15,16]. Similarly, Atkinson et al. highlighted the importance of feldspar, a common component of mineral dusts, as an efficient INP, likely due to its crystal structure providing specific nucleation sites [17]. Moreover, specific regions on the feldspar surface were observed to exhibit higher ice nucleation efficiency compared to other areas. These regions included specific crystal facets, surface defects, or chemical functional groups, which provided suitable environments for ice crystal formation due to their unique atomic arrangements or interactions with water molecules [18]. It is also reported that the proteins produced by some fungus can act as additional sites for ice nucleation when they adhere to the surfaces of mineral dust [19]. K-feldspar also greatly influences ice nucleation compared to quartz in dust samples, indicating its importance in atmospheric ice formation [14,20]. The role of mineral dust particles in cloud processes and precipitation, generated during the development of hailstorms, was investigated. The results suggest that mineral dust particles play a dual function as a CCN and an INP, promoting the formation of cloud droplets and ice crystals [21].

Silver iodide (AgI) is widely used as a prevalent ice nucleating agent. Studies have shown that AgI demonstrates remarkable ice nucleation efficiency and has been investigated for its potential use in cloud seeding and modifying precipitation processes. Marcolli et al. provide crucial insights for developing efficient cloud seeding strategies and comprehending AgI's influence on cloud microphysics and precipitation phenomena [22]. Atomistic and coarse-grained simulations conducted by Roudsari et al. examined how different geometries, such as slits and wedges, affect nucleation efficiency when present on the surfaces of AgI particles. The results showed an increase in ice nucleation activity, confirming the importance of the surface morphology of the INP in enhancing the nucleation process [23].

Recent studies have focused on the effect of graphene oxide (GO), a non-biological substance, on ice nucleation amid the importance of this process in a wide range of natural and industrial processes. For example, GO nanosheets served as effective ice nucleating agents, reducing the critical nucleus size and promoting ice nucleation [24]. Investigation of the size of nanoscale domains on inhomogeneous surfaces like GO determined that their size significantly influences ice nucleation efficiency, with smaller domains displaying greater ice nucleation activity [25]. In a separate investigation, researchers explored the ice efficiency of both graphene and graphene oxides, concluding that GO exhibited notable ice nucleation capabilities, surpassing pristine graphene [26]. The nucleation of ice on the surface of graphite in the presence of nanoparticles was examined, providing insights into the ice nucleation behaviour of related carbon-based materials [27]. Sequential surface modification of GO and its impact on ice nucleation were studied by Biggs et al., showing that sequential modifications of GO could lead to a controlled and tunable ice nucleation behaviour [28]. Furthermore, a study on heterogeneous ice nucleation by graphene nanoparticles demonstrated that graphene-based nanoparticles have the ability to induce ice nucleation [29].

Sea spray aerosols are tiny airborne particles formed when ocean waves break and burst into the air, releasing droplets and bubbles. These aerosols contain various components, including water, salt, organic matter, and other substances present in the seawater. Sea spray aerosols play a crucial role in Earth's climate system as they influence cloud formation and can impact the radiative balance of the atmosphere. Schill and Tolbert studied several important physical and chemical properties that are relevant to ice nucleation in simulated sea-spray aerosols. Some of these properties include the morphology and size distribution of the aerosol particles, as well as the composition and arrangement of the chemical components on the aerosol surfaces. The research also explored the influence of various chemical species present in the aerosols, such as salts and organic matter, on their ice nucleation efficiency using Raman microscopy [30]. For instance, one study investigated the heterogeneous ice nucleation of Prochlorococcus (marine organic aerosol) and indicated that variations in seawater biogeochemistry have a direct impact on the ice nucleation efficiency of these aerosols, highlighting the complex interplay between oceanic processes and cloud formation [31,32]. The mixed surfactants within sea spray aerosols were observed to trigger ice nucleation, even in environments abundant in fatty alcohols. Furthermore, salt concentration plays a role in this process, as the addition of salts to water suppresses freezing [33]. The significance of supermicron-sized particles (larger INPs) plays a crucial role in initiating ice nucleation in the

atmosphere, serving as efficient ice nuclei and contributing to the early stages of sea spray formation [34]. Sea salt aerosols were found to be effective INPs in cirrus clouds [35]. Seasonal and geographical variations in ice-nucleating particles were observed by Wilbourn et al. and significant ice nucleation activity was found in marine aerosols during late spring [36]. To identify and quantify INPs present in sea spray aerosols, Alpert et al. developed a comprehensive multimodal freezing model that considers various factors such as the composition of sea spray aerosols, the presence of INPs, and the interactions between these agents and aerosol particles [37].

Soot, a type of fine particles emitted during the incomplete combustion of carbon-containing materials, is important in cloud formation and climate [38]. Ice nucleation studies have shown that soot particles can efficiently nucleate ice in the lower troposphere through deposition mode [38]. Moreover, their ice nucleation ability is significantly influenced by the presence of sulfuric acid coatings [39]. During cloud processing, soot particles undergo numerous transformations, including condensation, coagulation and chemical reactions with cloud droplets or ice crystals. These transformations can contribute to alterations in the size, shape, and composition of soot particles, ultimately enhancing their ice nucleation efficiency [40]. Moreover, the number of soot particles emitted by aircraft engines can influence the formation and ice nucleation properties of contrails (ice clouds formed from aircraft exhaust emissions). This relationship was further investigated through simulated contrail processing to understand its effects on the ice nucleation efficiency of soot particles. In addition, changes in the organic content of the soot particles were examined, indicating alterations in their ability to nucleate ice [41]. A study found that all soot types lack ice nucleation below water saturation in mixed-phase clouds ($T > -38.15$ ºC). However, in cirrus clouds ($T \leq -38.15$ ºC), ice nucleation varies with particle size and soot properties. Soot aggregates with mesopores and low water-soot contact angles nucleate ice through a pore condensation and freezing modes, thereby influencing the microphysics of ice clouds. On the other hand, soot particles without appropriate cavities or with high contact angles initiate ice only when the relative humidity levels necessary for homogeneous freezing are reached or exceeded [42].

Fungal spores have gained attention as important ice nucleating particles. Some studies explored the ice nucleation ability of specific fungal spores, such as Cladosporium and Alternaria, as potential contributors to ice crystal formation in the atmosphere [43]. The results showed that these fungal spores have the ability to nucleate ice, possibly involving ice nucleation active proteins or other surface structures as nucleation sites for ice growth [43]. Urediospores of rust fungi were also identified as INPs, potentially influenced by the presence of ice nucleation active bacteria [44]. On the other hand, certain airborne fungal spores were found to lack ice nucleation activity, introducing variability among species [45]. The investigation also expanded to different fungal classes, including agaricomycetes, ustilaginomycetes, and eurotiomycetes, unravelling their ice nucleation ability and implications for atmospheric transport [46]. Further, a study specifically focused on Mortierella alpina spores and observed their ice nucleation activity at low temperatures, possibly due to ice nucleating proteins [47]. The significance of nanoscale biological fragments, including fungal spores, as INPs in clouds was highlighted [48]. Some studies simulated the influence of fungal spores, like Cladosporium sp. and Mortierella alpina, on cloud microphysics. Despite their high ice nucleation activity at elevated subzero temperatures, their overall impact on cloud ice formation is relatively minor due to their low atmospheric concentrations. However, under specific conditions, such as cloud top temperatures below 15 °C and in the absence of other INPs, these fungal spores can influence the cloud ice phase and contribute to a limited number of ice crystals [49]. Polytrichum commune spores exhibited ice nucleation ability, potentially facilitated by associated microorganisms [50]. Huang et al. provided an overview of biological INPs that included a discussion on the significance of fungal spores as potential contributors to ice formation in the atmosphere [12].

Ice nucleation by pollen has also been studied in atmospheric research. Laboratory studies have been conducted to investigate pollen's ice nucleating ability in various freezing modes, including deposition and condensation freezing [51], as well as later contact and immersion freezing [52]. The research has been expanded to include more pollen types, such as birch, hazel, and pine, in immersion and contact freezing modes [53]. Suspendable macromolecules have been identified as ice nucleation agents in birch and conifer pollen [54], and ice-nucleating and ice-binding polysaccharides have been found in boreal pollen [55]. Recent research has demonstrated that macromolecules extracted from pollen act as ice nucleating cryoprotectants. These macromolecules serve a dual function by protecting pollen during freezing conditions and facilitating ice nucleation. The presence of such cryoprotectants on the surface of pollen

grains promotes ice formation, making pollens effective INPs under appropriate freezing conditions [56]. Moreover, Matthews et al. focused on exploring pollen emissions, particularly subpollen or pollen grains, and their role as ice nucleation aerosols [57].

Ice nucleation by antifreeze proteins (AFPs) is a complex process with contrasting behaviours as both ice growth inhibitors and ice nucleation promoters [58]. These proteins play a crucial role in low-temperature preservation processes, contributing to the preservation of biological materials under freezing conditions [59]. In natural environments, ice nucleation and anti-nucleation processes mediated by AFPs have significant implications for the formation of ice crystals and their impact on various ecological [60]. AFPs have been shown to have essential physiological functions in animals, particularly in their adaptation to cold environments [61]. Certain AFPs (type I) have been found to enhance ice nucleation at specific concentrations, further highlighting their role in ice formation [62]. The mechanisms through which AFPs interact with ice surfaces involve a range of anchored clathrate and ice-like patterns [63]. However, AFPs can also exhibit a Janus effect, showing both ice nucleation inhibition and promotion, depending on their concentrations. The Janus effect is a unique and intriguing phenomenon where AFPs play a dual role in ice nucleation processes [64]. This behaviour adds an extra layer of complexity to the understanding of ice-binding proteins and has significant implications for applications, such as cryopreservation, agriculture, and atmospheric science.

Ice nucleation by bacteria, especially Pseudomonas species, has been a subject of growing interest due to its implications in atmospheric processes and biotechnological applications. Pseudomonas syringae ice crystallization has been studied since the 1970s [65]. Pseudomonas syringae, a bacterial species widely found on plant surfaces, has the ability to nucleate ice at relatively warm temperatures, above –2 °C, which is higher than typical ice nucleation temperatures observed in other biological systems [66]. In subsequent studies, research in cloud simulation chambers has shown that bacteria, including Pseudomonas, exhibit ice nucleation activity when present as aerosols in simulated cloud-like environments [67]. Ice active strains of Pseudomonas syringae are found to be diverse and abundant in natural aquatic environments, particularly with a significant presence found in freshwater lakes [68]. Analysis of ice nucleation active bacteria extracted from 23 precipitation events in Virginia, USA, unveiled their prevalence within the Pseudomonadaceae, Enterobacteriaceae, and Xanthomonadaceae families, using a membrane-bound ice nucleation protein. A unique heat-resistant molecule in

Lysinibacillus was also found among these bacteria suggesting a potential role for these bacteria in initiating precipitation events [69]. The ice nucleation protein InaZ from Pseudomonas syringae was studied [70]. InaZ240, with five 48-residue repeat units, acts as an elongated ellipsoid with minimal ice-binding compared to anti-freeze proteins. However, InaZ fragments with more repeat units display pH-dependent changes in shape [70,71]. Moreover, Pseudomonas syringae strain R10.79, isolated from rainwater, demonstrates resilience against various atmospheric stress factors, including temperature fluctuations, desiccation, and UV radiation [72]. Recent research has found that specific ion-protein interactions can enhance or inhibit the ice nucleation ability of Pseudomonas. For example, weakly hydrated anions such as perchlorate were observed to alter the conformation of ice nucleation protein units, affecting their functionality. Similarly, sulfate ions have been shown to influence the reorientation of water at ice-binding sites in antifreeze proteins [73]. In addition, the interaction between the ice nucleating protein InaZ induces structural ordering in the adjacent water network, resulting in increased order as the temperature approaches the melting point of water [74,75].

Various research has investigated the role of viruses as INPs, such as detecting viruses with ice nucleating potential in snow samples collected from Greece [76]. Additionally, investigations into their impact on cloud glaciation revealed their potential as INPs [77], and heat test methods demonstrated their ice nucleating abilities similar to certain minerals [78]. A separate study highlighted the prevalence of viral INPs in colder regions near the Western Antarctic Peninsula, suggesting their critical role in ice nucleation processes in cold environments and potential contribution to polar cloud formation and precipitation [79].

In the field of ice nucleation research, a growing body of evidence supports the notion that the efficiency of INPs is linked to the presence of specialized active sites on their surfaces. These active sites refer to specific regions or sites that exhibit a strong affinity for ice nucleation, acting as nucleation centres for the formation of ice crystals from water vapor [80]. The unique chemical and physical properties of these active sites play a pivotal role in reducing the energy barrier required for ice nucleation, thereby enhancing the ice-forming ability of the particles [81]. Furthermore, the surface morphology and geometry of INP are critical factors that determine the ice nucleation efficiency [82]. For example, the micro- and nanoscale characteristics of the surface can profoundly affect how particles interact with water vapor, influencing the probability of ice nucleation [83]. Surface roughness, topographical irregularities, and crystallographic orientations all contribute to the availability and

accessibility of active sites, further influencing the ice nucleation process [84]. Understanding how active sites and surface morphology interact is vital for advancing our knowledge of ice nucleation mechanisms. This knowledge is not only relevant in atmospheric science, where ice nucleation significantly impacts cloud formation and climate dynamics, but also in material engineering, where controlling ice nucleation is crucial for designing anti-icing coatings, cryopreservation techniques, and other applications [85]. Moreover, by unravelling the underlying principles that govern ice nucleation on INP surfaces, researchers can explore innovative strategies to engineer materials with tailored ice nucleation properties [86]. This involves creating better ice-resistant materials for enhanced performance and safety in industries like aviation, power generation, and transportation [87].

Nanoparticles provide a controlled and tunable experimental platform, making it possible to study factors affecting ice nucleation, like size, shape, and surface chemistry. This allows for creating innovative materials for various applications, such as cloud seeding, ice templating in materials synthesis, and cryopreservation techniques. For instance, inorganic nanoparticles, such as the kaolin-iron oxide composite (KaFe), demonstrated effective reactions with aqueous mercury salts, which result in the formation of highly efficient INPs named HgKaFe. These particles induced freezing of water at higher temperatures ranging from −6.6 to −4.7 °C [88]. Other inorganic nanoparticles, including iron oxide, silicon oxide, and magnesium oxide, have also exhibited ice nucleation ability via the deposition mode. Notably, amorphous Fe_2O_3 particles were found to be highly efficient ice nucleators. These particles were effective in forming cirrus clouds in the upper troposphere but were less active in tropospheric mixed-phase clouds above −40 ºC. Also, the contact angles observed in the high-latitude mesosphere could reduce their ability to initiate ice formation in that region [89]. Gold nanoparticles have potential as models for ice-nucleating particles (INPs). Researchers investigated ice nucleation in colloidal solutions containing gold nanoparticles (Au NPs) using low-temperature environmental transmission electron microscopy. The results demonstrate dynamic interactions between Au NPs and the crystallizing ice front, offering valuable insights into their role in ice nucleation processes [90].

Biomolecules, particularly proteins, provide interesting models for ice nucleation particles (INPs) compared to inorganic ones. Proteins are responsible for some of the significant ice nucleation efficiency of INPs, as they become adsorbed on the surface of certain mineral dust particles and are involved in the ice nucleation activities of fungal spores and Pseudomonas bacteria. In contrast, the lack of well-defined surfaces in inorganic INPs creates challenges in investigating their ice nucleation ability, often relying on probabilities and making reproducibility difficult. Proteins, however, provide a wealth of synthesis methods through recombinant DNA methods, chemical synthesis and cell-based expression systems, enabling the production of complex proteins with precise sequences and modifications [91]. Furthermore, the purification of proteins employs established techniques like chromatography, ultracentrifugation, and electrophoresis, ensuring the isolation of highly pure proteins and using specific protein-ligand interactions for selective purification. Protein characterization methods, including spectroscopy (UV-Vis, fluorescence, circular dichroism), mass spectrometry, X-ray crystallography, and NMR spectroscopy, provide comprehensive structural and functional insights [92,93]. Additionally, the possibility of protein modification allows for the introduction of specific functionalities [94–96]. On the contrary, the synthesis, purification, and characterization of inorganic NPs present greater challenges due to their varied physicochemical properties and the absence of inherent biological functionalities.

In a recent and intriguing study by M. Cascajo-Castresana et al. [97], they found that common proteins, including Ferritin, Apoferritin, casein, ovalbumin, hydrophobins, and a yeast ice-binding protein, displayed ice-nucleating activity at –10 ºC, with horse spleen Ferritin and Apoferritin exhibiting significant activity at –5 ºC. The ice-nucleating activity of Apoferritin was linked to specific misfolded cage monomers or oligomers. Furthermore, the researchers employed Dynamic Light Scattering (DLS) to identify distinct freezing ranges based on the location of ice-nucleating sites on aggregates or misfolded structures. In their conclusion, M. Cascajo-Castresana et al. summarized that ice nucleation is a prevalent characteristic of diverse proteins, regardless of their function, and may arise due to misfolding or aggregation. Building on this work, our study aims to extend their investigations by exploring the immersion freezing ice nucleation of Apoferritin subforms, such as oligomers, dimers, and monomers, which serve as Ice Nucleating Particle (INP) models purified using size exclusion chromatography (SEC) method. To achieve this, we will employ constant cooling rate (temperature ramp) and isothermal measurements, a valuable yet less commonly used method, to compare results and identify the ice nucleation efficiencies of each Apoferritin subform.

In recent studies, the ice nucleation properties of non-proteinaceous biomolecules, including DNA and RNA, have become a subject of significant interest. These nucleic acids have demonstrated ice nucleation activity, with freezing temperatures spanning from –19 to –26 °C [98]. In our investigation, we aim to evaluate the ice nucleation efficiency of DNA origami tiles in chapter 5, both in its annealed and unannealed states, to understand how different conformations impact its ice nucleating properties. By systematically studying the ice nucleation behaviour of DNA origami, we hope to shed light on its potential as a novel and highly controllable ice nucleating particle.

1.3. Classical Nucleation Theory

1.3.1. Homogenous Nucleation

A century ago, the foundations of a theoretical framework for the crystallisation process were developed as the well-known classical nucleation theory (CNT) by pioneers such as Volmer, Weber, Farkas, and Zeldovich [99]. CNT aims to explain, in general, the appearance of embryos (nuclei) of a new phase in the parent phase during a first-order phase transition [100]. Supercooling water below its melting point (0 °C), for instance, will result in the formation of ice nuclei. The driving force behind nucleation is the chemical potential difference $\Delta\mu$ between the metastable phase (parent phase) and the newly transitioned phase (nucleus) [1]. The chemical potential difference $\Delta\mu$ is a thermodynamic quantity that depends on the amount of supercooling ΔT and can be written as [100]:

$$\Delta\mu = H_m \frac{\Delta T}{T_m} \qquad (1-1)$$

where H_m is the enthalpy per molecule, T_m is the melting temperature, $\Delta T = (T_m - T)$ is the supercooling and T is the temperature.

The chemical potential difference is proportional to the supercooling. When the supercooling is large and positive, the thermodynamic driving force $\Delta\mu$ increases, hence raising the probability of nucleation [101].

In thermodynamics, the direction of a process like nucleation is dictated by the change in the system's Gibbs free energy, ΔG. Gibbs energy is equal to the difference between the change in enthalpy ΔH_m and the product of entropy ΔS of a system and the temperature ($\Delta G = \Delta H_m - T\Delta S$). If $\Delta G < 0$, a process can occur spontaneously; in other words, when ΔG is negative, nucleation is thermodynamically favourable. In contrast, if $\Delta G > 0$, the process will not be spontaneous and is thermodynamically unfavourable.

According to CNT, homogeneous nucleation takes place in the absence of INPs, hence the probability of forming a critical nucleus is the same throughout the parent phase [1]. A crystal nucleus is a cluster of particles (atoms or molecules) of the crystallised phase that are packed together with a specific overall volume [99]. For simplicity, the nucleus is assumed to be spherical. Although it is possible to assume other geometrical shapes, the spherical shape is simpler and, unlike other shapes, can be specified by a single key variable, the radius r, since

the sphere is an isotropic shape in space. The bulk free energy ΔG_V of the nucleus is given by [1]:

$$\Delta G_V = -\frac{4}{3}\pi r^3 \rho \Delta\mu \qquad (1-2)$$

where ρ is the density number of the nuclei.

ΔG_V is negative, indicating that the change in Gibbs free energy is likewise negative and that the nucleation process is favourable in the bulk system. The value of ΔG_V is proportional to the nucleus's cubed radius and the extent of supercooling, ΔT. However, the formation of a crystal nucleus also necessitates the formation of a surface that separates the nucleus phase from the metastable parent phase. The process of creating a nucleus surface requires energy and is given by the interfacial free energy change ΔG_s, where:

$$\Delta G_S = 4\pi r^2 \gamma_s \qquad (1-3)$$

here γ_s is the surface free energy per unit area between the parent and nucleus phases.
In summary, there is a competition between the bulk (negative) and interfacial (positive) free energies, resulting in an overall Gibbs free energy change ΔG_{tot} as shown in figure (1-1). By combining equations (2) and (3), the nucleation Gibbs free energy equation is [1,99–101]:

$$\Delta G_{tot} = \Delta G_S + \Delta G_V \qquad (1-4)$$

$$\Delta G_{tot} = 4\pi r^2 \gamma_s - \frac{4}{3}\pi r^3 \rho\, \Delta\mu \qquad (1-5)$$

The total Gibbs free energy varies with respect to the radius of the nucleus as shown in figure (1-1). The maximum point of the curve is referred to as the critical energy barrier ΔG^*, which corresponds to a radius value known as the nucleus critical radius r_c; both are key factors in CNT.

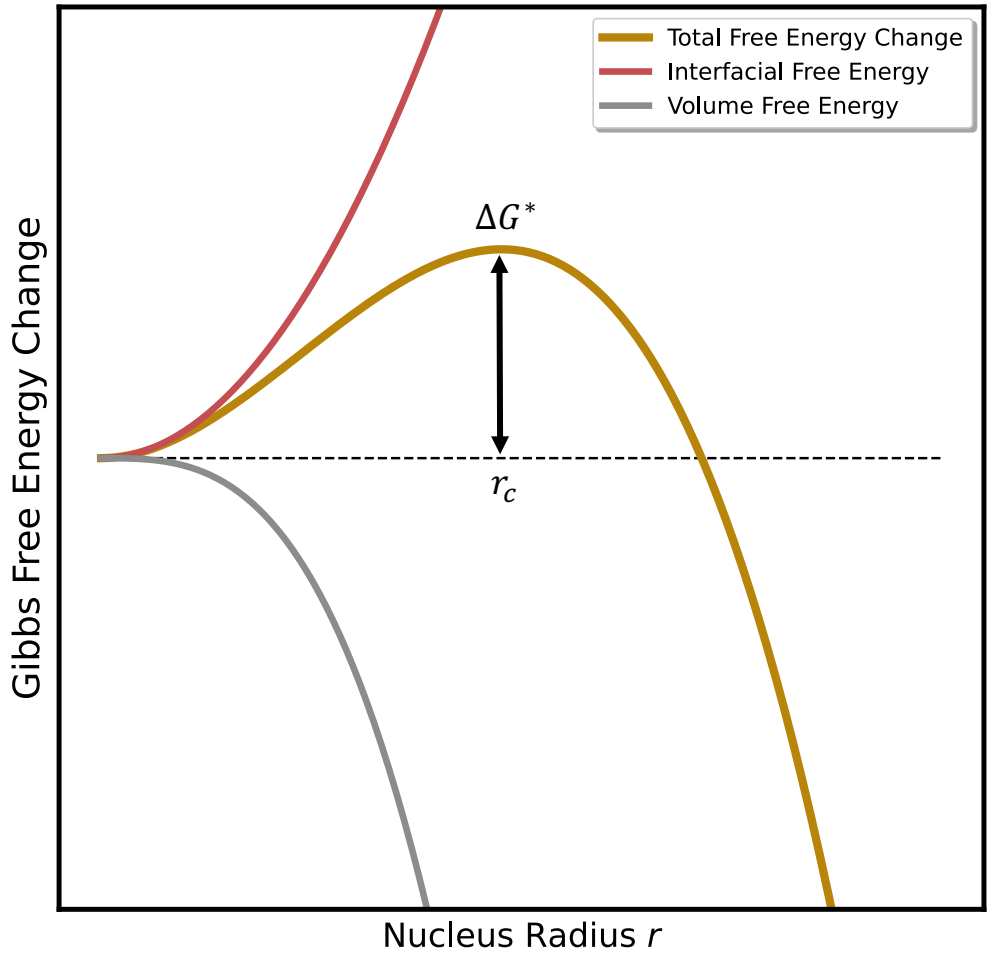

Figure 1-1: The Gibbs free energy profile according to classical nucleation theory (CNT) as a function of the nucleus radius under constant temperature and pressure. The nucleation process involves both bulk and interfacial free energy. The contribution of bulk free energy to total free energy is negative, whereas the energy required to create the nucleus' surface is positive. The critical radius of a nucleus, r_c, corresponds to the critical energy barrier ΔG^* that must be overcome by the system in order to form stable crystal nuclei.

When $r < r_c$, the probability of a nucleus surviving and progressing toward the critical radius is low [100,101]. In contrast, when $r > r_c$, the nucleus radius and size will increase spontaneously, as ΔG_{tot} will be reduced due to the dominance of bulk free energy. The critical nucleation barrier and radius can be obtained by differentiating equation 5 with respect to r:

$$\frac{d(\Delta G_{tot})}{dr} = 0 \qquad (1-6)$$

giving [1,99–101] :

$$\Delta G^* = \frac{16\pi}{3}\frac{\gamma_s^3}{\rho^2\Delta\mu^2} \qquad (1-7)$$

and:

$$r_c = -\frac{2\gamma_s}{\rho\Delta\mu} \qquad (1-8)$$

equation 7 represents the critical nucleation barrier ΔG^*, which is the energy or the work needed to be overcome by a crystal nucleus in order to form a new crystalline phase, where it is mathematically equivalent to the maximum point (peak) where the tangent line gradient of this point is zero, equation 6.

Equation 7 and 8 are under the assumption of constant temperature and pressure. Given how the chemical potential difference $\Delta\mu$ depends on the amount of supercooling, equation 1, ΔT is inversely proportional to the critical radius:

$$r_c \propto -\frac{1}{\Delta T} \qquad (1-9)$$

As seen from figure (1-2), a significant amount of supercooling decreases the critical radius and minimises the activation energy (ΔG^*) needed for the formation of a stable nucleus, whereas low supercooling causes an increase in (ΔG^*) [1].

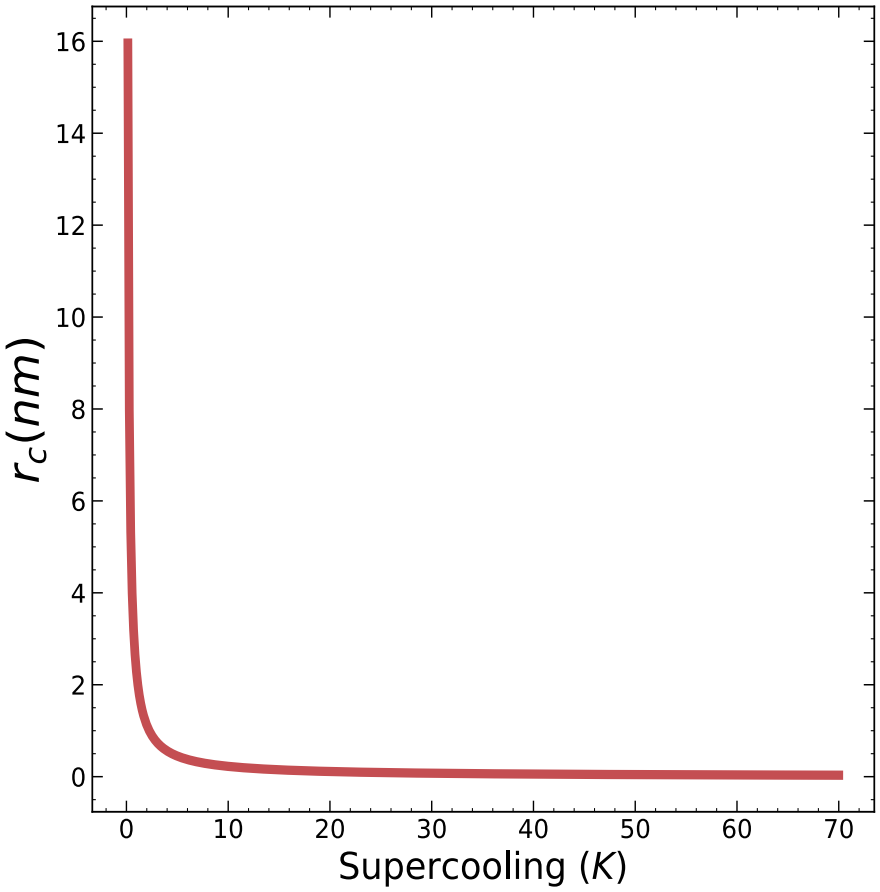

Figure 1-2: The relationship between the critical radius r_c and the amount of supercooling ΔT below the melting point. The critical radius reduces as the amount of supercooling increases.

1.3.2. Nucleation Rate

So far, we have used classical nucleation theory to describe the nucleation process with thermodynamic variables such as the change in the system's Gibbs free energy. CNT also considers the kinetics of the nucleation process. The nucleation rate of a system that is supercooled below its melting point gives the number of critical nuclei formed per unit volume per unit time:

$$J = J_0 \exp\left(-\frac{\Delta G^*}{k_B T}\right) \qquad (1-10)$$

where k_B is the Boltzmann constant and J_0 is the kinetic prefactor.

J is the steady state nucleation rate for homogenous nucleation and is a function of temperature [99,102,103]. When the supercooling is significant, the nucleation barrier is reduced, thereby

increasing the probability of forming a critical nucleus and, consequently, the nucleation rate. However, significant supercooling slows the kinetics of the system's particles, so reducing their mobility to attach to a nucleus so their diffusion. As a result, this will also limit the system's nucleation rate. The kinetic prefactor J_0 can be expressed as follows:

$$J_0 = N_0\, \phi \tag{1 – 11}$$

$$\phi = 4\pi r_c\, n_s\, A\, Z \tag{1 – 12}$$

where N_0 is the number of nucleation sites per unit volume. ϕ is the transfer rate of atoms or molecules into the nucleus, n_s is the number of parent phase molecules around the nucleus surface, $4\pi r_c$. A is the attachment frequency of an atom or molecule to a nucleus, which is related to the capability of these particles to diffuse across a supercooled system and is given by [1,99,102,104]:

$$A = \frac{k_B T}{h} \exp\left(-\frac{\Delta g^*}{k_B T}\right) \tag{1 – 13}$$

here, h is Plank's constant, Δg^* is an activation energy required for a molecule to diffuse across the parent phase-nucleus boundary. Δg^* it is a temperature dependent quantity, as it increases as the temperature decreases. Z is the Zeldovich factor that corresponds to the probability of nuclei shrinking or reaching the critical radius, it determines the non-equilibrium state of the nucleation process and ranges from 10^{-2} to 1, where 1 represents an equilibrium state, it is given by [104–106]:

$$Z = \frac{1}{n^*}\sqrt{\frac{\Delta G^*}{3\pi k_B T}} \quad , \; n^* = \frac{4}{3}\pi\, \rho\, r_c^3 \tag{1 – 14}$$

where $n^*$is number of atoms or molecules in the critical nucleus.

1.3.3. Heterogenous Nucleation

In nature, nucleation does not occur homogeneously due to the scarcity of impurity-free systems; rather, it occurs heterogeneously around contaminants and defects, meaning that the probability of a critical nucleus forming is not equal across the supercooled system. When nucleation happens in the presence of a foreign particle, such as INPs, the Gibbs free energy

of the system decreases; this is referred to as heterogeneous nucleation in CNT. This energy reduction depends on the so-called shape factor $f(\theta)$, and is given by [1,99–104]:

$$\Delta G_{het} = \Delta G_{hom} . f(\theta) \qquad (1-15)$$

The shape factor has a value between $0 \leq f(\theta) \leq 1$ and depends on the wettability between the substrate and the newly formed nucleus. θ is the nucleus-to-foreign particle contact angle that determines the degree of wetting and is determined by the equilibrium of interfacial energy between three different phases, as shown in figure (1-3) a. It is given by Young's surface tension equation [1,99–104]:

$$\text{Cos}\,\theta = \frac{\gamma_{ls} - \gamma_{cs}}{\gamma_{cl}} \qquad (1-16)$$

where γ_{ls}, γ_{cs} and γ_{cl} are the surface energies of liquid phase (l), foreign substrate (s) and crystalline phase (c), respectively.

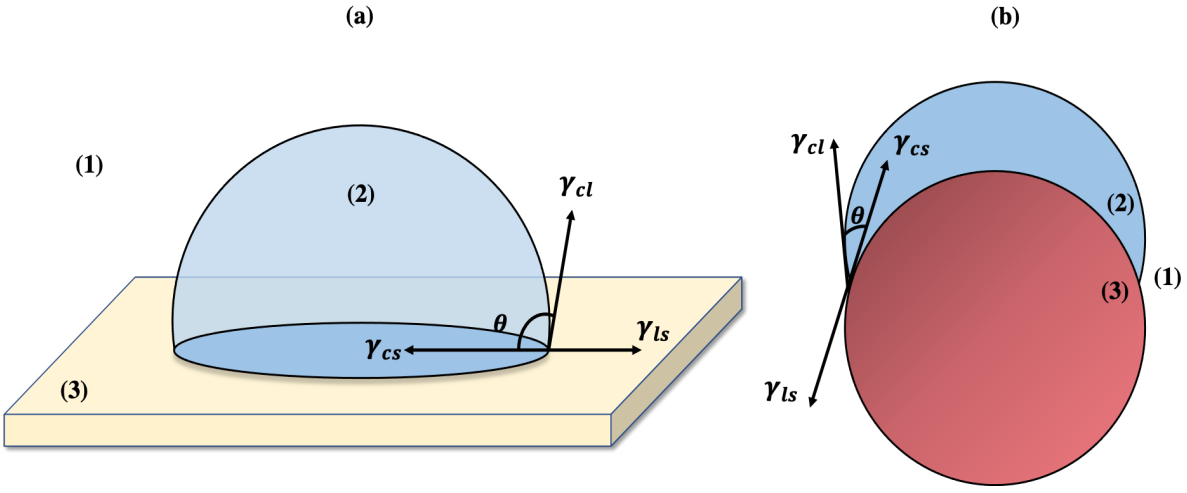

Figure 1-3: Heterogeneous nucleation contact angle between the critical nucleus and the surface of the foreign particle. Using Young's equation, the contact angle can be determined when the surface tension equilibrium is reached between the (1) liquid phase (l), (2) the crystalline phase (c), and (3) the foreign particle substrate (s). (a) is a flat substrate. (b) is a curved substrate e.g. a spherical particle.

As shown in figure (1-4), heterogeneous nucleation has a lower energy barrier than homogeneous nucleation. Also, in heterogeneous nucleation, the nucleus is considered to be a spherical cap instead of a whole sphere, despite the fact that critical radius is the same for both types of nucleation.

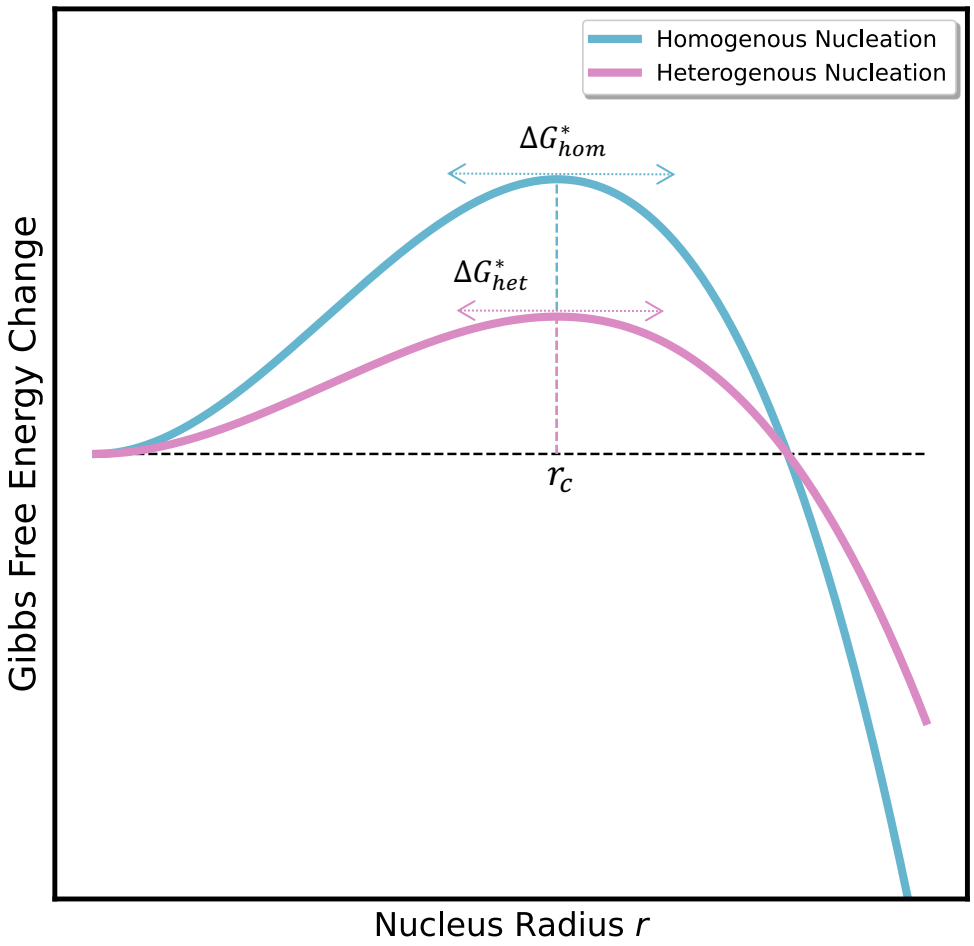

Figure 1-4: Comparison of homogeneous and heterogenous nucleation free energy barriers. Due to the presence of foreign particles that promote the nucleation process, the energy barrier for heterogeneous nucleation is lower than the barrier for homogeneous nucleation despite that the critical radius is the same.

If it is assumed that the foreign substrate's surface, where nucleus formation initiates, is flat (a) in figure (1-3), the nucleation shape factor is given by [107]:

$$if: \quad m = \cos\theta$$

$$f(m) = \frac{(2+m)(1-m)^2}{4} \qquad (1-17)$$

Figure (1-5) illustrates the relationship in equation 17 of the shape factor as a function of the contact angle between the nucleus and the foreign particle. Small contact angles imply higher interaction between the nucleus and the nucleator, hence effectively promoting nucleation (low activation energy), while large contact angles suggest poor interaction and an activation energy that is very near to the homogeneous nucleation case, $\theta \approx 180°$.

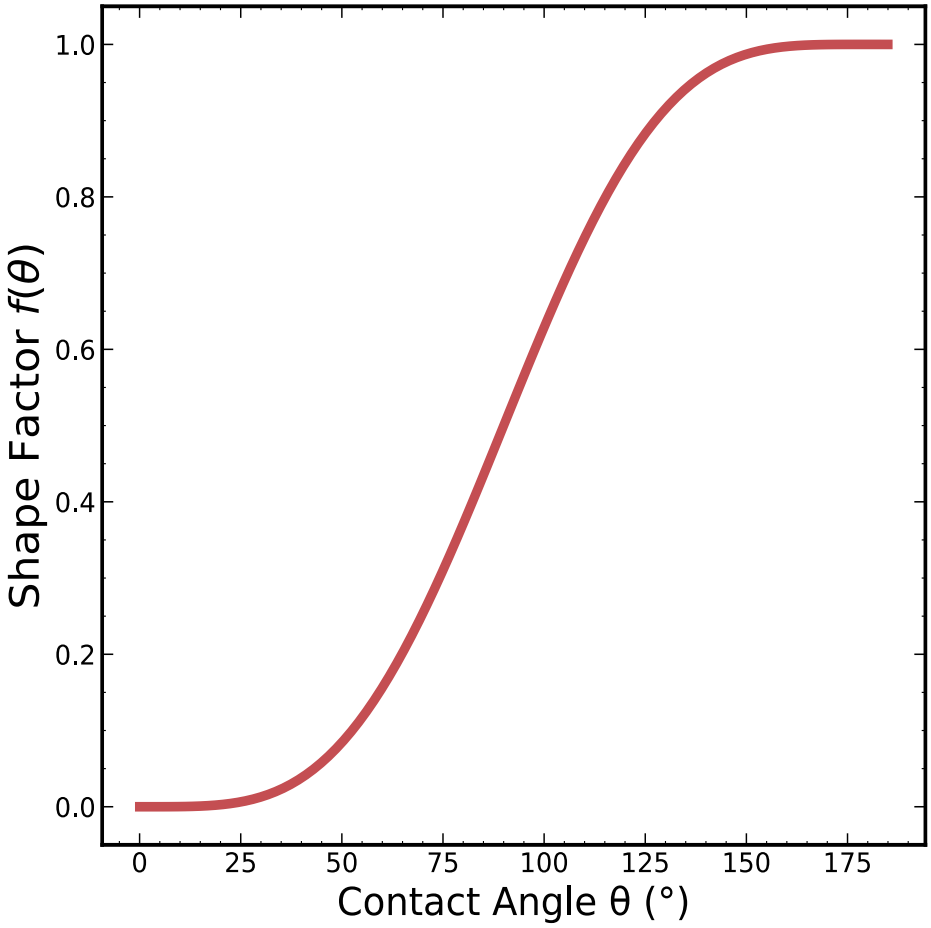

Figure 1-5: Heterogeneous nucleation shape factor $f(\theta)$ as a function of the contact angle of a flat foreign particle under the assumption that the critical nucleus is a spherical cap. It ranges from 0 to1, since smaller contact angles indicate a more effective INP, while at greater contact angles the nucleation process converges on homogeneous nucleation.

Thus, the shape factor of a flat surface indicates the difference between the homogeneous and heterogeneous nucleation energy barriers. It also indicates how much the volume of the spherical nucleus, V_{sphere} , decreased relative to the volume of the spherical cap, V_{cap}, and can be expressed as:

$$f(m) = \frac{\Delta G^*_{het}}{\Delta G^*_{hom}} = \frac{V_{cap}}{V_{sphere}} \qquad (1-18)$$

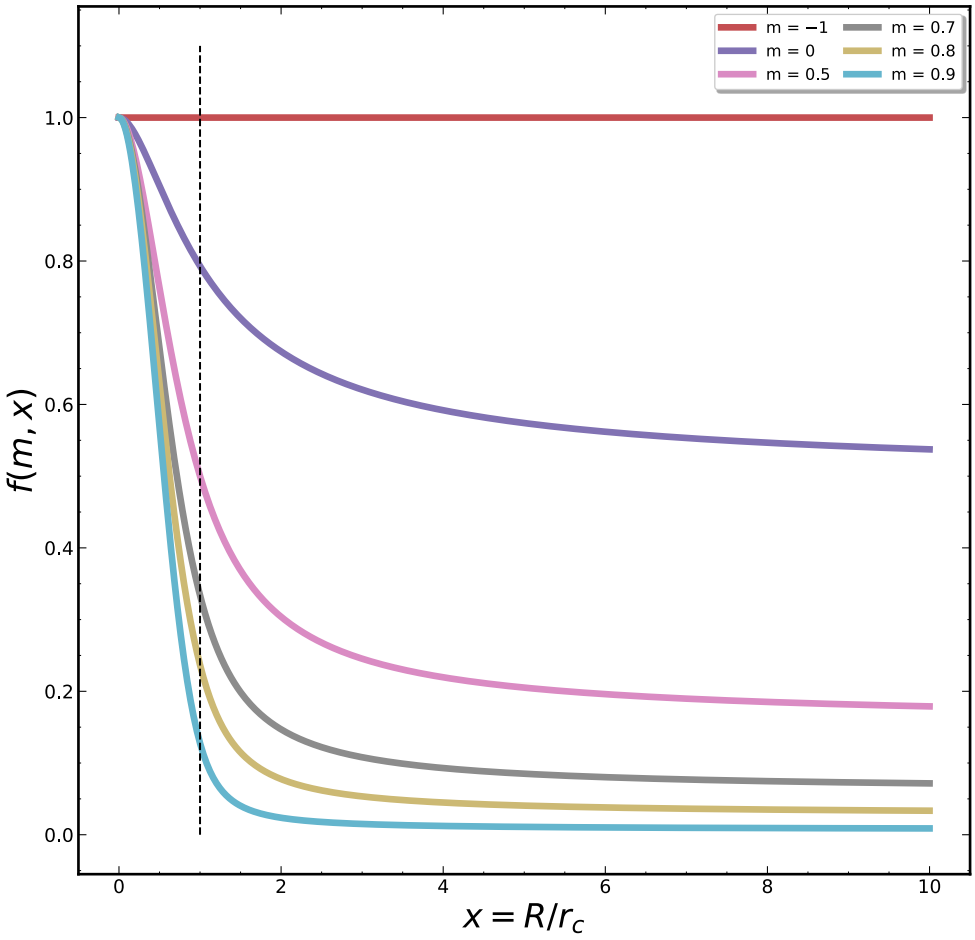

Figure 1-6: Demonstration of Fletcher's shape factor equation for a curved surface nucleator and various contact angles θ, as a function of the radius ratio x between the nucleator radius and critical nucleus radius. The dashed line indicates $x = \frac{R}{r_c} = 1$.

In classical nucleation theory, the effectiveness of a nucleator is determined by its ability to lower the activation energy barrier, which is controlled by its shape factor. Fletcher derived a formula for the shape factor for a curved rather than a flat nucleator, such as the spherical particle in figure (1-3) b, in terms of the contact angle and the relative ratio (x) of the nucleator radius (R) to the critical radius (r_c) as follows [108,109]:

$$when: \quad x = \frac{R}{r_c} \quad and \quad d = (1 + x^2 - 2mx)^{\frac{1}{2}} \qquad (1-19)$$

$$f(m,x) = \frac{1}{2} + \frac{1}{2}\left(\frac{1-mx}{d}\right)^3 + \frac{1}{2}x^3\left[2 - 3\left(\frac{x-m}{d}\right) + \left(\frac{x-m}{d}\right)^3\right] + \frac{3}{2}mx^2\left(\frac{x-m}{d} - 1\right) \qquad (1-20)$$

As with $f(m)$, $f(m,x)$ has a range between 0 and 1; figure (1-6) shows $f(m,x)$ for different m values as a function of x. At $m = -1, (\theta = 180°)$, the nucleator has no influence on the free energy barrier and $f(m,x) = 1$ for all values of x . In this case the nucleation barrier is equal to that for homogeneous nucleation [101,108,109]. The nucleator efficiency becomes significant when $\theta < 180°$ as then the nucleus wets the nucleator particle and $f(m,x) < 1$ which lowers the energy barrier of nucleation. If $x \gg 1$ the radius of curvature of the foreign particle becomes less important and it can be treated as a flat surface [101,108,109]. Conversely, when $x \leq 1$, the radius of the critical nucleus is greater than the nucleator radius and the foreign particles are unable to decrease the activation energy significantly; this is referred to as the zero-size effect by X. Liu et al. since the energy barrier again approaches that for homogeneous nucleation [101,110]. Equation 20 can be considered a generic shape factor formula since it can account for both curved and flat nucleator surfaces.

The heterogenous nucleation rate can be expressed in terms of the shape factor as follows:

$$J_{het} = J_0 \exp\left(-\frac{[\Delta G^*_{hom} \cdot f(m,x)]}{k_B T}\right) \qquad (1-21)$$

1.3.4. Limitation of Classical Nucleation Theory

Classical nucleation theory (CNT) is a theoretical framework that has provided a reasonable representation of the nucleation process. In spite of this, it has limitations. Nucleation occurs on an atomic or molecular scale where physical quantities such as interfacial energy, density, and contact angle could be different from on a macroscopic scale [1,8,99]. For heterogeneous

nucleation, the contact angle and particle size are the only variables used to describe an INP; nevertheless, the complexity of the nucleator makes it difficult to generalise these two variables to all types of INPs [5,8]. Nevertheless, classical nucleation theory is still able to provide adequate explanations for experimental results, mainly the nucleation rate.

1.4. Ice Nucleation Experimental models

Heterogeneous ice nucleation in general can be described by four fundamental modes, each of which exhibits a specific physical interaction between the ice nucleation particle (INP) and water or water vapour (parent phase). Deposition ice nucleation occurs from a supersaturated vapour surrounding an INP without the formation of liquid water [5]. Contact freezing describes the process whereby ice is formed when INPs collide with droplets of supercooled water [5]. Immersion freezing as the name implies, nucleation takes place as a result of total immersion of the INP in a supercooled liquid droplet [5,111]. The main focus of this work will be on this mode. The last mode is condensation freezing, in which the vapour condenses into liquid water and then freezes; this model could be important for porous INPs.
[8,111,112].

Measuring the ice nucleation efficiency of an INP for immersion freezing is often done by cooling small samples of equal size, such as water droplets containing the INP, below the melting point of water (0 ^{o}C). The efficiency of INPs is assessed from the temperature and length of time needed for an array of droplets to freeze. However, real samples often cannot be described by a single nucleation rate. The reason for this is variation in the nucleator properties and their distribution in the droplets. For instance, a single INP is believed to have specific regions on its surface that initiate ice nucleation; these regions are known as active sites. Nevertheless, little is known about the nature of these active sites and whether or not all nucleators of one type have identical active sites with the same density and distribution on the INP surface. Moreover, INPs with different nucleating efficiency may be distributed differently among the observed droplets [5,111]. Yet, the two models most commonly used to describe measurements are the singular (deterministic) and stochastic (time-dependent) models [113].

1.4.1. Singular (Deterministic) Model

In this approach, a specific freezing temperature is assigned to each active site. This is convenient when dealing with a complicated environment such as atmospheric clouds, which can contain organic and inorganic INPs with a wide spectrum of ice nucleating efficiency, size, and active sites. In this model, the time-dependent aspect of ice nucleation is given less weight. The cumulative number of ice active sites per unit surface area between water melting point and temperature T, can be expressed as [114]:

$$n_s(T) = -\int_0^T k(T)\, dT \qquad (1-22)$$

where $k(T)$ is the number of active sites per unit temperature. So, to relate $n_s(T)$ to experimental data, the frozen fraction, $F_{ice}(T)$ is given by [8,111,113]:

$$F_{ice}(T) = \frac{N_{frozen}(T)}{N_{total}} = 1 - \exp(-n_s(T)\, s) \qquad (1-23)$$

where $N_{frozen}(T)$ is the cumulative number of frozen droplets at temperature T, N_{total} is the total number of droplets, and s is surface area. The frozen fraction can also be expressed by, $K(T)$, the cumulative number of active sites per unit droplet volume V , as follows [115]:

$$F_{ice}(T) = \frac{N_{frozen}(T)}{N_{total}} = 1 - \exp(-K(T)\, V) \qquad (1-24)$$

If the mass concentration C_m, mass per unit liquid volume, is known $K(T)$ is given by [8,111,113]:

$$K(T) = N_m(T)\, C_m \qquad (1-25)$$

here $N_m(T)$, is the number of active sites per unit mass. $K(T)$ also, can be given by the number of active sites per particle $N_n(T)$ when the particle's concentration per liquid volume C_n is known, as follows [8,111,113]:

$$K(T) = N_n(T)\, C_n \qquad (1-26)$$

1.4.2. Stochastic (Time-Dependent) Model

The stochastic approach in heterogeneous ice nucleation could be represented as a first-order kinetics process, since the number of unfrozen droplets decreases with time at a given temperature. A well-known example of a first-order kinetic process is radioactive decay. The nucleation process can be described using the Poisson distribution, in which each successful nucleation event is independent of the prior successful nucleation events. The probability of x nucleation events occurring during a time interval Δt with a mean nucleation rate R, is given by [17,20]:

$$P_x(t) = \frac{(R.t)^x}{x!} e^{-Rt} \qquad (1-27)$$

To obtain the probability of droplets remaining liquid or having zero nucleation events, $x = 0$, throughout a period of time, Eq 28 will be [17,20]:

$$P_0(t) = e^{-Rt} \qquad (1-28)$$

The exponential decay function can be related to the unfrozen fraction of time-dependent measurements as follows [17,20]:

$$P_0(t) = \frac{N_L}{N_{tot}} = e^{-Rt} \qquad (1-29)$$

N_L, N_{tot} are the number of unfrozen droplets and total droplets, respectively. R is the central focus of the stochastic method, since it can be constant or variable depending on the homogeneity of the INPs and their distribution among the examined droplets. When droplets are of uniform size and contain the same distribution of INPs, the mean freezing rate R remains constant with time, as shown in figure (1-7) a, b. The plot of log $(\frac{N_L}{N_{tot}})$ versus time is a straight line and the slope value corresponds directly to the value of R. In contrast, when droplets are heterogeneous, meaning they contain INPs with different efficiencies and distributions, as indicated by the colours in figure (1-7) c, the log $(\frac{N_L}{N_{tot}})$ will not be linear but rather curve due to the multiple freezing rates of the droplets, as droplets with effective INPs would freeze faster as shown in figure (1-7) d. This is a common example in the atmospheric system.

To determine the mean freezing rate of heterogeneous droplets, consider dividing them into subgroups, such as $a, b, c, \ldots\ldots$, with respective freezing rates $R_1, R_{2,}, R_3, \ldots\ldots$, during a time interval t, the total unfrozen fraction can be expressed as follows:

$$\frac{N_L}{N_{tot}} = a\, e^{-R_1 t} + b\, e^{-R_2 t} + c\, e^{-R_3 t} + \ \ldots\ldots\ldots\ldots\ldots\ldots \qquad (1-30)$$

Then $a, b, c, \ldots\ldots$ can be regarded as the probability that a subgroup of droplets will freeze at the rate R_i:

$$\frac{N_L}{N_{tot}} = P(R_1)e^{-R_1 t} + P(R_2)e^{-R_2 t} + P(R_3)e^{-R_3 t} + \ \ldots\ldots\ldots\ldots\ldots\ldots \qquad (1-31)$$

Therefore, the ultimate unfrozen fraction is given by the summation or integration of all subexponential decays with respect to R:

$$\frac{N_L}{N_{tot}} = \sum_{i=1}^{n} P(R_i)\, e^{-R_i t} = \int_{R_1}^{R_n} P(R_i)\, e^{-R_i t}\, dR \qquad (1-32)$$

where $P(R_i)$ can be obtained from the probability density function (PDF) of the fitted distribution, for example log-normal distribution PDF is:

$$P(R_i) = \frac{1}{R_i\sqrt{2\pi\sigma^2}}\, exp\left(-\frac{(\ln(R_i)-\mu)^2}{2\sigma^2}\right) \qquad (1-33)$$

Here μ and σ are the shape parameters of the log-normal distribution. If each droplet of a subgroup contains INPs with nucleation rates that are for example log-normally distributed around their mean as shown in figure (1-7) a, c, then each subgroup of droplets will freeze at a mean rate R_i. The heterogeneous droplets will thus freeze initially at the mean R_{mean} of these R_i. Also, as t increases the mean R_i of the remaining unfrozen droplets changes as given by equation 33. The mean freezing rate and standard deviation of lognormally distributed R_i can be determined as follows:

$$R_{mean} = exp\left(\mu + \frac{\sigma^2}{2}\right) \qquad (1-34)$$

$$\sigma_{mean} = \sqrt{exp(\sigma^2 - 1)\, exp(2\mu + \sigma^2)} \qquad (1-35)$$

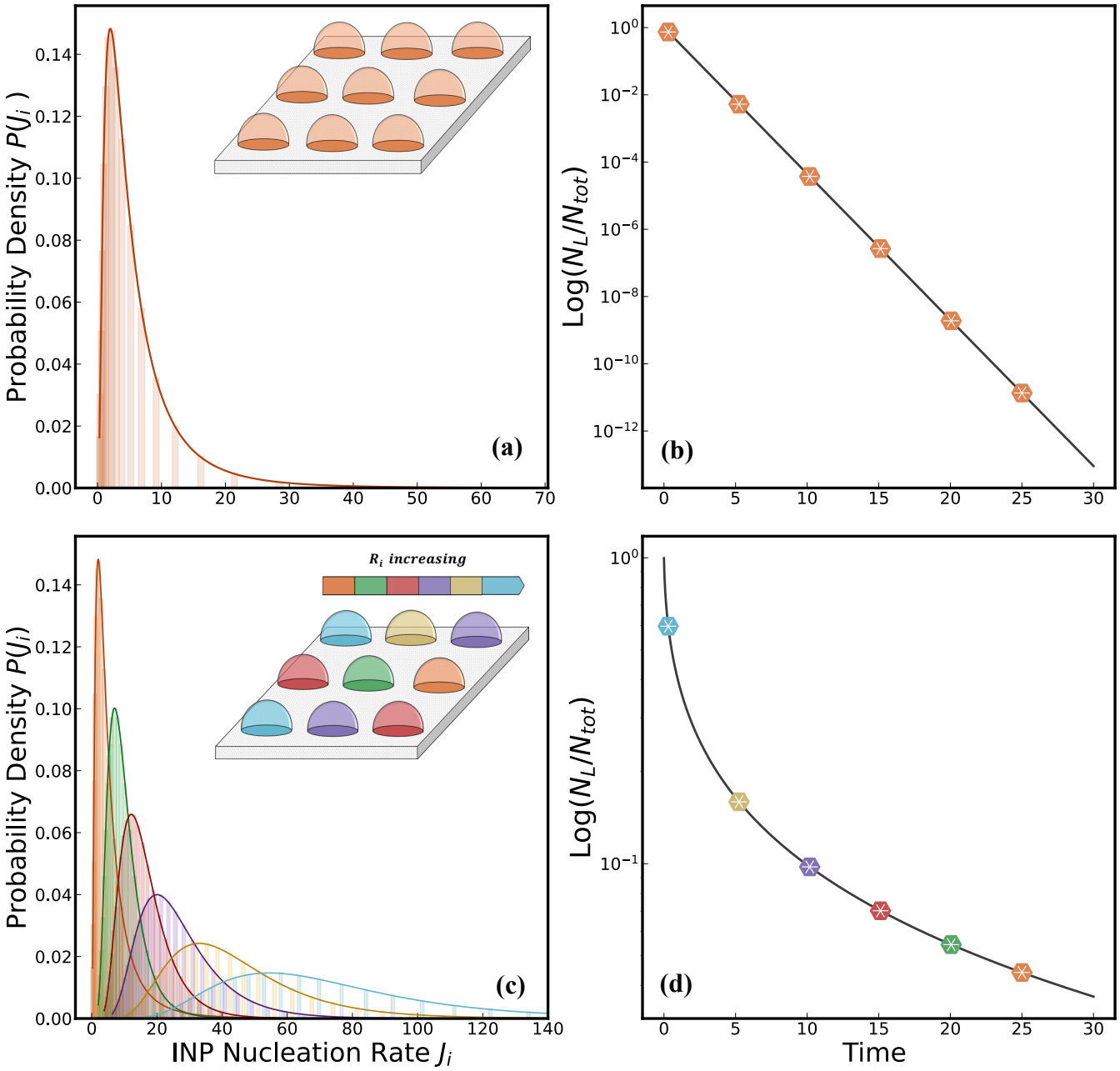

Figure 1-7: Schematic of stochastic (time-dependent) model. (a) A homogeneous droplet array containing INPs with a fixed distribution of J_i values given by the log-normal probability density function (PDF) shown. (b) The plot of log (N_L/N_{tot}) of these homogeneous droplets is linear as a function of time, with the slope corresponding to the droplets' freezing rate. (c) A heterogeneous droplet array (indicated by the different colours) containing INPs with different distributions of J_i values indicated by the different PDF. (d) The plot of log (N_L/N_{tot}) of these heterogeneous droplets is no longer linear over time. Droplets with more effective INPs freeze at a higher rate and as they do so, the mean freezing rate of the remaining droplets falls, leading to a decrease in the gradient of the curve, the colours indicate the sub-group that dominates the freezing at each time.

Furthermore, the number of active INPs in the arrays of droplets can be estimated. Assume $R_{mean} = n\,J$, where n is the number of active INPs of nucleation rate J, and $\sigma_{mean} = J\,\sigma_n$, where $\sigma_n = \sqrt{n}$ is the standard deviation of the number of active INPs. Using the statistical coefficient of variation ratio between a distribution's standard deviation and mean, n can be derived as follows:

$$\frac{\sigma_{mean}}{R_{mean}} = \frac{J\,\sigma_n}{n\,J} = \frac{1}{\sqrt{n}} \qquad (1-36)$$

Hence:

$$n = \left(\frac{R_{mean}}{\sigma_{mean}}\right)^2 \qquad (1-37)$$

According to Andersson et al., the log-normal distribution is an appropriate model for describing the vast majority of first-order kinetic processes in environmental systems than normal distribution [116]. Marcolli et al., for instance, modelled the variation in the surface wettability of mineral dust particles in terms of the contact angle using a log-normal distribution [117]. But the model is constrained by the discrepancies with experimental data.

The normal and log-normal distributions are both appropriate, however for identical INPs but varying in n, the normal distribution most likely describes the system, whereas the log-normal distribution is probably more suitable for describing INPs in environmental systems. The normal distribution probability function (PDF) used to determine the droplets' mean freezing rate and standard deviation is:

$$P(R_i) = \frac{1}{\sigma\sqrt{2\pi}} \exp\left(-\frac{(R_i-\mu)^2}{2\sigma^2}\right) \qquad (1-38)$$

here μ, σ are the actual mean and standard deviation of the distribution.

1.5. Motivations

In this work we investigate heterogenous ice nucleation by biomolecules i.e. Apoferritin and DNA origami tiles. Chapter 2 analyses the ice nucleation efficiency of Apoferritin subcomponents, oligomers, dimers, and monomers using temperature ramp measurements for microlitre and nanolitre droplet volumes. Additionally, nucleation coefficients are derived and discussed. In Chapter 3, we demonstrate that the freezing rate of Apoferritin oligomers, dimers, and monomers can be determined directly with minimal uncertainties by using isothermal measurements. We examine the influence of the protein amount in droplets on the freezing rate by varying the concentration and volume of the droplets. We extract the parameters of classical nucleation theory, including the activation energy-contributing constant, shape factor, and nucleation rate coefficient, for each subcomponent of Apoferritin. In Chapter 4, the impact of the internal temperature gradient on the freezing rate of different droplet volumes is investigated using COMSOL Multiphysics simulations. Using isothermal measurements, observations of droplets with different volumes are obtained for comparison with simulation results. The simulations show how the internal temperature history of a droplet influences the time needed for freezing and becomes significant as the droplet's volume and contact angle increase. In Chapter 5, we study the ice nucleation by DNA origami tiles via temperature ramp and isothermal measurements. We demonstrate that the isothermal approach is an effective method for deriving the parameters of the classical nucleation theory for DNA origami. For future research, it may be concluded that DNA origami can serve as a INP model for studying heterogeneous ice nucleation using custom-designed structures.

2. CONSTANT COOLING RATE MEASUREMENTS

2.1. Introduction

There are several aerosol particles that serve as ice nucleating agents to initiate the formation of ice within the climate system. For heterogeneous ice nucleation, these aerosols are primarily categorised as inorganic and organic ice nucleation particles (INPs). Mineral dusts like feldspar are one of the well-known, effective INPs example that have been thoroughly researched in a number of literature sources [17,18,118–120]. Organic INPs have also been studied; one of the best-known active INPs is the bacterium Pseudomonas syringae, which induces nucleation at temperatures close to the melting point of ice, 0 ^{o}C [71,121].

However, one of the problems encountered in the immersion freezing mode is the purity of the INP samples used for constant cooling rate measurements, which contributes to a certain extent to the propagation of uncertainties in subsequent analyses. This is due to the tendency of biomolecules, such as proteins and viruses, to aggregate and dimerize from their monomeric forms. There are a variety of reliable purification techniques to separate their components and assess their purity conditions. Size exclusion chromatography (SEC) and Blue Native PAGE gel electrophoresis are well-known techniques for determining the purity of sample fractions. Consequently, biological particles can be used as models to investigate heterogenous ice nucleation and their contribution to the atmospheric system. Protein aggregates and viruses have been reported as ice nucleation agents [77,97]. M. Cascajo-Castresana et al. investigated non-purified Ferritin and Apoferritin ice nucleation and concluded that the oligomers of both proteins are particularly effective INPs that commence freezing at warmer temperatures. Due to the fact that aggregates often comprise multiple protein components of various shapes and sizes, the regarded efficiency cannot be established with precision, and additional uncertainty will be found in the observations. In this Chapter, we will look at Apoferritin's ice nucleation activity. Apoferritin will be separated into three peaks based on their sizes: oligomers, dimers, and monomers. Their ice nucleation efficiency will be compared by evaluating their frozen fraction and nucleation rate coefficients with respect to the freezing temperature of microlitre and nanolitre droplets using the standard experimental method, constant cooling rate.

2.2. Materials and Methods

2.2.1. Ferritin and Apoferritin

Ferritin (Fr) is a protein that is composed of 24 subunits and forms a spherical shell with an inner cavity. This cavity is about 7-8 nm in diameter and can hold up to 4500 iron atoms (Fe^{3+}) in the form of an amorphous oxide. The outside diameter of the Ferritin shell is approximately 12 nm. When the iron is removed from Ferritin, it is referred to as Apoferritin (Apo). Apoferritin is the iron-free form of Ferritin protein, see Figure (2-1) [97,122–127].

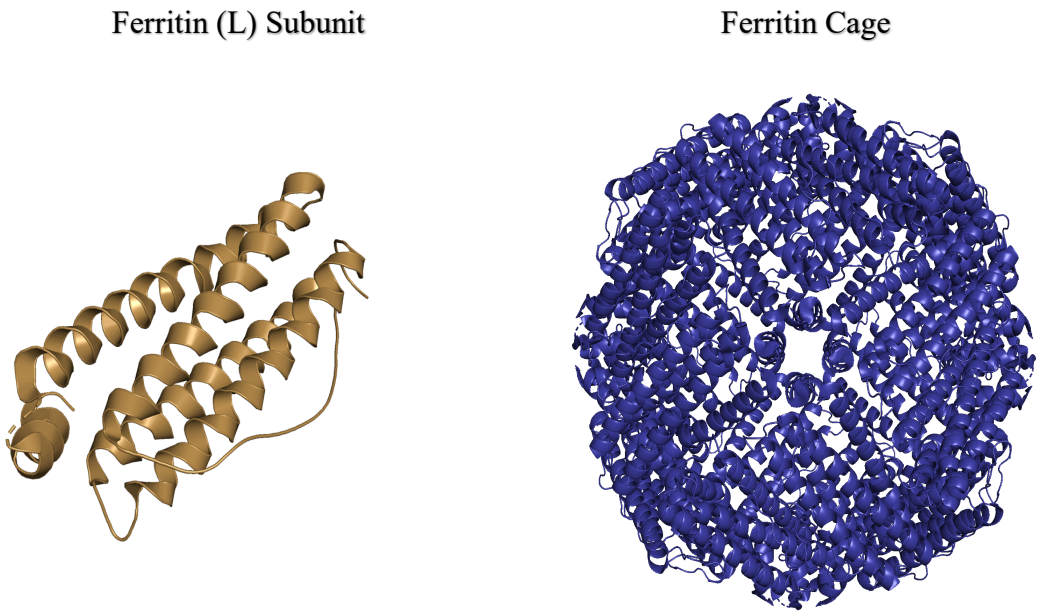

Figure 2-1: The horse spleen Ferritin/Apoferritin (L) subunit and the structure of the spherical cage. There are four helices in the subunit. Ferritin produced from horse spleen is mostly composed of approximately 90 wt % light subunits. The whole ferritin cage is constructed from 24 identical subunits. Ferritin has an iron core, while Apoferritin has a free-ion core (PDB ID: 4V1W, [123]**).**

The Apoferritin cage in mammals e.g. horses is made up of L (light) and H (heavy) subunits, with a stoichiometry unique to the tissue [97,122]. In Fr and Apo, there are channels where the subunits meet, allowing for the passage of ions and molecules of interest. Ferritin's capacity to release iron in a regulated manner is dependent on these channels [97].

Apoferritin has sparked considerable interest, particularly from the academic community, for numerous applications. For instance, it can be used as a fluorescent marker, contrast agent for MRI, for drug delivery, and it also serves as a template for producing nanoparticles. This is all due to the fact that Apo is a stable and spherical hollow sphere with channels for access [122,124].

Studies using gel filtration analysis (GF) and gel electrophoresis (GE) have indicated that commercial Apoferritin solutions are heterogeneous and not homogeneous. They contain a mixture of oligomers, dimers, and trimers in addition to monomers. The monomer is a single iron-free cage that is composed of 24 subunits and has a molecular weight of around 450-500 kDa. The dimer is generated by twice as many subunits as a monomer, totalling 48 subunits, to create a dumbbell-like structure of two spherical cages. The trimer can take on one of two distinct shapes: either a linear trimer consisting of three spherical cages that are adjacent to one another, or a triangular trimer in which a void will be formed at the interception point of the three cages, i.e. the centre. The remainder will consist of higher oligomers or agglomerates with a greater molecular mass than trimers [125–130] (see Figure 2-2).

2.2.2. Sample Preparation

0.2 μm filtered horse spleen Apoferritin was purchased from Sigma-Aldrich. Apoferritin solution with an initial concentration of 37 mg/ml was diluted to about 20 mg/ml in Tris buffer (0.5 mM Tris and 150 mM NaCl, pH 8) (Sigma-Aldrich) before being injected into the size exclusion chromatography system (SEC). Tris buffer, also known as Tris(hydroxymethyl)-aminomethane, is a basic buffer used in biochemistry and molecular biology to resist pH changes. The pH of a Tris buffer can be adjusted by blending Tris HCl and Tris Base.

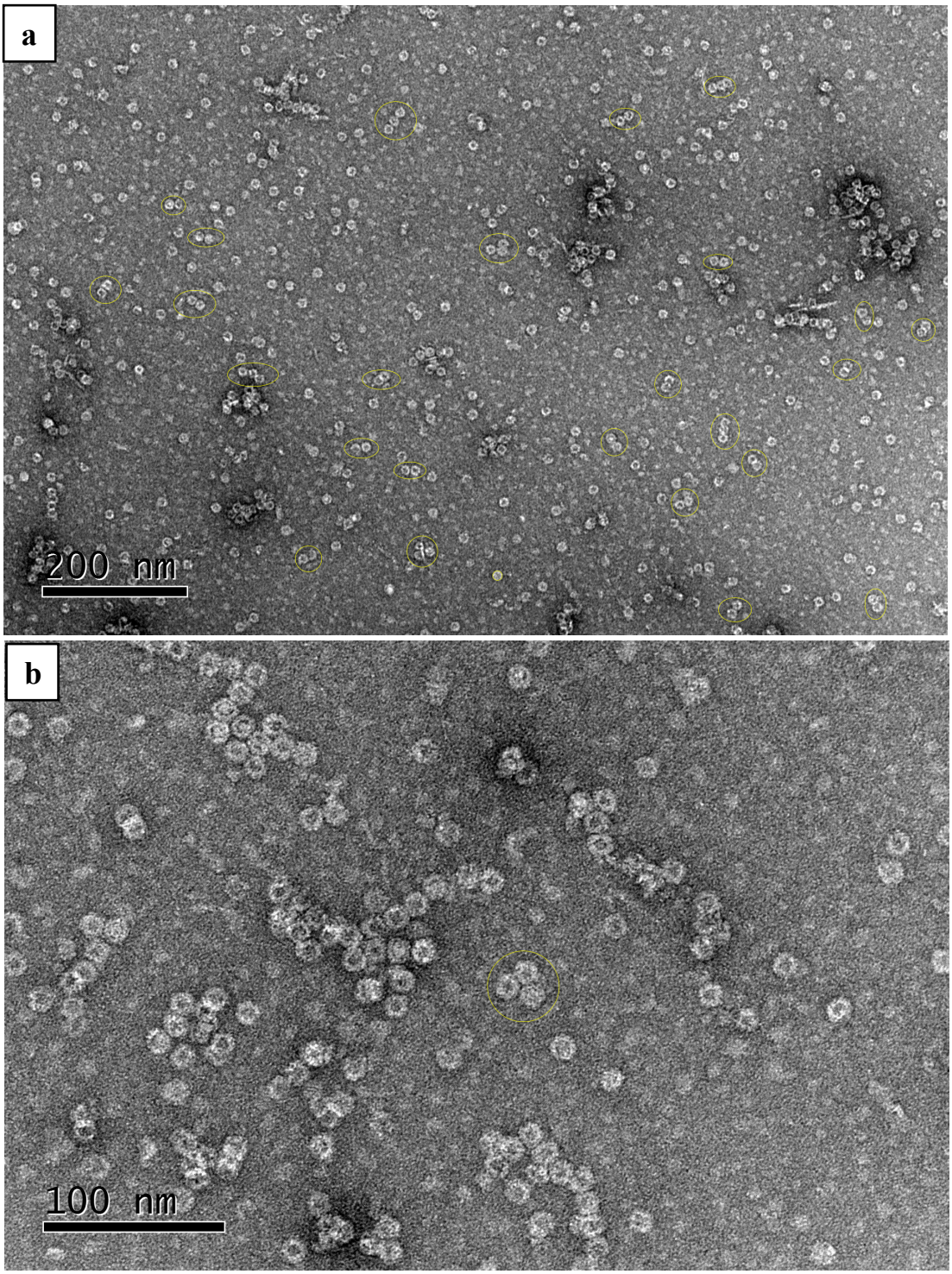

Figure 2-2: Horse spleen Apoferritin imaged by Transmission Electron Microscope (TEM). The images demonstrate the heterogeneity of commercial Apoferritin before it is purified. The yellow circles in (a) represent monomers (one sphere), dimers (two spheres), and both linear and triangular (b) trimers (three spheres). The large irregular forms may represent oligomers with a greater molecular weight.

2.2.3. Apoferritin Purification by Size Exclusion Chromatography (SEC)

Proteins are very soluble in water, and in addition to their nanoscale sizes compared to inorganic INPs, there are a number of dependable approaches for determining their purity status. Besides, it is feasible to separate protein subforms depending on their size using size exclusion chromatography (SEC). Size Exclusion Chromatography (SEC) is an example of an HPLC method used to separate proteins. In analytical chemistry or biology, high-performance liquid chromatography (HPLC) is a method for separating, identifying and quantifying components in a combination. It is based on the principle that different compounds in a mixture will elute (i.e. be separated and detected) at different times when passed through a stationary phase (e.g. a column packed with resin) under high pressure. A detector, such as a UV-Vis spectrophotometer, is used to detect the presence of the separated compounds as they elute from the column [126,129,130].

Separation was achieved by passing 2ml of horse spleen Apoferritin through a porous medium packed in a gel filtration column (Sephacryl S300, GE Healthcare Life Science). The sub-forms of Apoferritin were separated according to their size or molecular weight. The column was initially equilibrated overnight with 120 ml buffer, and then the diluted Apoferritin sample was injected into the column which was mounted in a ÄKTA HPLC system (GE Healthcare Life Science). The eluted fractions of protein were detected by the system's UV detector as the Apoferritin chromatogram occurred at 280 nm wavelength. In SEC, the molecules with the highest molecular weight come out first, while the molecules with the lowest molecular weight come out last. This means that Apoferritin oligomers come out first (peak 1), followed by dimers (peak 2), and then by monomers (peak 3), which have the lowest molecular weight. The chromatogram revealed that monomers were the predominant sub-form of Apoferritin, followed by dimers, while trimers and higher oligomers were the least abundant, as seen in figure (2-3).

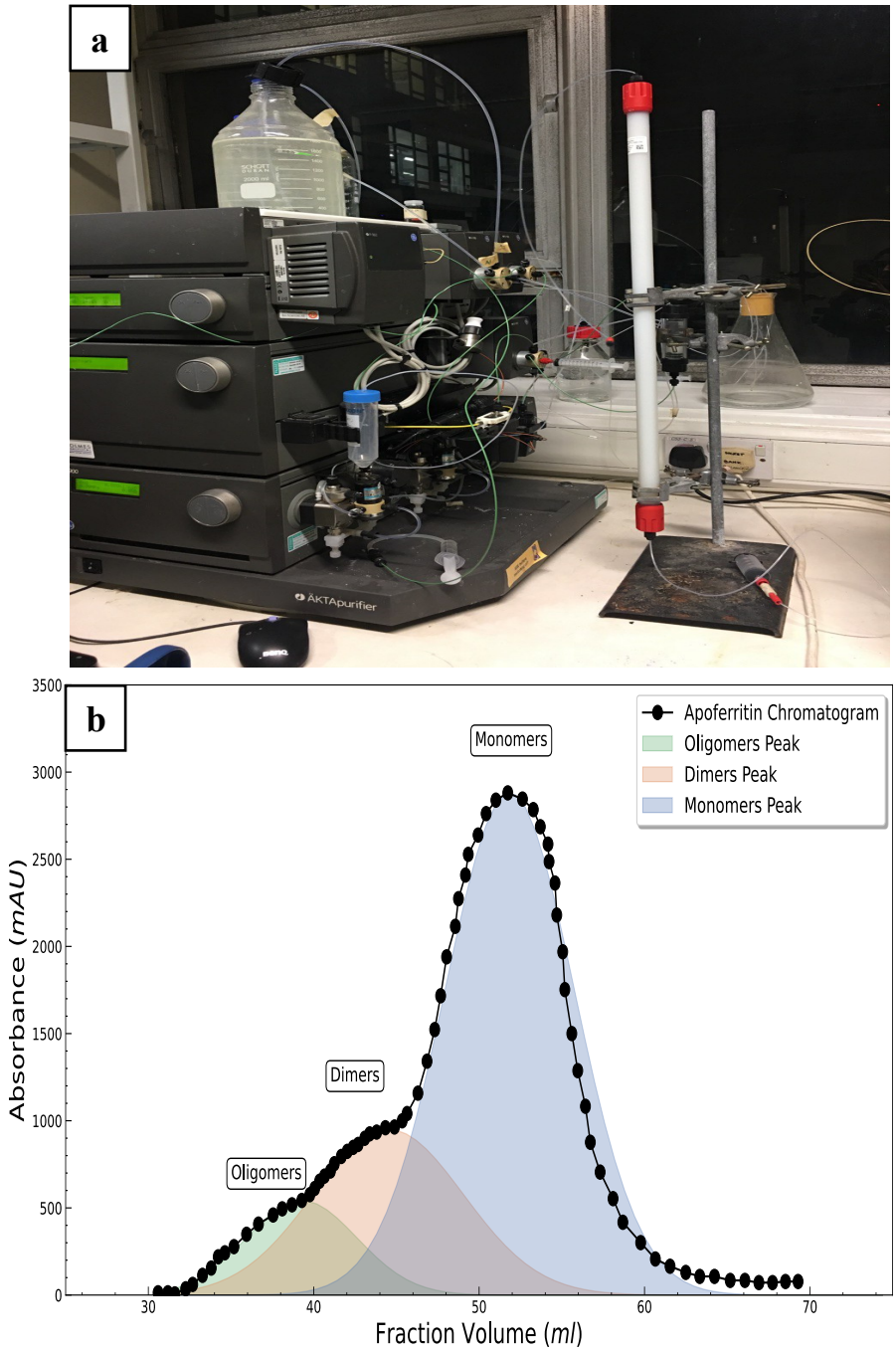

Figure 2-3: (a) System for size exclusion chromatography (ÄKTApurifier). Sephacryl S-300 HR (Hi Prep 16/60) column is connected to the system (white with red ends). The column's upper tubing is connected to the system pump via a valve, while the column's lower tubing is connected to the UV detector. The column was equilibrated with 120 ml of buffer (0.5 mM Tris and 150 mM NaCl) at a flow rate of 0.5 ml/min and a maximum pressure of 0.15 MPa. 5 ml of Apoferritin sample (20 mg/ml) was manually injected into the column by the valve using a syringe. (b) SEC chromatogram of Apoferritin at 280 nm UV absorption (black). The three primary peaks, from left to right, are respectively oligomers, dimers, and monomers. The molecules with the highest MW are eluted first, followed by the molecules with the lowest MW. In order to demonstrate the peaks, each of which was fitted to a Gaussian distribution, it is obviously shown that monomers are the predominant form of Apoferritin, followed by dimers. The volume of each eluted fraction was 0.5 ml.

2.2.4. Blue Native Polyacrylamide Gel Electrophoresis (BN-PAGE)

Blue Native PAGE gel electrophoresis was used to determine the molecular weight of proteins in their native form and assess the purity and ratio of sub-forms in the fractions [131–134]. In this procedure, the proteins are subjected to a current. Since proteins typically carry a negative charge, they migrate through the gel matrix in the direction of the positive electrode. Regarding the molecular weight (MW) of proteins, those with a higher MW migrate less and those with a lower MW migrate farther due to their size in comparison to the pores size of the gel matrix. Molecular weight is determined by comparing the unknown protein to a protein ladder with a known molecular weight. Each gel cassette well was loaded with 10 µl of protein (Invitrogen NativePAGE 3 - 12 %, Bis-Tris, 1.0 mm gel thickness). The gel was run for two hours at 150 V using outer buffer (Invitrogen NativePAGE Running Buffer - 20X) and inner buffer (Invitrogen NativePAGE Cathode Buffer Additive - 20X). BN-PAGE was used to characterise the purity and heterogeneity of monomers and dimers from SEC. Figure (2-4) shows an example of a gel result.

2.2.5. Bradford Assay

The concentration of SEC fractions was determined using the Bradford assay method [135–138]. In a standard 96-well plate, 250 µl of Bradford reagents (Sigma-Aldrich) was added to 5µl of protein sample. With a microplate reader (Biocompare), the absorbance of the mixture (a blue protein-dye complex) was measured at 595 nm. The unknown sample concentration (mg/ml) was estimated using a linear equation based on the known concentration and absorbance of standard proteins.

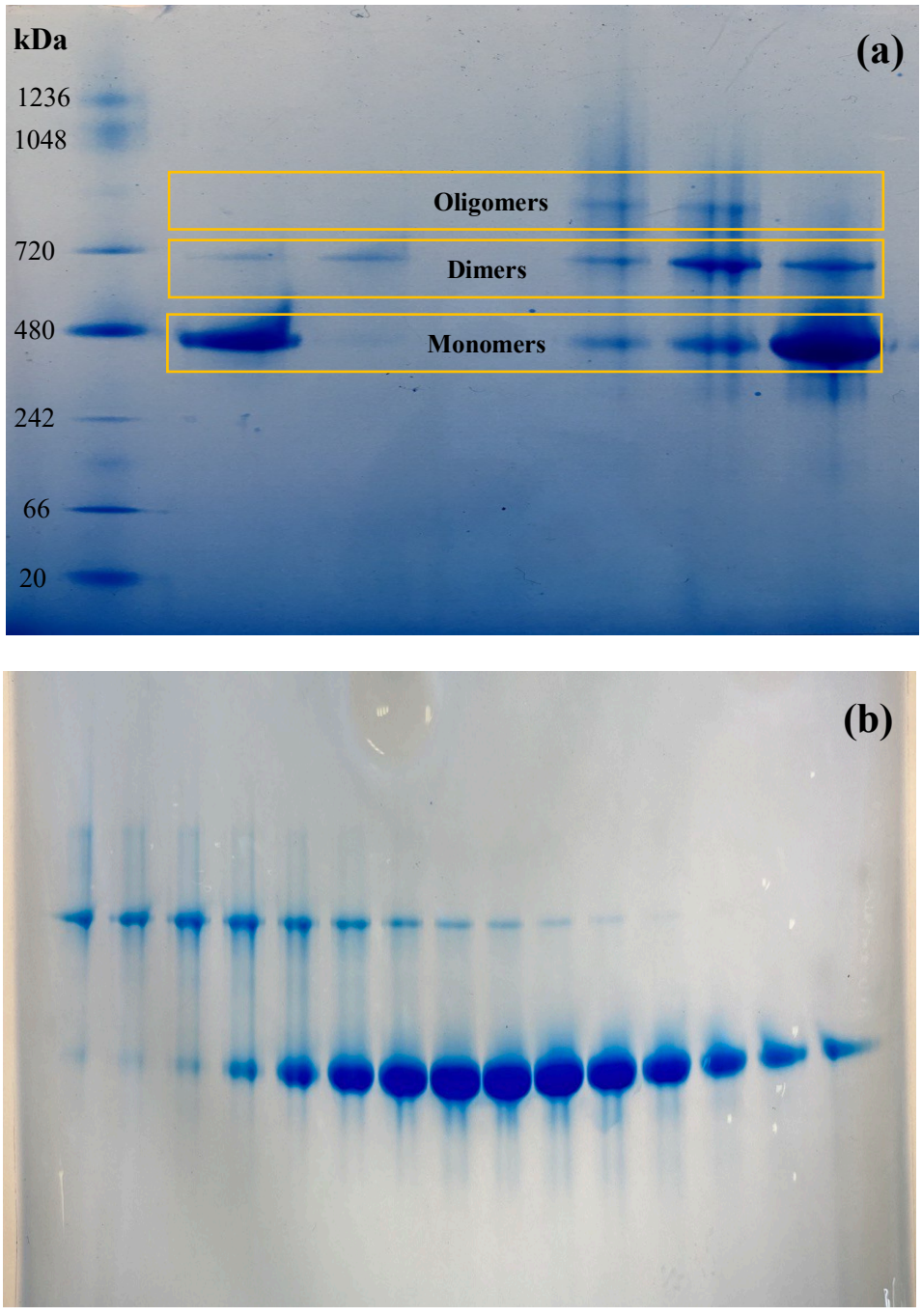

Figure 2-4: (a) The protein ladder (NativeMark Unstained Protein Ladder) with known molecular weights is shown in the first lane from the left. The second through sixth lanes display various SEC fractions of Apoferritin, with the bottom bands corresponding to monomers (MW about 450 kDa) and the middle bands corresponding to dimers (MW 720 kDa). The upper bands represent oligomers. (b) Examples of SEC fractions for Apoferritin clearly indicate monomers, dimers, and oligomers. In accordance with the SEC chromatogram, monomers have the highest peak and is the predominant species in Horse spleen Apoferritin.

2.2.6. Droplet Assays

First, silicon substrates were coated with Dimethyloctadecyl [3-(trimethoxysilyl) propyl]ammonium chloride (DMOAP) at a concentration of 0.1 to 1 % (v/v) and treated in an oven at 120 °C for an hour. For each experiment, a total of 10 droplets of 1µl size were pipetted onto a treated slide using an electronic microlitre pipette, with sufficient spacing between the droplets. The second droplet assay used nanolitre droplets and the droplets were sprayed (Mini Spray Atomizer – 3ml) on treated slides and coated with silicone oil. A temperature-controlled stage (Linkam THMS600) was then used to cool the droplets array below their equilibrium melting point to the desired temperature. In this setup, samples were placed on a 22mm-diameter silver stage inside a well-sealed chamber. The stage is cooled with liquid nitrogen by means of an LN pump and controller (LNP95) controlled by a LabView programme. For constant cooling rate measurements, the rate of cooling from the initial temperature to the desired temperature was set at 20 °C /min. The temperature was then steadily decreased by 1 °C /min while freezing images were captured. Droplets freezing events were observed using an OLYMPUS SZX10 Stereomicroscope with a magnification range of 0.63x to 6.3x and an attached digital camera (Moticam 5MP) for picture capture. The number of unfrozen droplets was calculated using ImageJ software and the Python programme YOLOv5 (Object detection algorithm).

2.2.7. Data Analysis of Immersion Freezing

The frozen fraction for constant cooling rate measurements was obtained by applying the following formula:

$$f(T) = \frac{N_f(T)}{N_L} \qquad (2-1)$$

Where N_L is the total number of liquid droplets at the start, $N_f(T)$ is the cumulative number of frozen droplets at temperature T.

2.3. Results and Discussion

2.3.1. Constant Cooling Rate Measurements of 1µl Droplets

The constant cooling rate is the most common approach for studying homogeneous and heterogeneous ice nucleation. In this method, the temperature of the droplets is gradually decreased toward low temperatures at a fixed cooling rate. The cumulative frozen fraction of the droplets is then determined as a function of temperature. This technique is effective when an overview of a sample is required, regardless of the sample's purity status, since the frozen fraction of the droplets can be used to establish the temperature range in which ice nucleating agents are most active. In the case that the freezing temperature range is relatively narrow, this suggests that the freezing of the droplets could be caused by a single nucleating agent (INP) or single active site. On the other hand, if the freezing temperature range is relatively broad, this suggests the presence of multiple nucleating agents or multiple active sites. When the frozen fraction of droplets appears at higher temperature ranges, this can be referred to as an efficient INP or INP active site. For freezing at lower temperatures, which can be referred to as a less efficient INP, the frozen fraction data may approach what would be observed for homogenous ice nucleation. Consequently, the state of the sample to be frozen in terms of purity could contribute greatly to either maximising or limiting the uncertainties in the frozen fraction. For instance, when the sample includes many species, each with a distinct efficiency, the frozen fraction will represent a greater degree of ambiguity; conversely, when the sample is highly pure, the measured frozen fraction will correspond to the single species that the sample contained. The cumulative frozen fraction of 1 µl droplets containing 1 mg/ml of Apoferritin oligomers, dimers, monomers, and buffer from constant cooling rate experiments is shown in figure (2-5).

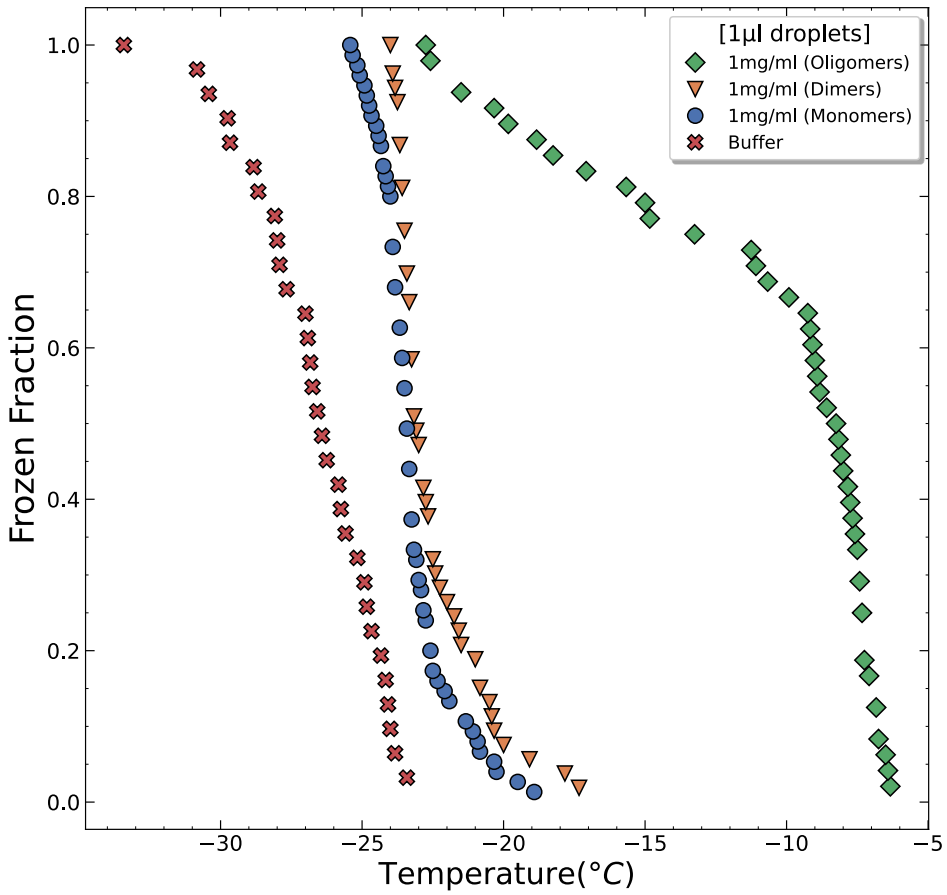

Figure 2-5: The cumulative frozen fraction for Apoferritin subforms: oligomers, dimers and monomers as well as buffer. The droplet concentration for all subforms was 1 mg/ml. Oligomers consisting of Apoferritin trimers of two types (linear and triangular) as well as higher forms of aggregates froze at higher temperatures and over a broader temperature range, indicating that the freezing of the droplets is caused by multiple INPs of different sizes or multiple active sites per subform. Dimers and monomer frozen fractions showed considerably narrower freezing ranges than oligomers, and this was presumably because dimers and monomers had less diversity among them. However, since they are smaller than oligomers, their frozen fractions shift toward lower temperatures, with the shift for dimers smaller than for monomers. Oligomers are more efficient ice nucleating agents than dimers and monomers. The latter freeze at a higher temperature than their buffer.

Droplets containing oligomers, which correspond to SEC peak 1, froze between –5 and –23 °C, followed by droplets containing dimers, SEC peak 2, which froze between –17 and –24 °C, and droplets having monomers, SEC peak 3, which froze between –19 and –25.5 °C. In general, the three froze at higher temperatures than the buffer, which froze at temperatures between –22 and –33.5 °C. Since the oligomer SEC peak includes linear and triangular Apoferritin trimers as well as higher Apoferritin aggregates, this explains why the oligomers freezes over a wider temperature range. As there are multiple Apoferritin subforms of different sizes, there is a greater likelihood that different active sites exist. This means that the droplets freeze at different

temperatures, but in general, they freeze at a higher range of temperatures than dimers and monomers. SEC fractions corresponding to peak 2 may initially contain only dimers; however, due to the fast rate at which dimers can dissociate into monomers, samples may contain both dimers and monomers. Typically, the ratio of dimers to monomers in these samples is greater than one. In contrast, monomer samples are highly pure and have a lower probability of dimerizing than dimers have of dissociating [125,128]. Unlike oligomers, dimers and monomers froze over a much narrower range of freezing temperatures and at lower temperatures. Although the temperature freezing ranges of monomers and dimers overlap to some degree, the dimers froze at slightly higher temperatures compared to monomers, implying that dimers are better INP than monomers due to their larger size. In addition, dimers possess a central junction between the two spherical cages, which might form an active site, while monomers consist of a single nano spherical cage with no junctions. In spite of this, Apoferritin monomers are active as ice nucleating agents due to the fact that, in comparison to the pure buffer, they cause the frozen fraction to shift toward higher temperatures. Buffer freezing over a wider temperature range might be due to background impurities.

2.3.2. Constant Cooling Rate Data for Nanolitre Droplets

The purity of the sample to be frozen is one of the most prevalent obstacles in ice nucleation experiments. This challenge is notably evident when freezing droplets of inorganic nucleating agents like Feldspar, which are dusty in nature and have a limited solubility in water. Due to the dusty nature of Feldspars, as INP examples, they are less uniform in terms of size and shape, which are two crucial characteristics that impact the efficiency of INPs. Unfortunately, there are not many very effective and accurate size-based methods for segregating Feldspar particles. Hence, using very small droplet volumes, such as nanolitre droplets, is the experimental method for reducing the amount of uncertainty associated with measurements of the frozen fraction. As a result, instead of freezing occurring due to a few efficient and rare species in the droplets, as could be the case for larger droplets, more common but less effective species can play a role as the probability of a single droplet containing a rare species will decrease. Although purification of proteins by SEC and characterization of their purity state in the sample by gel electrophoresis enhanced the specificity of the data relative to inorganic INPs by separating all different species within sample fractions, it is still of interest to test nanolitre droplets containing Apoferritin oligomers, dimers, and monomers.

Nanolitre droplets were sprayed on DMOAP-treated silicon surfaces and covered with silicone oil to inhibit the evaporation process. One of the challenges that were faced while spraying protein solutions was the difficulty in obtaining consistent droplet sizes; see figure (2-6).

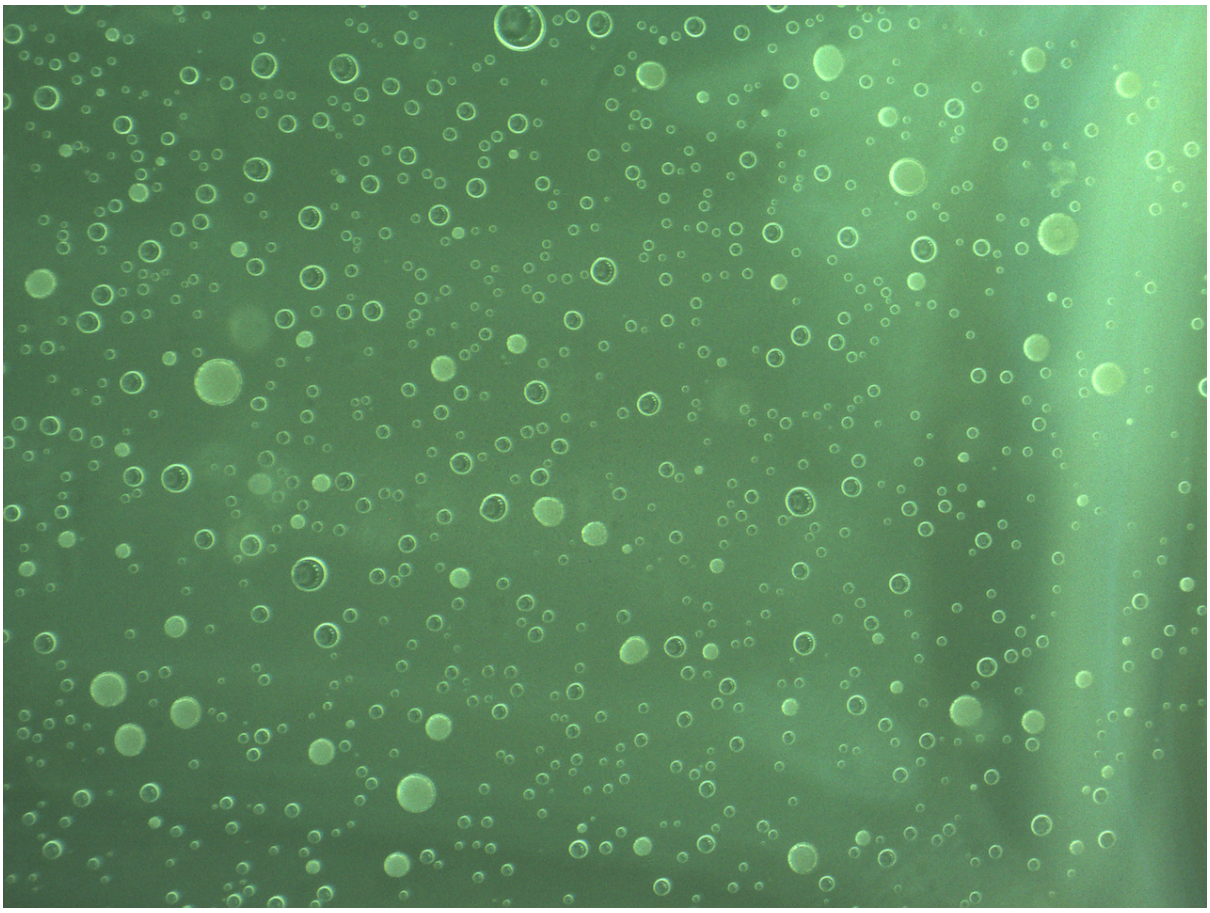

Figure 2-6: Sprayed droplets on a silicon substrate treated with DMOAP to increase its hydrophobicity. The droplets are coated with silicone oil to reduce their evaporation because of their small volume. The majority of droplets have a nanolitre volume, but they are not all the same size; thus, the data acquired for frozen droplets was divided into three volume groups: [0.1 – 0.9] nl, [1 – 9] nl, and [10 – 90] nl. The concentration of sprayed Apoferritin droplets was decreased to reduce the influence of the high surface tension of the solution at high concentration, which distorts the droplet shape when sprayed on substrates.

Another obstacle was the concentration of the protein solutions; when the concentration is high, for example 1 mg/ml, the sprayed droplets will merge and become non-spherical; this is due to the influence of protein viscosity, as the higher the concentration of protein solution, the greater the surface tension. The observed frozen fraction for nanolitre droplets was analysed for three different size groups, including [0.1 – 0.9] nl, [1 – 9] nl, and [10 – 90] nl. Moreover, in order to minimise the effect of viscosity of the protein solution on the shape of the sprayed droplets, the concentration of the protein solutions was reduced by a factor of 10 compared to the concentration used in the 1µl droplets in the previous section; thus, the final concentration of the nanolitre droplets used was between 0.1 and 0.2 mg/ml. Figure (2-7) shows frozen fraction data for droplet sizes in the range [1 – 9] nl at a concentration of 0.1 mg/ml for oligomers, dimers, and trimers; this range of droplet sizes represented the most abundant volume across all the three size groups.

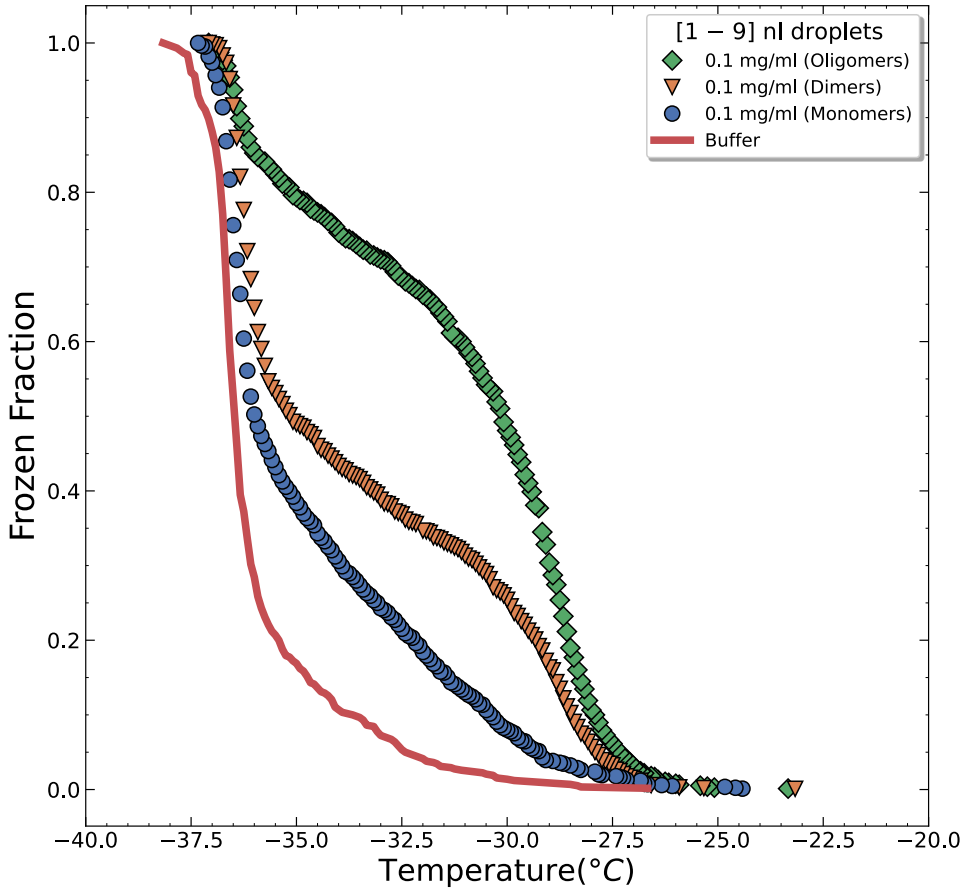

Figure 2-7: The frozen fraction of the most abundant nanolitre droplets, [1 – 9] nl, containing 0.1 mg/ml of Apoferritin oligomers, dimers, and monomers, as well as a buffer. It can be seen that oligomers freeze at the highest temperature, followed by dimers and then monomers, while buffer freezes at the lowest temperatures. Consequently, oligomers are the most effective subform of Apoferritin, followed by dimers and monomers, which are also good examples of INPs due to the fact that they freeze at higher temperatures than the buffer.

The frozen fraction is in general agreement with the 1µl droplet results, as oligomers freeze at the highest temperatures, followed by dimers, and finally by monomers, and all three freeze over higher temperature ranges than their pure buffer. Compared to the temperature ranges for microlitre droplets, the temperature ranges at which nanolitre droplets freeze have shifted toward very low freezing temperatures. All three Apoferritin subforms began freezing about −23 ºC and ended at −38 ºC, however the shapes of the frozen fraction curves differ. The freezing ranges are broader, notably for dimers and monomers, but the microlitre droplets of high concentration (1mg/ml) exhibited a narrower freezing temperature range. One possible explanation for this could be the low protein concentration of the droplets, which affects the distribution of INPs within droplets; for instance, rare INPs will be distributed in some droplets, but not every droplet will contain a rare INP, as is the case for higher concentration and volume droplets; in other words, the probability of having a rare INP decreases as concentration and volume decrease. This explains why certain protein droplets freeze at temperatures near to the homogenous frozen fraction around −37 to −38 ºC, suggesting that these droplets may have few or no effective proteins, causing them to freeze in the buffer temperature ranges. Furthermore, the size variation of the droplets, even if it is within the nanolitre volumes, may contribute to a wider freezing temperature range, as the smallest droplets usually freeze at low temperatures while the largest droplets freeze at higher temperatures, which may account for the wide frozen fractions of the proteins and their buffer. Similar to the frozen fraction trend of [1 − 9] nl, the other two droplet volume groups with less frequent volumes, [0.1 − 0.9] nl and [10 − 90] nl, also exhibit consistent results with respect to oligomers, dimers, and monomers, as shown in figure (2-8). Overall, at low protein concentrations, oligomers are the most effective ice nucleating agents among the Apoferritin subforms, but a noticeable difference was noted between dimers and monomers, with dimers being clearly more efficient INPs than monomers, which were nevertheless effective INPs compared to pure buffer. Moreover, the resolution of the frozen fraction has improved after the use of the tiny droplets therefore, as dimers and monomers freezing have been clearly separated and this is picked up in the data.

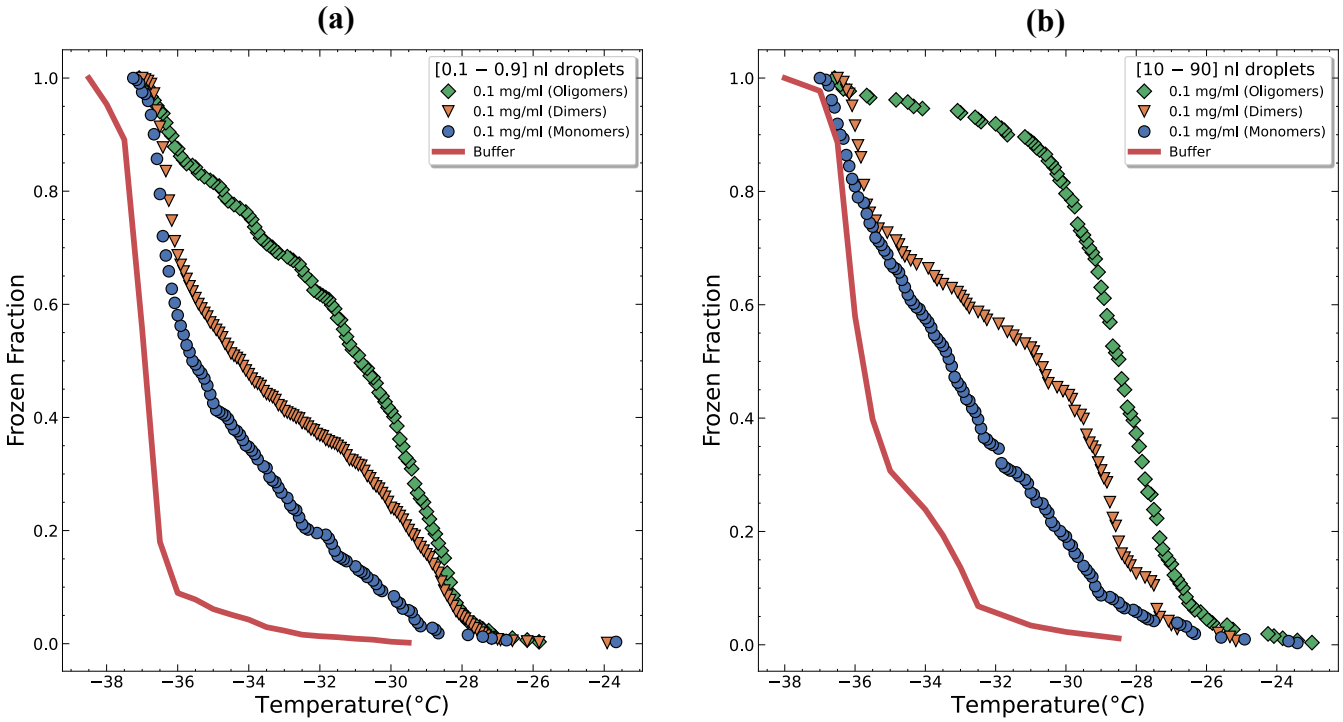

Figure 2-8: Additional examples of frozen fraction data for 0.1 mg/ml Apoferritin for droplets of [0.1 – 0.9] nl (a) and [10 – 90] nl (b). A similar trend to that reported for [1 – 9] nl is also evident for oligomers, dimers, monomers, and buffer.

The concentration of proteins also has an effect on the frozen fraction of the droplets; for example, when the concentration is reduced, the frozen fraction shifts towards lower temperatures, and vice versa. Figure (2-9) illustrates some examples of the concentration effect on two different monomer concentrations and droplet sizes. In order to increase the probability of a droplet freezing, the number of INPs that are contained inside the droplet needs to be increased. This can be attained in one of two ways: either by increasing the volume of the droplets or by increasing the concentration of the INP in a droplet.

When comparing the frozen fraction of droplets with the same protein concentration but of different volumes, such as [0.1 – 0.9] nl and [10 – 90] nl, the larger droplets froze at higher temperatures while the smaller droplets froze at lower temperature ranges, this was observed regardless of which Apoferritin subform was frozen, as shown in figure (2-10).

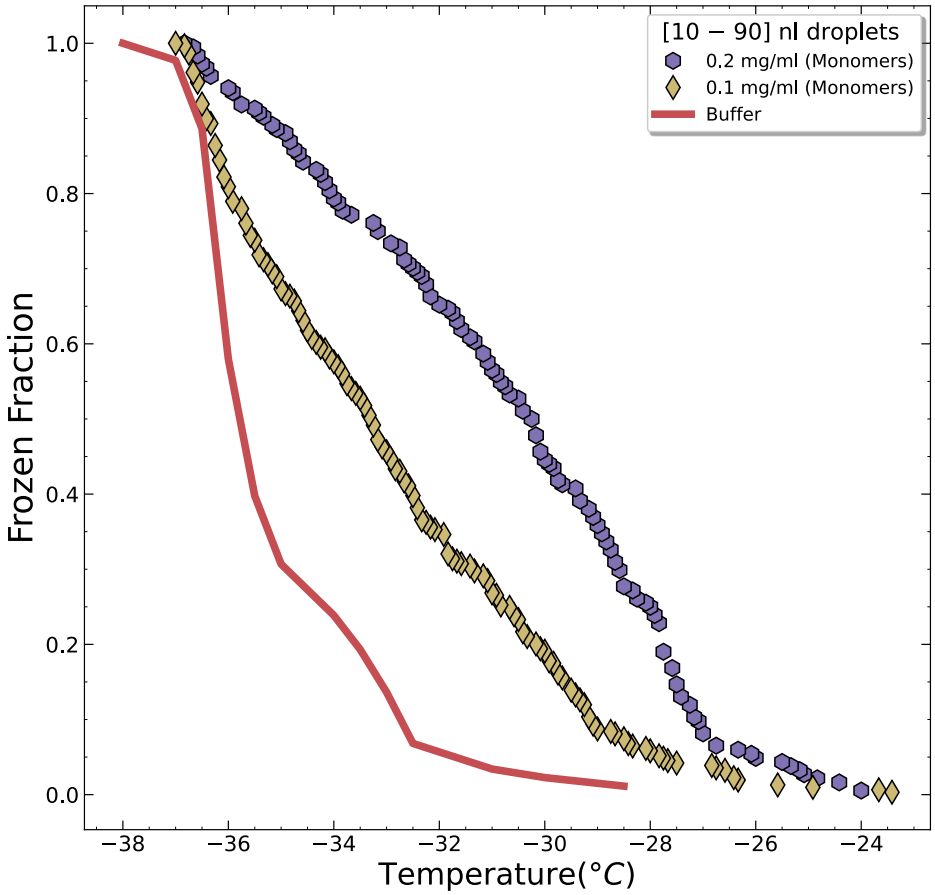

Figure 2-9: The effect of two different concentrations of monomers on the frozen fraction of nanolitre droplets of sizes [10 – 90] nl relative to buffer. When the concentration of monomers is increased, droplets freeze at higher temperatures, and vice versa. The concentration determines the number of INPs per droplet, which in turn determines the probability that the droplet will freeze at a certain temperature, as a higher INP number per droplet corresponds to a higher probability of freezing and a lower INP number in a droplet corresponds to a lower probability of freezing.

This confirms the idea that the freezing temperature ranges over which INPs induce freezing are significantly influenced by the impact of the number of INPs per droplet if the volume is varied. As a result, increasing the size of the droplets that contain proteins will increase the probability that freezing will occur at higher temperatures.

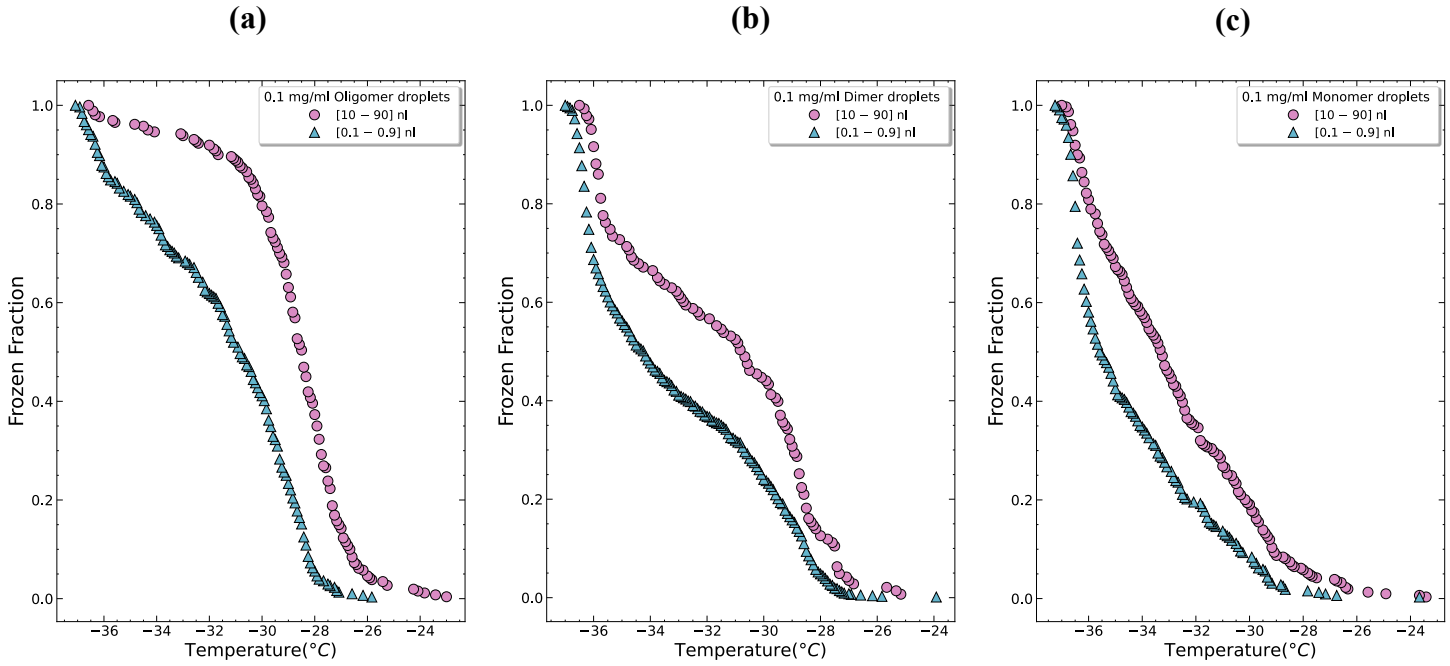

Figure 2-10: Increasing/decreasing the size of droplets with the same concentration is another way to present the relationship between the number of INP per droplet and the probability of freezing. The freezing temperatures of bigger droplets with the same Apoferritin concentration [10 – 90] nl (oligomers (a), dimers (b), and monomers (c)) have moved to higher temperatures compared to [0.1 – 0.9] nl. Larger droplets contain a greater number of proteins than smaller droplets of the same concentration, increasing their likelihood of freezing at higher temperatures.

Buffer data for different volume droplets agree with Apoferritin findings; bigger buffer droplets froze at higher temperatures, while the smallest froze at lower temperatures. Even though they are buffer droplets that did not contain proteins and buffer is considered a homogenous freezing example, larger droplet volumes have a greater likelihood of containing contaminants than smaller droplet volumes, which could explain why larger droplets freeze at higher temperatures than smaller droplets, as shown in Figure (2-11). Due to the nanolitre size range of these droplets, they will not be exposed to a considerable inner temperature gradient, which impacts bigger droplet sizes more; this effect will be addressed in length in Chapter 4.

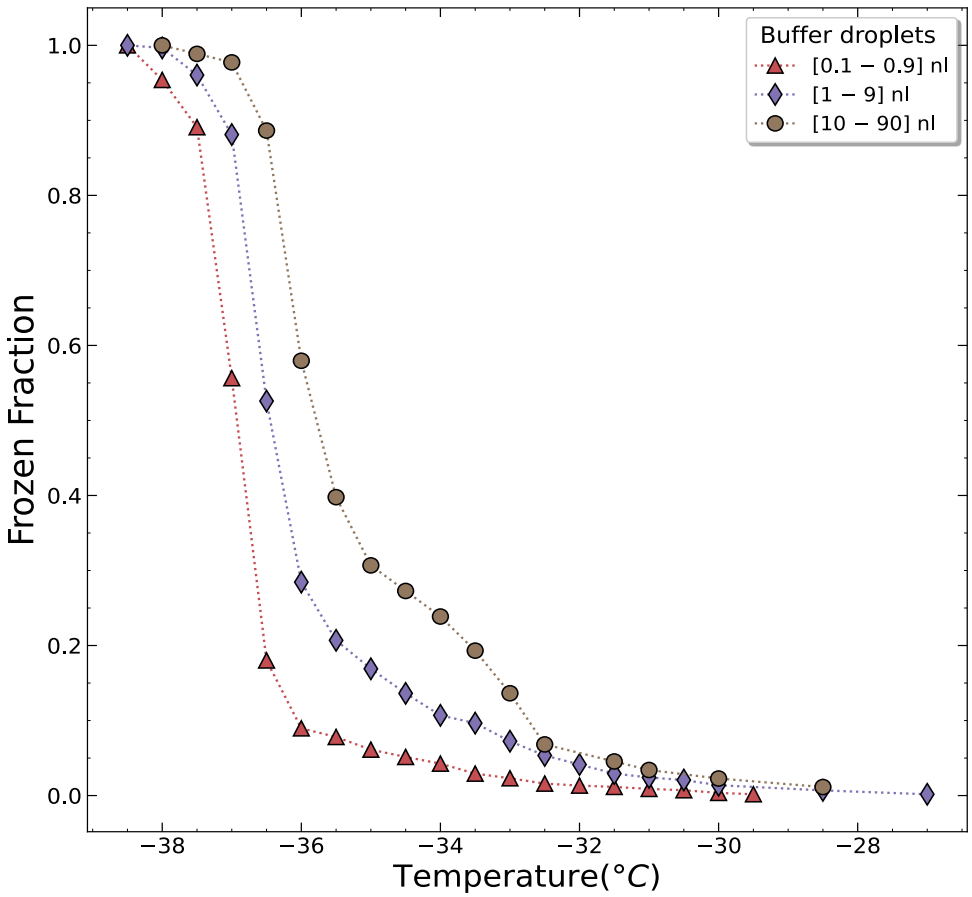

Figure 2-11: The effect of droplet volume on the frozen fraction of the buffer. Larger droplets [10 – 90] nl freeze at higher temperatures, then droplets [1 – 9] nl and the smallest ones [0.1 – 0.9] nl freeze at the lowest temperatures. It demonstrates that even pure buffer (protein-free) droplets may contain impurities, hence raising the freezing likelihood as the droplet volume increases.

2.3.3. Comparing Experimental Findings with Existing Literature

To interpret our findings in the context of existing literature we looked at the study by M. Cascajo-Castresana et al. [97], which is closely related to our work. In their study, they focused on the ice nucleation of proteins, specifically Apoferritin and Ferritin. They referred to the astonishingly high efficiency of Apoferritin and Ferritin due to protein aggregations present in the solution, which can occur through two mechanisms: those normally found in the solution or those resulting from disassembled monomer cages.

They found that Apoferritin freezes within temperature ranges starting from −5 to −11 ºC. Similarly, we observed that Apoferritin starts freezing at −5 ºC and completes freezing at −23 ºC (as shown in figure 2-5). This temperature range is lower than what M. Cascajo-Castresana

et al. reported. This difference could possibly be attributed to variations in droplet sizes and consequently, droplet concentrations. For instance, their droplet assays contained droplets of 50 µl, whereas the largest droplet size in our study was 1 µl. We have previously in this chapter demonstrated that larger droplets freeze at higher temperature ranges compared to smaller droplets, such as nanolitre droplets. This explains the higher temperature ranges for Apoferritin freezing reported by M. Cascajo-Castresana et al. compared to our findings. Furthermore, the highest concentration we used here was 1 µg/µl, whereas their highest concentration was around 0.34 µg/µl. This means that each droplet in their assays contained around 17 times more Apoferritin than our droplets which was 1 µg per droplet. Consequently, a higher protein content per droplet increases the probability of freezing. Nevertheless, our results from size exclusion chromatography (SEC) purified samples confirm that the Apoferritin's efficiency at higher temperatures can be attributed to its aggregates, also referred to as oligomers here.

M. Cascajo-Castresana et al. have dedicated more effort to experimental investigations, particularly focusing on disassembled aggregates and, specifically, monomer cages. One method they employed to probe this phenomenon involved altering the pH and then measuring the frozen fraction of the Apoferritin solution. Across different pH levels ranging from 9.5 to 2, the freezing behaviour of Apoferritin droplets exhibited minimal dependence, with the exception of pH 0, where freezing occurred at lower temperature ranges. This observation can likely be attributed to the loss of subunits from some of the aggregates and monomer-cages in highly acidic environments. This loss of subunits results in changes to the size, shape, and number of the effective ice-active elements. According to M. Kim et al., these disassembled subunits tend to form aggregates at pH levels below 0.8, possibly through van der Waals interactions as well as weak hydrogen bonds [139]. However, the findings of M. Cascajo-Castresana et al. regarding Dynamic Light Scattering (DLS) measurements conducted at pH 0 did not reveal an additional peak corresponding to disassembled subunits. Instead, the peaks corresponding to the original aggregates either increased or decreased. This suggests that the formation of subunit aggregates is not consistently observed, and disassembled subunits may contribute to the existing aggregate count by potentially increasing it. Despite these observations, the freezing behaviour of Apoferritin droplets did not show any improvement. In summary, it appears unlikely that highly acidic conditions will enhance the ice nucleation efficiency of Apoferritin.

Another method employed to investigate the characteristics of these efficient Apoferritin aggregates involved comparing the frozen fraction of droplets that underwent a serial dilution process. The 50 µl droplets at lower Apoferritin concentrations displayed broader temperature ranges for freezing and shifted towards lower temperatures, whereas those at higher concentrations exhibited narrower freezing ranges at warmer temperatures. M. Cascajo-Castresana et al. attributed this phenomenon to the disassociation of Apoferritin monomer-cages into subunits at significantly lower concentrations, which could explain the freezing at lower temperature ranges.

However, our data and characteristic techniques raise doubt on the accuracy of this explanation for few reasons. Firstly, our Transmission Electron Microscopy (TEM) images, captured at lower concentrations, did not provide clear evidence of the existence of subunits as distinct species or aggregates entirely composed of disassembled subunits. Instead, most of the observed aggregates consisted of multiple spherical cages. Therefore, if dilution were indeed causing Apoferritin disassociation, we would expect to observe their aggregates or at least indications of their presence. Moreover, if such an effect were common, it would likely have been widely reported in the biological research literature, especially in electron microscopy imaging, which often involves low concentration samples.

Furthermore, our experiments involving size exclusion chromatography (SEC) for commercial Apoferritin, conducted multiple times (approximately 9 times during this project), consistently yielded three main peaks representing oligomers, dimers, and monomers, respectively, based on their size. Importantly, no unique peaks corresponding to smaller entities like Apoferritin subunits were detected. Similarly, several gel electrophoresis runs for Apoferritin samples at different concentrations (both high and low) did not reveal any bands beyond the dominant monomers, dimers, and oligomers.

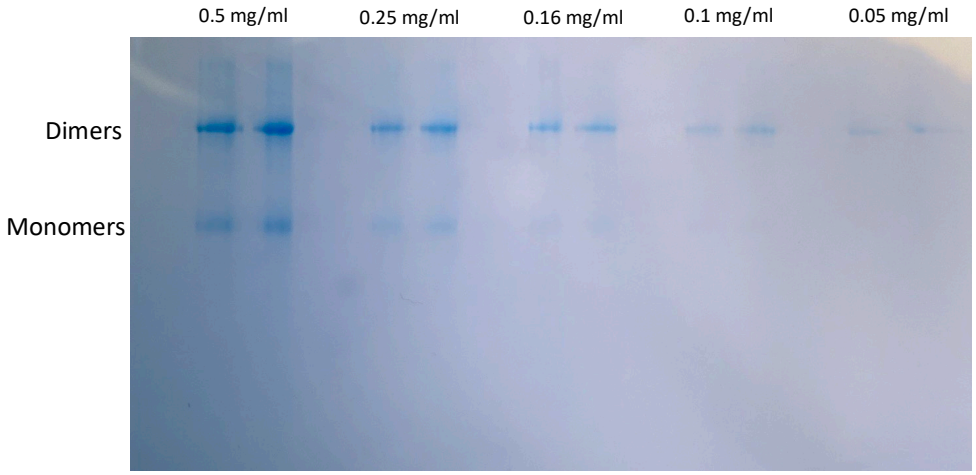

Figure 2-12: A series of dilutions of an Apoferritin sample with a starting concentration of 0.5 mg/ml. There is no clear evidence of the presence of protein disassociated subunits at the low concentrations from the gel electrophoresis bands especially beyond monomer bands. No new bands or bands with increased intensity, such as those higher than dimers, were evident, which could imply the formation of aggregates from these disassociated subunits. In contrast, the density of resolved bands decreased as the concentration was reduced.

An illustrative Native Page gel electrophoresis result of an Apoferritin sample subjected to serial dilution is presented in figure (2-12). This result clearly lacks bands corresponding to disassembled subunits in the highly diluted sample. Furthermore, it does not show any new bands or even an increase in the density of existing bands, such as higher bands than dimers, which could indicate the formation of aggregates from these subunits. On the contrary, the density of resolved bands decreases as the concentration decreases, as would be expected. Loss of subunits from monomer-cages would likely result in bands lower than those of monomers, owing to their smaller size and lower molecular weight compared to a full spherical cage. This characteristic would allow them to migrate further in the gel matrix. If subunits were present, we would anticipate observing a band around 20 kDa, see the protein ladder in figure (2-4) a.

A third possible reason is that our nanolitre droplet results show distinct freezing curves for the three dominant species: oligomers, dimers, and monomers. These species were not clearly resolved from Dynamic Light Scattering (DLS) measurements in the work of M. Cascajo-Castresana et al., nor were they taken into account. The concentration of nanolitre droplets in our dataset represents a much lower protein content compared to the 50 µl droplet assays. The protein content for the three nanolitre intervals was as follows: 1–9 ng, 0.1–0.9 ng, and

0.01–0.09 ng per 10–90 nl, 1–9 nl, and 0.1–0.9 nl droplets, respectively. In contrast, the lowest protein content used for Apoferritin in the data of M. Cascajo-Castresana et al. was around 28 ng per droplet. Therefore, in the case of subunit existence at very low concentrations or in tiny droplets, a significant overlap would occur, making it difficult to separate the frozen fractions of the nanolitre ranges. Such an overlap would indicate the presence of similar ice-active particles, which could either be disassembled subunits or their aggregated forms. Furthermore, the freezing behaviour of these subunits would likely be observed closely to temperatures approaching that of the buffer or water. M. Cascajo-Castresana et al. demonstrated that subunits resulting from heating Apoferritin to 110 ºC froze at low temperature ranges similar to water. The wider range of freezing temperatures in our nanolitre droplets' frozen fraction, as discussed in the previous section, is likely due to variations in the sizes of droplets within each interval. Thus, based on our data, we believe that reducing the Apoferritin concentration leads to a reduction in the number of efficient protein aggregates within the droplets. This decrease results in the abundant but less effective ice-active subforms, such as trimers, dimers, and monomers, start to dominate the freezing process as the temperature decreases. These subforms tend to prevail at lower temperature ranges, thereby accounting for the broader temperature ranges observed in diluted droplets. This aspect will be further investigated in Chapter 3.

Furthermore, Apoferritin and ferritin proteins have shown to be an efficient INPs compared to other protein tested in the same work by M. Cascajo-Castresana et al. for example casein, ovalbumin, hydrophobins, and a yeast ice-binding protein, since they initiate freezing at –10 ºC at higher concentrations and temperature ranges than Apoferritin and Ferritin droplets.

M. Ling et al [71] explored the relationship between ice nucleation activity and the number of protein repeats (16 repeats) for protein strains extracted from Pseudomonas bacteria R10.79 and referred to as INpro. The size of the repeats ranged from 50 to 70 nm, which is comparable to the size of Apoferritin oligomers. The freezing range of 1 µl droplets containing these proteins was between –9 ºC and –20 ºC. This indicates that INpro is an efficient ice nucleating protein however, Apoferritin exhibited freezing at higher temperature ranges compared to INpro.

M. Adams et al. [77] conducted an investigation involving 11 viruses, with only 9 of them displaying ice nucleation activity. These viruses belonged to various families, including Enveloped Icosahedral, Icosahedral, Pleomorphic, and Lemon-shaped viruses. The sizes of the viruses used in the experiments ranged from 85 to 30 nm. Notably, the enveloped virus Phi12, a type that infects Pseudomonas bacteria, was the most efficient virus in the study. The freezing behaviour of 1 µl droplets containing Phi12, with a particle size of 85 nm, appeared within the range of –15 °C and –21 °C. This freezing range is lower than that observed for Apoferritin droplets.

In conclusion, Apoferritin is indeed one of the most efficient ice nucleating particles, especially among biomolecular ice nucleating particles, and thus is worthy of further investigation and study.

2.3.4. Nucleation Rate Coefficient of Apoferritin Subforms

In the classical nucleation theory (CNT), the ice nucleation rate J of pure water is linked to the rate at which water molecules can be added to an ice nucleus, or, more simply, it may be defined as the ice nucleation probability per unit time and volume [113]. In experiments, it is not always straightforward to determine the ice nucleation rate from data, especially for the constant cooling rate approach. In order to obtain J of heterogeneous ice nucleation, constant cooling rate measurements may be interpreted using the Poisson distribution. Using Poisson statistics, the measured frozen fraction is given by the formula [140]:

$$\frac{N_f}{N_L} = 1 - \exp(-J(T).V.\Delta t) \qquad (2-2)$$

where N_f is the number of droplets that freeze during time t, N_L is the number of unfrozen droplets at the start of the time interval Δt, V is the sample/droplet volume and $J(T)$ is the nucleation rate coefficient as a function of temperature and can be generally obtained by [140–142]:

$$J(T) = \frac{-\ln\left(1-\frac{N_f}{N_L}\right)}{\omega.\Delta t} \qquad (2-3)$$

where N_L is the number of liquid droplets at the start of Δt and N_f is the number of freezing droplets during this time interval, ω is a generic symbol for the normalisation parameter, which,

for homogeneous nucleation, represents a droplet's volume, while in heterogeneous nucleation, it stands for the mass of an INP per droplet. Figure (2-13) displays the nucleation rate coefficients per unit mass and time, J_m, for Apoferritin oligomers, dimers, and monomers calculated from frozen fraction data for droplets of 1 µl size. J_m values rise as the temperature decreases as would be expected from classical nucleation theory.

Normalized by the protein mass ($m = C.V$), the resulting J_m for oligomers, dimers, and monomers shows that oligomers are the most active nucleating particles since they cause the droplet to freeze at higher temperatures. Apoferritin dimers and monomers have overlapping freezing temperatures and J_m values, which may be the consequence of the same active INPs in the droplets promoting the freezing of the droplets. Moreover, the density of active sites per unit mass and time suggests that these active sites are few and may be rare INPs, which may be a result of the protein clusters, that are most likely present in droplets with a high protein concentration, this will be investigated in Chapter 3.

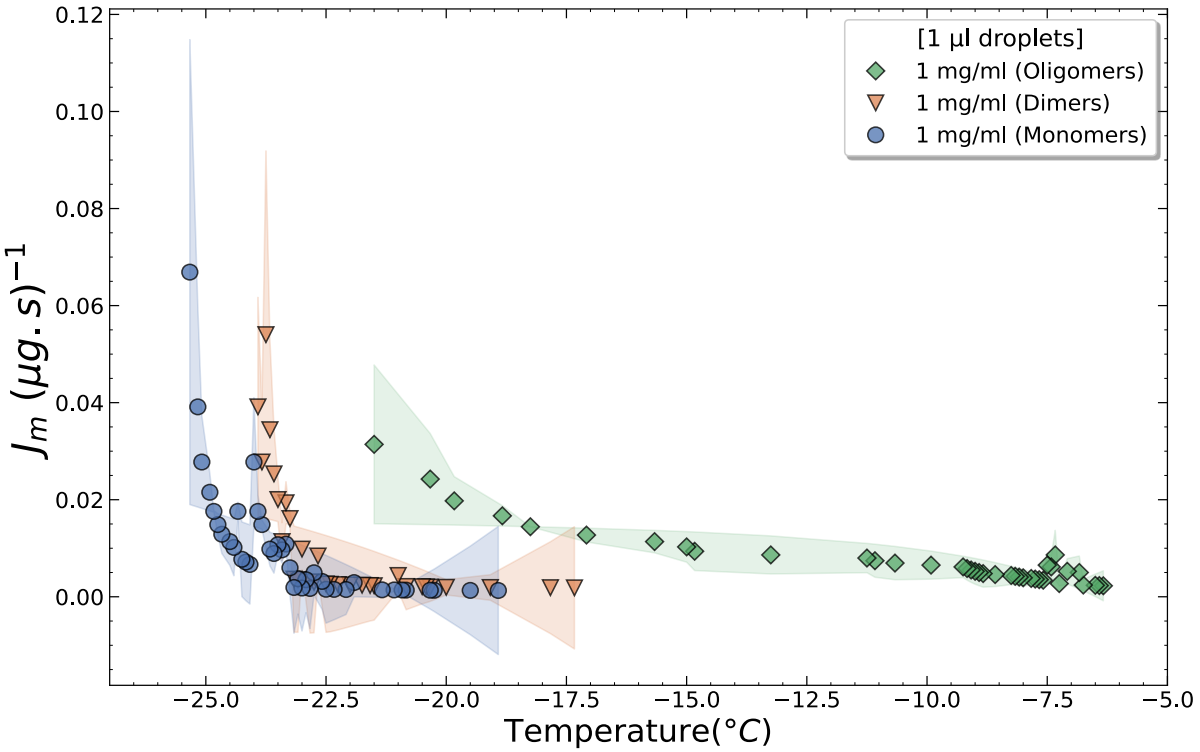

Figure 2-13: The number of nucleation events per unit mass and per unit time, J_m (µg. s)$^{-1}$, for Apoferritin oligomers, dimers, and monomers calculated from frozen fraction data for a droplet size of 1 µl. Oligomers are the most active INP because they initiate the freezing process at higher temperatures. J_m values for dimers and monomers coincide in the initial part of the data, then separate at lower temperatures, which may be related to the effect of rare INPs or protein clusters.

The freezing of droplets by clusters could be responsible for the slowly varying J_m observed at higher temperatures before the data sets for monomers and dimers at lower temperatures. The number of total liquid droplets was significantly reduced at the start of the experiments due to droplets freezing by clusters at higher temperatures. Consequently, at lower temperatures, fewer droplets froze due to dimers and monomers, indicating that clusters were responsible for the preponderance of freezing rather than dimers and monomers.

On the other hand, the nucleation rates J_m of nanolitre droplets at a low concentration of 0.1 mg/ml for each Apoferritin subform were also evaluated, see figure (2-14). A unit mass of oligomers has more active sites that induce a greater number of nucleation events per unit time. The J_m values of dimers are generally greater than those of monomers as anticipated. J_m values for nanolitre droplets are several orders of magnitude higher than those of microlitre droplets. As bigger droplets and higher protein concentration often freeze at higher temperatures, while smaller droplets with low concentration typically freeze at lower temperatures, the nucleation rate coefficient increases as the temperature decreases.

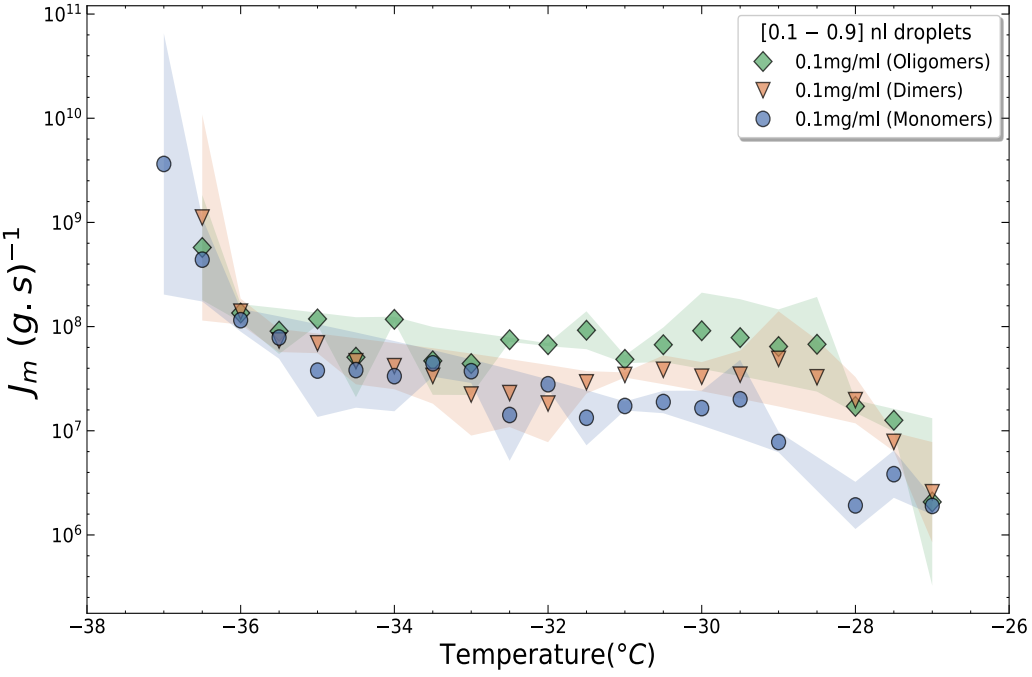

Figure 2-14: Nanolitre droplet nucleation rate coefficients calculated from frozen fraction data for droplets containing 0.1 mg/ml Apoferritin (oligomers, dimers, monomers). The normalised frozen fraction by protein mass and time demonstrates a higher density of active sites for oligomers compared to the same mass of smaller Apoferritin components (dimers and monomers). The shaded areas represent the average with the maximum and minimum values.

To determine values of energy barrier and shape factor for Apoferritin subforms, it is essential to fit the data to the model of classical nucleation theory. However, the calculated nucleation coefficients based on a constant cooling rate method include a great deal of uncertainty, thereby making them difficult to interpret based on classical nucleation theory. Despite the fact that the data obtained by this method are very valuable in determining the general properties of a particular INP with respect to temperature, it is essential to conduct more in-depth studies for Apoferritin subforms using the alternative method of isothermal freezing in order to gain more insight and to be able to compare data to CNT.

2.3.5. Singular Description for Apoferritin Subforms

To calculate the cumulative active sites per unit mass N_m for Apoferritin subforms using the singular model described in Chapter 1, in which the nucleation time is given less weight than INP freezing temperature, N_m can be expressed as a function of temperature as follows [143]:

$$N_m(T) = \frac{-\ln(1 - f_{ice}(T))}{m} \qquad (2-4)$$

where $f_{ice}(T)$ is the fraction of frozen droplets per total number at temperature T and m is the protein mass in a droplet. As expected, oligomers gave the highest N_m values for Apoferritin subforms, followed by dimers and then monomers as shown in figure (2-15) a for nanolitre droplets.

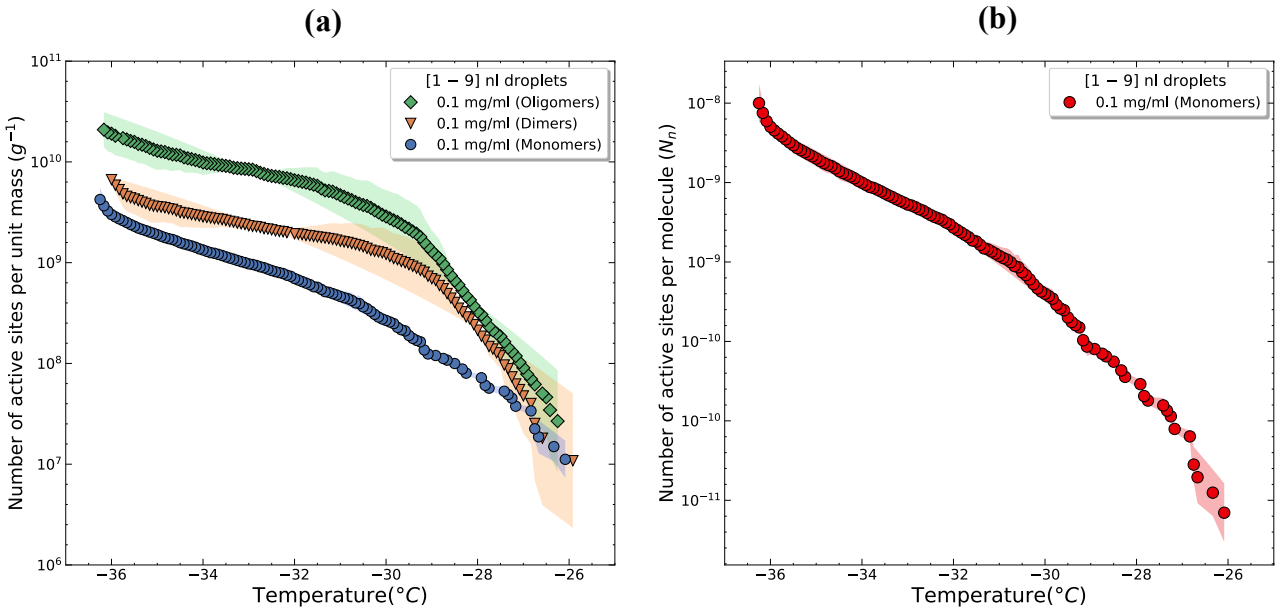

Figure 2-15: (a) The temperature-dependent number of active sites per unit mass for Apoferritin subforms, N_m, for nanolitre droplets. (b) The number of active sites per Apoferritin monomer N_n. The shaded regions represent the mean together with the maximum and minimum values.

Since oligomers and dimer SEC samples contain mixed subforms but monomer SEC samples are quite pure, it is possible to quantify the cumulative number of active sites per single molecule. By normalising monomers nanolitre observations, the number of active sites per monomer N_n can be given by [144]:

$$N_n(T) = \frac{-\ln(1 - f_{ice}(T))}{m\left(\frac{N_A}{M_W}\right)} \qquad (2-5)$$

where N_A is Avogadro number and M_W is the molecular weight of a single Apoferritin monomer (450 kDa). In figure (2-15) b, the resultant N_n of monomers ranges between (10^{-11} – 10^{-8}) active sites per monomer cage. These are very small values, best explained by assuming that the active site fraction values correspond to a small number of ice active monomers among a majority of inactive monomers, because active sites do not exist as fractions of sites but as single sites. Some studies in the literature argue that biomolecules like proteins and viruses are often regarded as having a small role in the nucleation of ice in the atmospheric system, nevertheless the rare biomolecules, such as aggregates and clusters are thought to make a significant contribution [77,97,121].

A second argument is that all monomers are weakly ice-active, making it challenging to define a characteristic temperature thus, the singular model cannot be applied. In addition, since the INP sample, which is a monomer sample in this instance, is uniform, the singular model is more useful if the INP sample used has a broad range of ice nucleating efficiency.

2.4. Conclusion

In summary, we investigated heterogeneous ice nucleation by biomolecules using a constant cooling rate approach, employing the Apoferritin protein as an example. Size exclusion chromatography (SEC) was used to separate Apoferritin into its three components, oligomers, dimers, and monomers. The frozen fractions were evaluated as a function of temperature. For microliter droplets, the most ice-active subform was oligomers, followed by dimers and monomers, the least effective INP. In the nanolitre droplet regime, the frozen fraction exhibited comparable findings to the microlitre droplets for the three Apoferritin components, with the exception of a shift in the freezing temperature range towards lower temperatures. The nucleation rate coefficient J_m was next examined by converting the frozen fraction measurements using the Poisson distribution. In bigger droplets, it was observed that the dimer and monomer nucleation rate coefficients overlapped, which may be attributed to rare INPs or a protein clustering effect. For nanolitre droplets, the J_m was also higher for oligomers than dimers and monomers. The number of active sites per particle was also calculated for monomers, and in general, the ratio of active monomers to total monomers is low, or the singular model is less applicable. Due to the high uncertainty in nucleation coefficients obtained from the constant cooling rate method, which makes it difficult to interpret and obtain classical nucleation theory parameters, we will further investigate the ice nucleation rate of Apoferritin via a time-dependent approach and seek the validation of CNT through the quantification of fundamental parameters.

3. ISOTHERMAL MEASUREMENTS

3.1. Introduction

Constant cooling rate experiments for homogeneous and heterogeneous ice nucleation provide empirical evidence that the ice nucleation of immersion freezing droplets is temperature dependent. For some ice nucleation systems, measuring the frozen fraction of droplets as a function of temperature serves to provide an overview of a sample's ice nucleating ability. However, measuring the nucleation rate using this approach may be challenging due to the high level of noise and ambiguity encountered while interpreting the data. Ice nucleation is not only a temperature-dependent phenomenon, but also a time-dependent process. According to the classical nucleation theory, the formation of a stable critical nucleus is stochastic and therefore occurs at random times.

Isothermal measurement is another experimental approach to assess the ice nucleation rate of immersion freezing droplets, and shows how the fraction of unfrozen droplets varies as a function of time. Sear categorised the data derived from time-dependent observations of nucleation into three categories: 1) time-independent freezing rate, which gives a straight line with a constant slope when the logarithm of the unfrozen fraction is plotted as a function of time; 2) decreasing freezing rate giving an upward bending curve; (see Chapter 1) and 3) increasing freezing rate giving a downward bending curve (will be discussed in Chapter 4) [145]. The first two categories for heterogeneous ice nucleation are heavily influenced by sample properties, such as homogeneity, purity, and size.

Despite the fact that it is not feasible to create a sample that comprises 100% identical ice nucleators, this challenge may be approached statistically. A sample of ice nucleating agents can be represented by a probability distribution function that assigns each particle in a sample a specific nucleation rate J as explained in Chapter 1. The mean of this distribution determines how effective this particle is as an ice nucleating agent, whereas the standard deviation gives an approximation of the purity and uniformity or the variation of this particle in the sample, which determines whether the plot of the logarithm of the unfrozen fraction is linear or nonlinear, as studied in depth by Knopf et al. [141,146].

The majority of ice nucleating particles, particularly inorganic nucleators, are highly varied, and they are difficult to separate and purify, which increases the uncertainty of finding the nucleation rate from the collected data. Proteins can be excellent models for ice nucleating agents due to their high degree of homogeneity and responsiveness to changes in different environmental conditions such as pH and temperature, and the possibility for control over their synthesis and surface functionalization. Additionally, there are various reliable techniques for their purification and characterisation that enable the separation of larger proteins from smaller ones. Here, Apoferritin is used as a model ice nucleating agent for immersion freezing isothermal measurements. Size exclusion chromatography is used to separate monomers and dimers prior to measurement. Here, we will evaluate the nucleation rate of monomers and dimers of Apoferritin using the isothermal approach in order to determine if a simple aggregation, such as the dimer, is more effective than the monomer at ice nucleation. In addition, we will fit the results to classical nucleation theory to extract plausible model parameters for Apoferritin clusters, dimers and monomers.

3.2. Materials and Methods

3.2.1. Apoferritin Preparation

Materials and purification of Apoferritin were determined using the same methodological protocols as in Chapter 2.

3.2.2. Droplet Assays and Freezing Experiments

Isothermal measurements were carried out using the same setup as in Chapter 2. Each droplet assay consists of 10 droplets of µl size. The rate of cooling from the initial temperature to the desired temperature was set at 50 °C /min. The temperature was held for two to three seconds before freezing images were captured.

3.2.3. Data Analysis of Immersion Freezing

The unfrozen fraction of isothermal measurements was obtained by applying the following formula:

$$Unfrozen\ fraction = \frac{N_{liq}(t)}{N_{tot}} \qquad (3-1)$$

where N_{tot} is the total number of liquid droplets at the start of the run and $N_{liq}(t)$ is the number of unfrozen droplets at time t. The nucleation rate was calculated using the logarithmic plot of the unfrozen fraction vs. time.

3.2.4. Apoferritin Dimers/Monomers Ratio in SEC Samples

Monomers are the most stable subcomponents of Apoferritin, whereas dimers of Apoferritin may dissociate and generate a dimer-monomer mixed solution over time. Consequently, the ratio of monomers to dimers must be approximated in ice nucleation measurements. The ratio was obtained by evaluating an image of the protein's bands using the ImageJ tool for analysing gel electrophoresis bands. The result is a profile map of the gel lanes containing dimers and monomers that displays the peak density of each band. The tool also estimates the size of this peak; the size of dimers peak/monomers peak provides a useful approximation of the sample's monomer-to-dimer ratio. Figure (3-1) is a pie chart illustrating this ratio for the two samples used to determine the dimer nucleation rates.

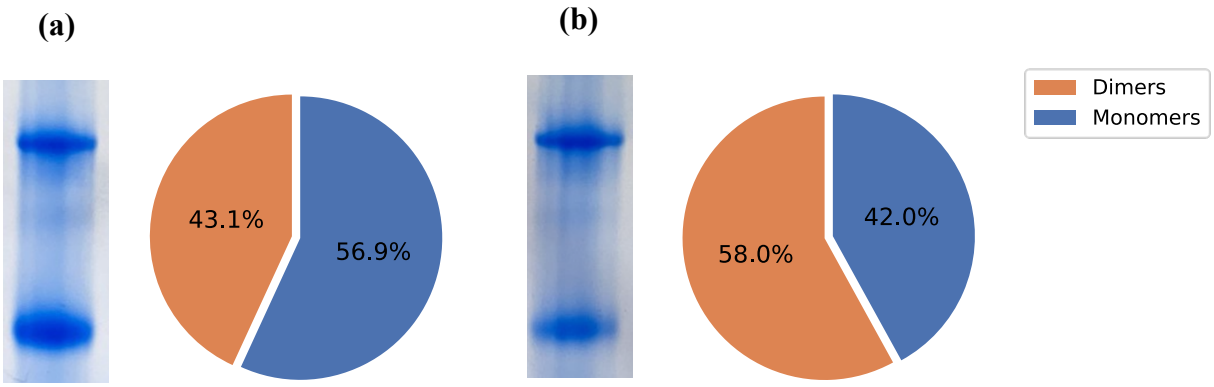

Figure 3-1: The ratio of dimers to monomers in SEC dimer samples is represented by blue native gel electrophoresis bands and pie charts. (a) Fraction 1 has a greater proportion of monomers (57% - lower band) than dimers (43% - upper band). (b) Fraction 2 of the blue bands analyses showed a greater dimer to monomer ratio of 58 % to 42 %.

3.3. Results and Discussion

3.3.1. Immersion Freezing Isothermal Measurements

Monomers were the most abundant and smallest sub-form in the commercial horse spleen Apoferritin. As a result, a sample containing pure monomers is quite likely to be obtained from size exclusion chromatography (SEC). Furthermore, they are very stable compared to higher Apoferritin conformations, such as dimers, since they are the smallest native unit of Apoferritin and their dissociation into subunits could only occur under extreme chemical and physical conditions [125,128]. Nevertheless, monomers may combine to create dimers, but this process is very gradual and can take months, while dimers can break down into monomers in a matter of days or weeks. However, like most ice nucleating particles, their surface structure could vary, despite the proteins being nominally identical. TEM images in Chapter 2 and the literature suggest that there is some variation in the structure of Apoferritin [147–150].

When Apoferritin monomers were evaluated as an ice nucleating agent in isothermal freezing experiments, both linear and nonlinear curves were observed for the time dependence of the logarithm of the unfrozen fraction. Figure (3-2) illustrates the log $(\frac{N_{liq}}{N_{tot}})$ of monomers at two different concentrations and temperatures. At the higher temperature (–23 °C), monomers gave nonlinear curves. This indicates that the data cannot be described by a single freezing rate R. However, when the freezing rate was measured at a slightly lower temperature, such as –23.5 °C, for both concentrations, the number of unfrozen droplets decreased for each with a constant rate over time. Hence, it was possible to fit the log $(\frac{N_{liq}}{N_{tot}})$ to a straight line and estimate the mean freezing rate directly from the slope of the line, as well as the value for goodness of fit, R^2, which was close to one (figure 3-2).

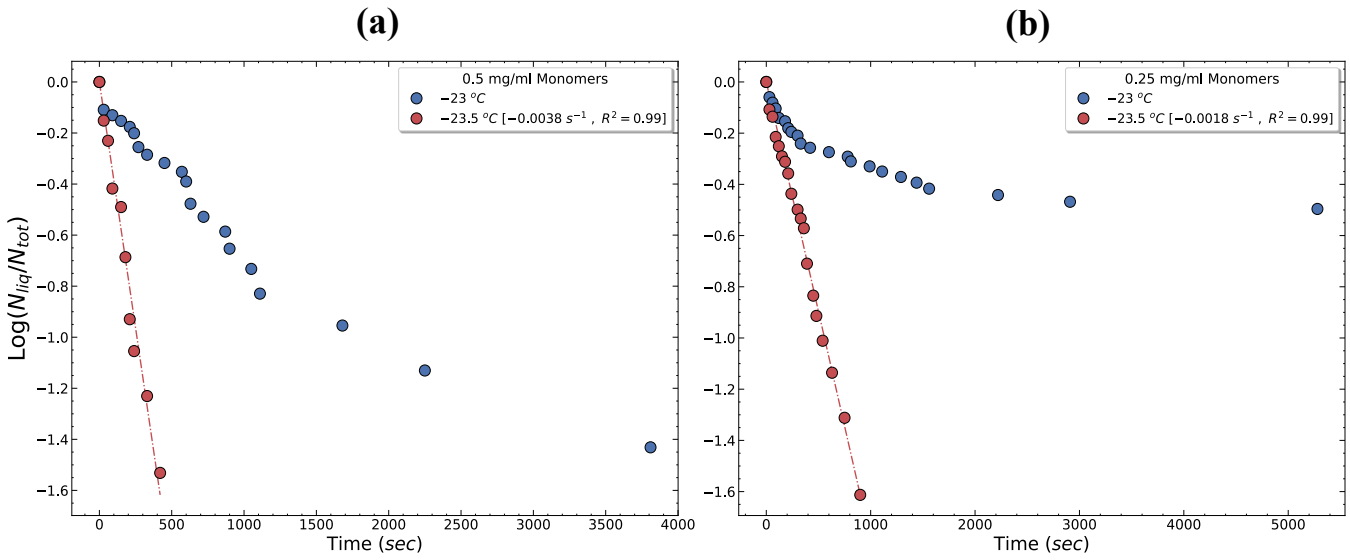

Figure 3-2: Logarithm of the unfrozen fraction of Apoferritin monomers as a function of time for two different concentrations for 1µl droplets cooled at 20 ºC/min. At the higher temperature −23 ºC (shown in blue in a and b), the unfrozen fraction curve demonstrates a nonlinear relationship over time. This indicates that the freezing rate R per droplet is not single-valued. At the lower temperature of −23.5 ºC (red in a and b), the logarithm of the number of unfrozen droplets decreases at a constant rate over time. The slopes and goodness of fit are given in the legends.

Although monomer samples were obtained by the size exclusion chromatography (SEC) it seems that the droplets may also contain a small number of highly efficient nucleating agents namely, protein clusters in addition to a large number of less efficient ones which in this case are either the monomers/dimers or a combination of these and less-efficient clusters. Therefore, at higher temperature the most efficient INPs may dominate the freezing whereas at lower temperature the more abundant but less efficient may dominate. This hypothesis could be tested by fitting the non-linear data in figure (3-2) to a discrete distribution model namely a Poisson distribution to represent the contribution of rare INPs which are clusters whereas the linear data could be fitted to a sum of two Poisson distributions to represent the contribution of clusters and more abundant, less-efficient INPs. If the number of efficient clusters in a droplet is n_c and the number of the less efficient ones is n_m, then the probabilities of having n_c and n_m in a droplet can be given by:

$$p(n_c) = \frac{(\lambda_c)^{n_c}}{n_c\,!}\exp(-\lambda_c), \quad p(n_m) = \frac{(\lambda_m)^{n_m}}{n_m\,!}\exp(-\lambda_m) \qquad (3-2)$$

where λ_c and λ_m represent the mean number of active clusters per droplet and the mean number of less active INPs per droplet, respectively. Hence the unfrozen fraction of the droplets can be given by:

$$\frac{N_{liq}}{N_{tot}} = p(n_c)\, exp(-[n_c\, j_c(T)]\, t\,) \qquad (3-3)$$

$$\frac{N_{liq}}{N_{tot}} = \sum_{n_i} p(n_i)\, exp(-[n_i\, j_i(T)]\, t\,) \qquad (3-4)$$

where $j_c(T)$ is the nucleation rate per cluster, $j_m(T)$ is the nucleation rate per less active INP and t is the measured time interval. For example, equation (3-3) applies when only clusters are important whereas equation (3-4) applies when both clusters and less efficient INPs are important. Figure (3-3) shows the fitted log $(\frac{N_{liq}}{N_{tot}})$ results of the two concentrations at two different temperatures, and table (3-1) summarizes the corresponding fit parameters.

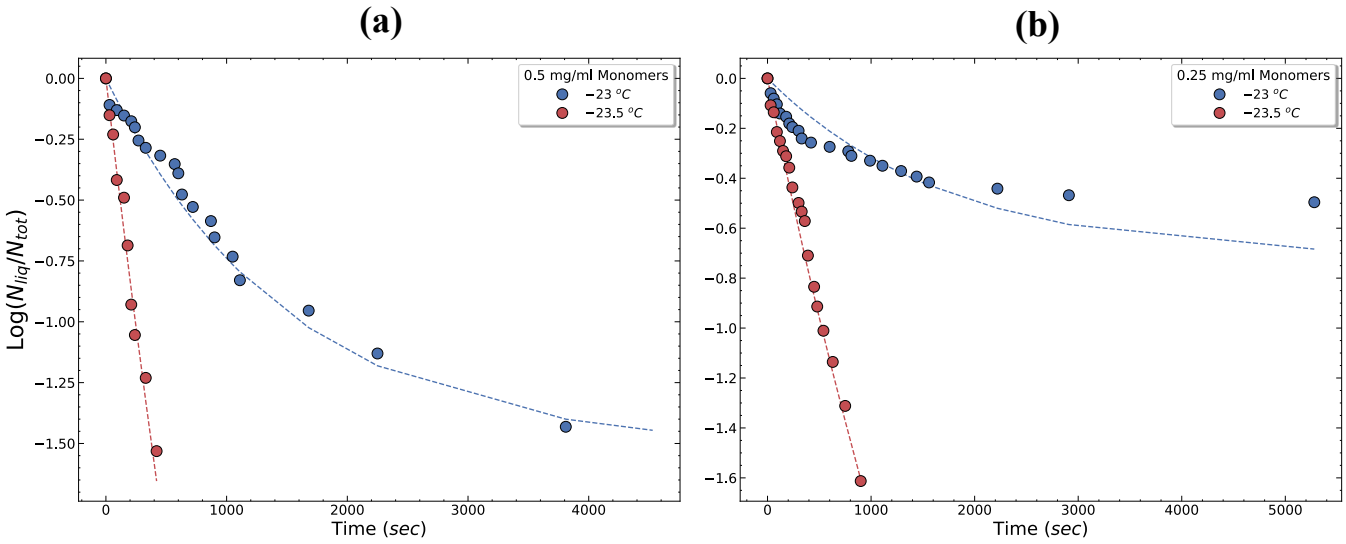

Figure 3-3: he data in figure (3-2) (curves and lines) were fitted to equations (3-2), (3-3) and (3-4) at two different temperatures and concentrations.

At higher temperature, –23 °C, it shows that there is a small mean number of active clusters λ_c in a droplet with a high j_c value, therefore the curved log $(\frac{N_{liq}}{N_{tot}})$ will be dominated by these clusters. Moreover, λ_c per droplet doubles when the concentration of protein is doubled. At lower temperature, –23.5 °C, the contribution of the less efficient INPs increases, λ_m, indicating that at lower temperatures a greater number of less efficient INPs may dominate the

freezing in addition to the highly active clusters which could explain a linear log ($\frac{N_{liq}}{N_{tot}}$). The nucleation rate per INP increases for both clusters and less efficient INPs when the temperature decreases, additionally the mean number of active INPs per droplet is proportional to the protein concentration of droplets.

Table 3-1: Fitting parameters for Apoferritin clusters and less efficient INPs for two different concentrations.

Temperature [°C]	Concentration [mg/ml]	λ_c [INP]	j_c [s^{-1}]	λ_m [INP]	j_m [s^{-1}]
–23	0.5	4	0.02		
	0.25	2	0.02		
–23.5	0.5	4	0.05	20	0.02
	0.25	2	0.05	10	0.02

3.3.2. Influence of Cooling Rate

The cooling rate of the previously given data was 20 °C/min, which is a moderate rate of cooling. During the time-dependent freezing experiments, it was observed that when the cooling rate was set to be slow, once the programmed temperature was reached, the number of unfrozen droplets that survived freezing was small in comparison to the total number that was present at the beginning. A slow cooling rate means that droplets will be exposed to a prolonged period of cooling, which will ultimately result in random freezing prior to reaching a particular set temperature. In addition, freezing may be caused by dust and contaminants, even though the likelihood of their presence is low. As a consequence, the log ($\frac{N_{liq}}{N_{tot}}$) curves and straight lines sometimes only reflects a tiny amount of the protein sample under study; for example, the straight line may only represent the freezing rate of 10 to 20 % of the total droplets (the number of unfrozen droplets at the start of the isothermal measurement). For long experiments needing more than an hour, e.g. for low protein concentrations, water, or buffer, the surrounding air begins to condense and generate picolitre to nanolitre droplets on the surface of the substrate, which leads to dendritic ice crystals when they freeze. Sometimes frost forms before the main droplets freeze, and if the frost reaches an unfrozen droplet, it can induce nucleation. A layer of mineral oil could prevent such condensation problems, but it also affects the freezing rate

because the water/air interface of typical droplets, which resemble cloud droplets, will change to a water/oil interface. Droplets with and without oil layer will be discussed in Chapter 4.

When the cooling rate was optimised and increased to 50 ºC/min, it was feasible to lower the freezing temperatures of the droplets to lower ranges than when the rate was 20 ºC/min see figure (3-4). Although the same log $(\frac{N_{liq}}{N_{tot}})$ pattern of nonlinearity at higher temperatures and linearity at lower temperatures was observed, the whole pattern was shifted toward lower temperatures compared to the slow cooling rate data, and any overlap with dust and contaminants was likely avoided. Also, when the programmed temperature is reached, the number of unfrozen droplets is significantly larger. Thus, more than half of the entire number is included, resulting in a higher fraction of the protein sample being represented in the data. As a result, because the temperatures have been shifted toward lower ranges, the time required for freezing is less than it would be with a slow cooling rate, minimising the formation of dendritic ice crystals or frost and eliminating the need to coat the droplets with oil, particularly the microlitre droplets. For all forthcoming results, the rate of cooling will be set at 50 ºC/min.

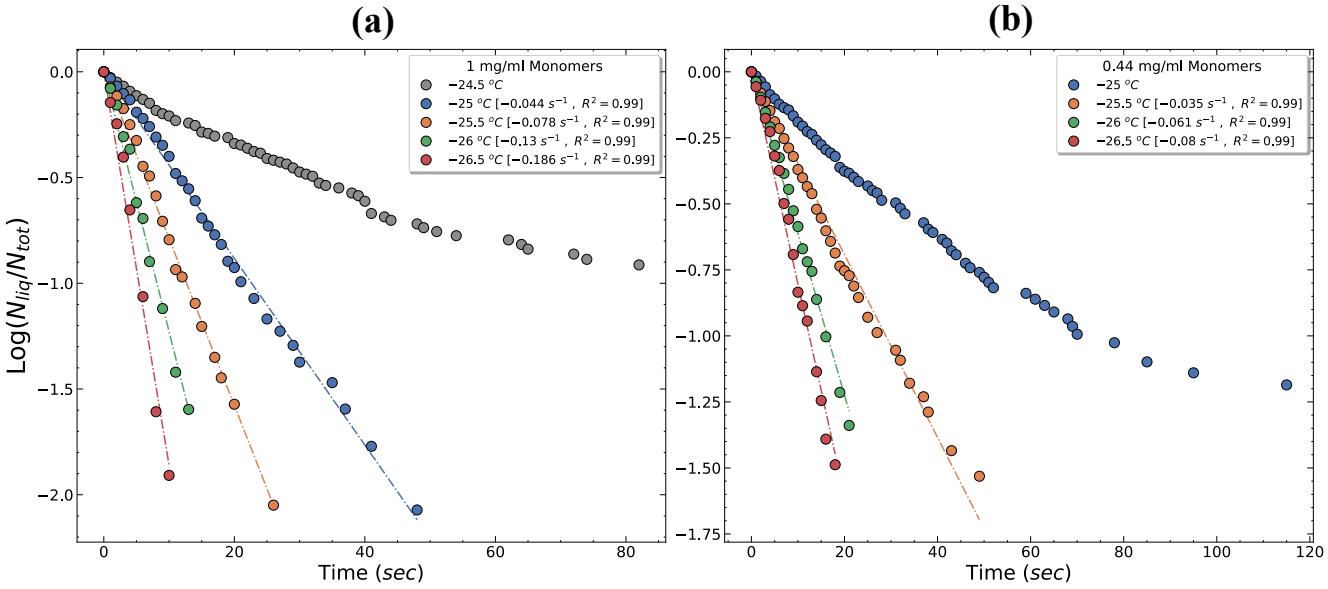

Figure 3-4: Isothermal measurements of Apoferritin monomers (1 and 0.44 mg/ml) for 1µl droplets cooled at 50 ºC/min. The plot of the logarithm of the unfrozen fraction curves with time at higher temperatures. When the temperature lowers, the unfrozen fraction is a straight line, and the nucleation rate values increase. The slopes and goodness of fit are shown in the legends.

The data were fitted to equations (3-2), (3-3) and (3-4) and shown in figure (3-5). The obtained parameters in table 3-2 suggest that the curved log ($\frac{N_{liq}}{N_{tot}}$) is a result of a small number of efficient clusters dominating the freezing at higher temperature. At lower temperatures, the mean number of less active INPs contributing to the freezing with the clusters increases, resulting in a linear log ($\frac{N_{liq}}{N_{tot}}$). The mean number of active INPs per droplet is proportionate to the protein concentration. The nucleation rate per cluster and per less efficient INP increases with decreasing temperature as expected.

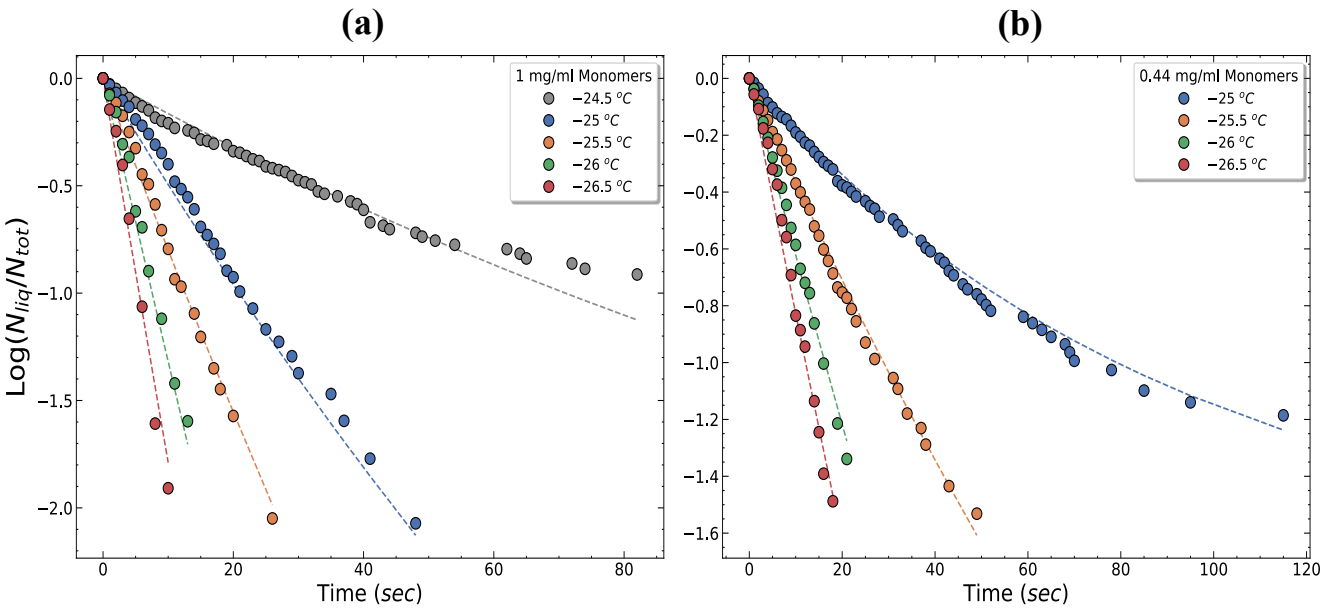

Figure 3-5: Data in figure (3-4) were fitted using Poisson distribution for curved log ($\frac{N_{liq}}{N_{tot}}$) whereas for linear ones two Poisson distributions were used.

This result is consistent with the previous result for the slow cooling rate, 20 °C/min. However, to detect the contribution of clusters to the freezing, we should vary the concentration of the droplets using monomer and dimer samples. If the freezing rate of monomers and dimers at a given temperature is the same this could indicate that the freezing is dominated by protein clusters. This will be explored in depth in the next section.

Table 3-2: Fitting parameters for Apoferritin clusters and less efficient INPs with a droplet concentration of 1 and 0.44 mg/ml.

Concentration [mg/ml]	Temperature [°C]	λ_c [INP]	j_c [s^{-1}]	λ_m [INP]	j_m [s^{-1}]
1	–24.5	10	0.22		
	–25	10	0.45	75	0.03
	–25.5	10	0.55	75	0.08
	–26	10	0.65	75	0.16
	–26.5	10	0.75	75	0.27
0.44	–25	5	0.47		
	–25.5	5	0.55	37.5	0.07
	–26	5	0.65	37.5	0.16
	–26.5	5	0.75	37.5	0.22

3.3.3. Influence of Apoferritin Concentrations on Droplets Freezing Rate

Apoferritin samples have previously been shown to exhibit a consistent linear decrease in the logarithm of unfrozen fraction as a function of time, which may be described by a single freezing rate. As a result, it is possible to investigate Apoferritin's nucleation behaviour in detail and compare the efficiency of its purified sub-forms, for example, changing the amount of these sub-forms in droplets to see how the freezing rate varies as temperatures are lowered. When freezing droplets containing monomers only and droplets containing a fixed proportion of monomers to dimers, (figure 3-6), the mean freezing rate varies in proportion to the concentration, as it decreases by a factor of 2 when the concentration is halved and vice versa. This is important as it shows that the mean freezing rate is dominated by the protein sample (dimers and monomers) rather than e.g. dust from the atmosphere.

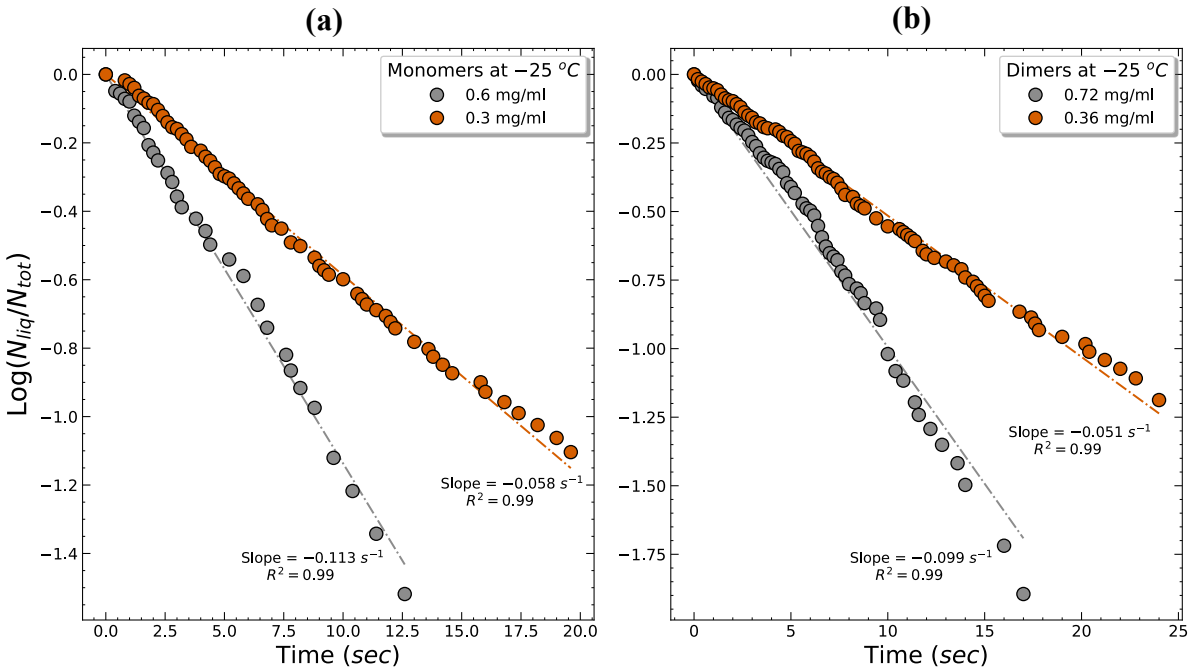

Figure 3-6: The freezing rate of Apoferritin monomers and dimers at 2 different concentrations with 2µl droplets at −25 °C. (a) The freezing rate due to monomers is proportional to their concentration, therefore doubling the concentration doubles the slope. (b) The freezing rate of a sample consisting of 57 % monomers and 43.1 % dimers likewise doubles.

More examples of monomers and dimers that demonstrate a concentration dependence of their freezing rate at a lower temperature and with lower concentrations are shown in figure (3-7). Dimers are the smallest aggregated forms of Apoferritin. Since they consist of two bonded monomers, they are bigger than monomers and include a potential active nucleation site, their junction in the centre. Theoretically, a dimer could therefore be much more effective as an ice nucleating agent than a monomer. However, the freezing rate values of monomer and dimer samples in figures (3-6), (3-7) indicate that the active INPs are almost equally effective in both cases. Comparable concentrations of both resulted in essentially similar slopes. Thus, the cause of freezing is the same for both kinds of sample.

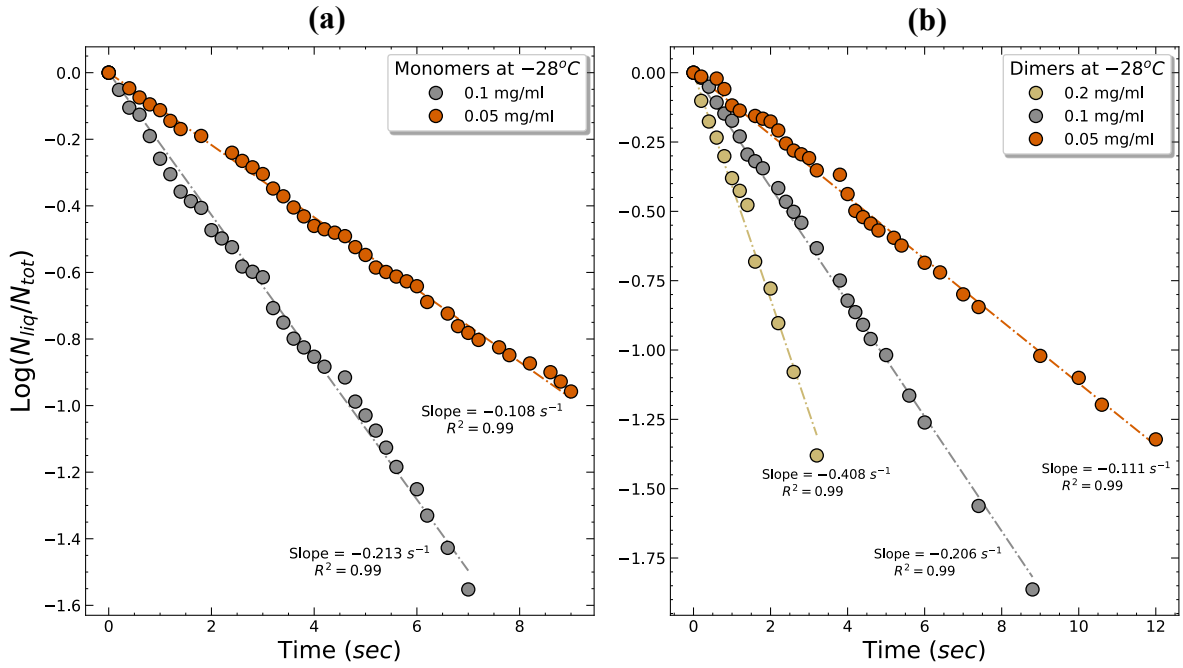

Figure 3-7: Examples of freezing rate dependence on concentration at −28 °C for monomers (a) and 58% dimers / 42% monomers (b). The freezing rates of monomers and dimers are comparable at their respective concentrations, indicating that their ice nucleation sources are similar.

Our hypothesis is that at higher temperatures, Apoferritin clusters dominate the mean freezing rates, however at lower temperatures, dimers or monomers begin to dominate the mean freezing rates. In order to examine this hypothesis at lower temperatures, the concentration of droplets containing dimers and monomers should be decreased to reach these temperatures. At low concentrations e.g. 0.025 mg/ml in figure (3-8), the freezing rates for monomers and dimers begin to show clearly different values. At lower temperatures, monomers have a lower mean freezing rate than dimers, which is reasonable given that dimers are larger in size and have a candidate active site, the junction at the centre. This hypothesis is consistent with the explanation given in sections 3.3.1 and 3.3.2, that at higher temperatures active clusters dominate the freezing rate while at lower temperatures, less active INPs start dominating the freezing rate, and it was possible to test this hypothesis experimentally with isothermal measurements and directly extract the mean freezing rates from the slopes.

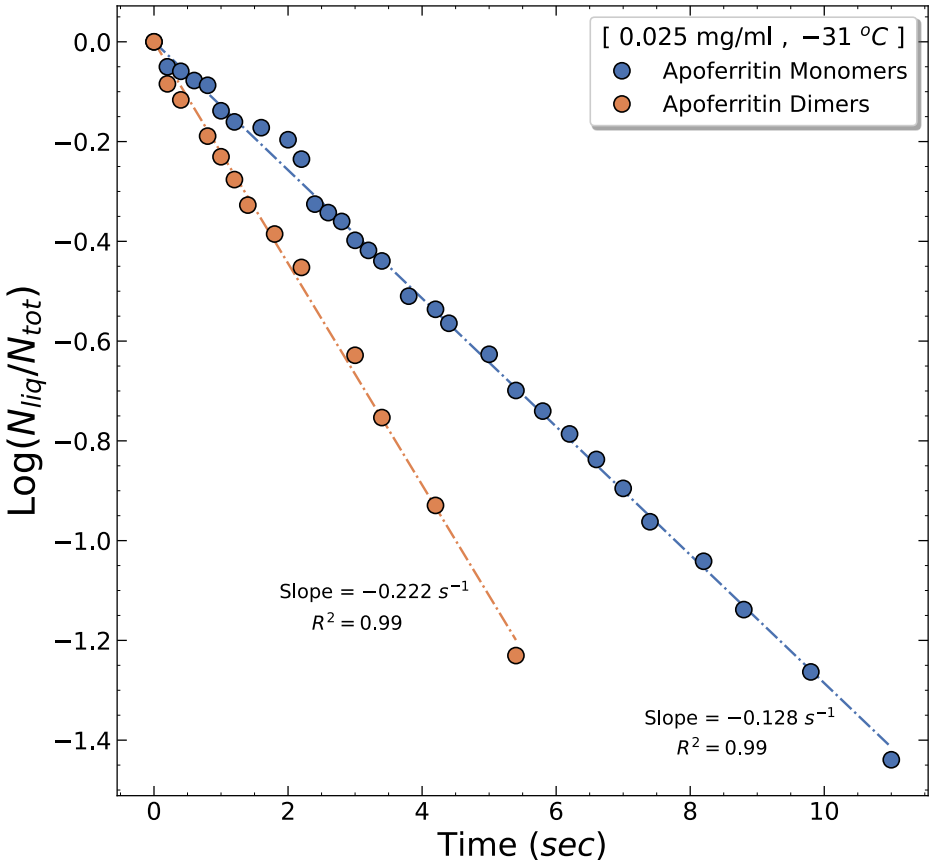

Figure 3-8: At low temperatures and concentrations, such as 0.025 mg/ml, the freezing rates for monomers and dimers begin to diverge significantly.

One hypothesis that needs to be investigated is that as the droplets cool over a period of time, dimers, which are known for their relatively fast disassociation rate, will break down to monomers. Alternatively, it could be the case that monomers dimerize during freezing. Freeze-thaw tests on a sample with a certain initial dimer-to-monomer ratio were a convenient means to test this hypothesis. An array of droplets was cooled until they froze, after which they were allowed to melt and refreeze; the freeze-thaw cycles were repeated up to 10 times. The droplets that underwent these cycles were then collected for native PAGE gel electrophoresis to determine if the ratio of monomers to dimers exhibited a significant change in relation to the number of freeze-thaw cycles (see figure 3-9). The results indicate that the monomer/dimer ratios did not change significantly as the number of freeze-thaw cycles increased.

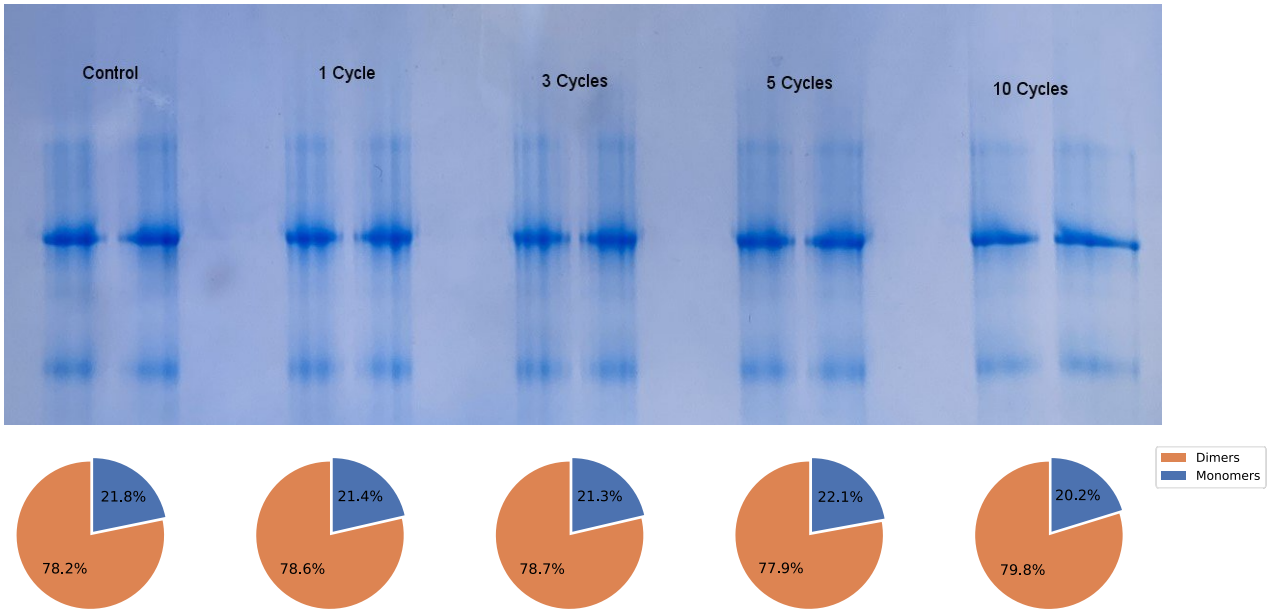

Figure 3-9: Experiments of freezing and thawing protein droplets over a number of cycles. According to the results of gel electrophoresis, the ratio of monomers to dimers is almost constant regardless of the number of cycles. It demonstrates that monomer dimerization or dimer disassociation does not occur within the time scale of the experiment.

3.3.4. The Influence of a Constant Number of Apoferritin Monomers on the Freezing Rate of Droplets of Different Volumes

The effect of concentration on the freezing rate may also be studied by observing the same amount of protein in droplets of varying volumes. Here, we shall examine the isothermal freezing rate of droplets of different volumes, such as 1µl, 8µl, and 27µl, containing the same number of monomers, such that all droplets of different volumes have 1.11 nmol of monomers. Figure (3-10) represents the results of this experiment at –26 ºC.

Despite bigger droplets often being avoided because they may contain more contaminants and dust than smaller droplets owing to their size, which causes them to freeze faster than smaller droplets, this was not the case at all in this experiment. Compared to 8µl and 27µl droplets containing the same number of proteins, 1µl droplets showed the greatest freezing rate. The volume of the droplets was selected to vary the ratio of droplet volume to surface area, therefore 8µl has a ratio of 2 and 27µl has a ratio of 3 times that of the 1µl droplet.

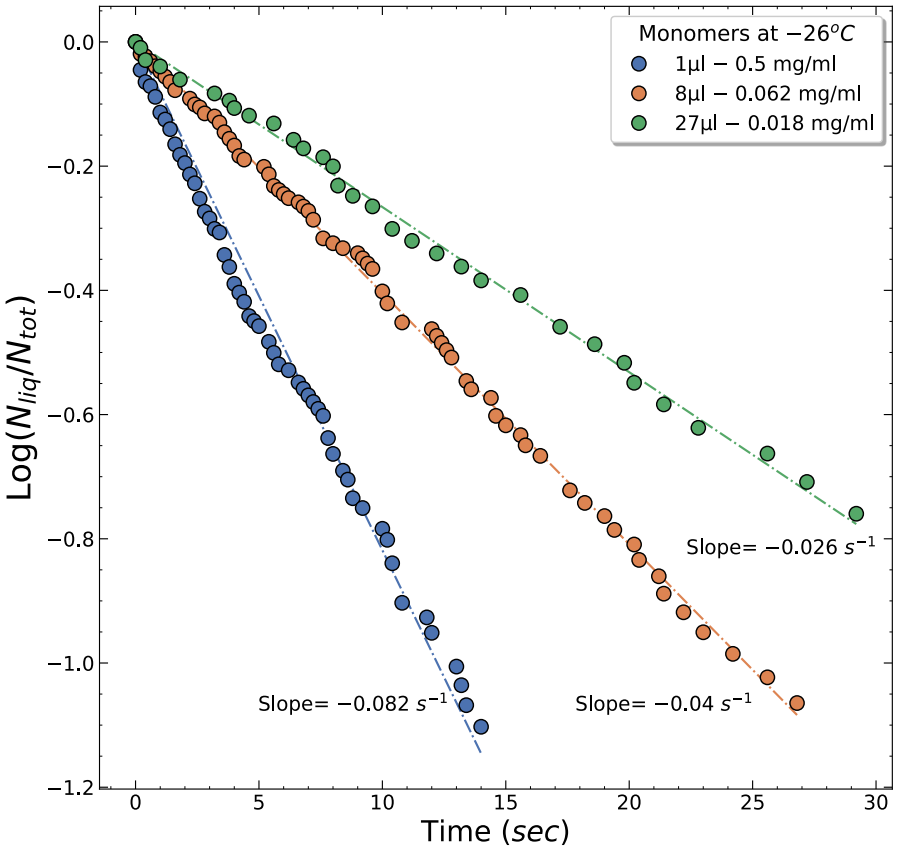

Figure 3-10: The rate of freezing of 1.11 nmol of Apoferritin monomers in 3 different droplet volumes. The size of the droplet was chosen to vary its volume to surface area ratio, which is for the 8µl and 27µl droplets is 2x and 3x respectively the value for the 1µl droplet. At −26 ºC, the data linearizes with 1µl droplets having a nucleation rate that is two times greater than 8µl droplets and three times more than 27µl droplets. Under the hypothesis of protein adsorption at interfaces (water/air and water/solid) ice nucleation may induce at interfaces, in particular for bigger droplets with low concentrations compared to those with high concentrations. This seems to indicate a correlation between freezing rate and droplet surface area.

There are a number of studies on the tendency of proteins to form thin films through self-assembly on surfaces [151–155]. This tendency depends on a number of variables, one of which is the concentration of proteins in the solution, which can impact the adsorption rate of proteins at the surface over time [156]. Measuring the contact angle is a simple method for determining if proteins are adsorbed to the droplet surface. It is generally known that the surface tension of a liquid reduces as proteins are adsorbed to its surface, and that this reduction accelerates as the protein concentration increases [157]. We evaluated the contact angle of 1ul and 8ul droplets at two different concentrations, 0.5 mg/ml and 1 mg/ml. The average contact angle (CA) for both droplet sizes at a given concentration was roughly equivalent. The average

CA for 0.5 mg/ml was 113° ± 0.34°, whereas it was 95° ± 0.6° for 1 mg/ml. In addition, the drop in contact angle was greater for 1mg/ml than for 0.5 mg/ml, with decreases of 4.34° and 2.1°, respectively, after a 10-minute period. It suggests that high concentration droplets show lower CAs and low concentration droplets show larger CAs. This is possibly due to the increasing adsorption of proteins at the droplet's surface as the number of proteins per unit volume increases. The complex mechanism of protein adsorption is outside the scope of this thesis, however the results in figure (3-10) indicate a correlation between the freezing rate and the droplet surface area.

If the findings are to be interpreted by the hypothesis of protein adsorption tendency at interfaces, as seen in figure (3-11), then a hemispherical liquid droplet placed on a solid surface would have two principal interfaces: the water/air interface and the water/solid interface. The 1ul droplets contain a large number of monomers confined in a small volume, which increases the rate of protein adsorption at interfaces. Excess monomers either contribute to the thickening of surface monolayers or begin to cluster in the bulk volume, all of which can increase the probability of ice nucleation.

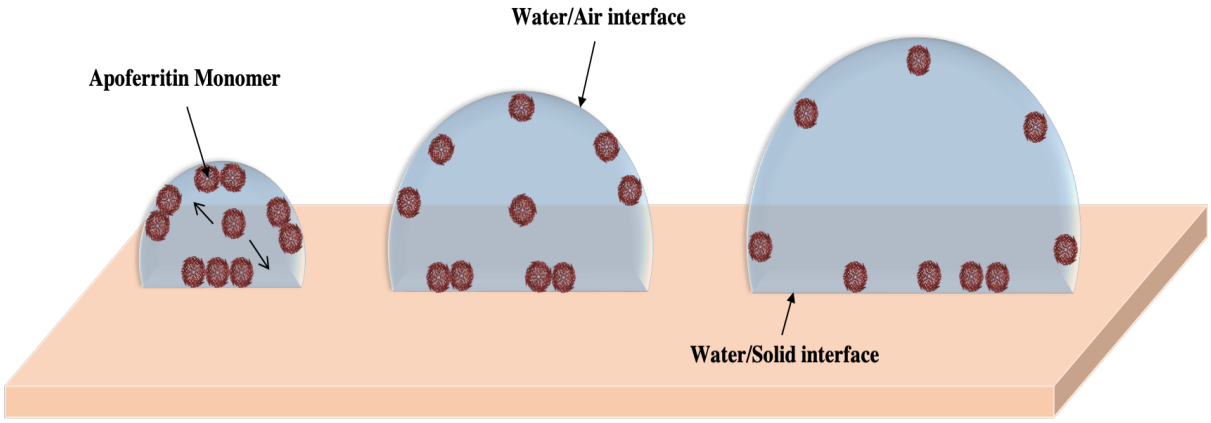

Figure 3-11: A simple illustration of the droplets' water/air and solid/air interfaces, which also demonstrates that the same number of Apoferritin monomers distribute differently depending on the droplet volume. For instance, when the concentration is high and the surface to volume ratio is also high, a fraction of the proteins would attempt to self-assemble at the interfaces, but the remaining proteins will either form clusters in the bulk or contribute to the first layer by forming a second layer. However, if the number of proteins is relatively low in comparison to the volume of the droplet, this will allow the proteins more freedom to diffuse throughout the droplet. Furthermore, because proteins have a higher affinity to adsorb to surfaces, significant adsorption will still take place, which will result in a lower amount of excess protein remaining in the bulk volume.

On the other hand, in larger droplets with greater surface area, a greater proportion of monomers will likely have a higher probability of self-assembly at interfaces due to the larger surface area available and the tendency of proteins to adsorb at interfaces, resulting in a lower probability of cluster activity in the bulk volume as shown in figure (3-11). Furthermore, it is essential to highlight that self-assembly of proteins may occur at either or both droplet interfaces, water/air and water/solid, simultaneously; however, further research is required to estimate the rate of protein adsorption at each interface. Because the surface area of 8µl droplets at water/solid contact is twice that of 1µl and tripled for 27µl, the same factors apply to the water/air interface. Although the freezing rate data to some extend coincides with these factors, the temperature gradient inside the droplets, particularly for bigger droplets, may significantly impact the freezing rate, as will be explored in depth in Chapter 4.

3.3.5. Parameters of Classical Nucleation Theory (CNT)

Isothermal freezing measurements of monomers, dimers, and clusters have shown that the formation of ice nuclei by these biomolecules is a stochastic process. To determine the CNT parameters, the mean freezing rates previously obtained from experiments at different supercooling temperatures and concentrations were normalised by the number of proteins in a droplet. The nucleation rate as a function of temperature was then determined by fitting the normalised data to the following equation:

$$\mathrm{Log}(J_{het}) = \log(J_0) - \frac{\eta}{T(T-T_m)^2} \qquad (3-5)$$

where $\log(J_0)$ is the logarithm of the kinetic prefactor, T_m is the melting temperature, T is the temperature and η is a constant that contributes to the free energy barrier for ice nucleation. By evaluating η and J_0, the shape factor ($f(\theta) = \eta/\eta_{hom}$) can also be calculated giving that the homogenous η_{hom} equals $1.35 \times 10^7\ K^3$, which is calculated by:

$$\eta_{hom} = \frac{16\pi\gamma_{iw}^3\, T_m^2}{3k_B\, H_m^2} \qquad (3-6)$$

where k_B is Boltzmann constant, γ_{iw} is surface free energy between ice and water (0.025 J/m^2) and H_m is the heat of fusion of water (334 x10^6 J/m^3). As discussed in Chapter 1, the shape factor ranges from 0 to1, and determines the percentage decrease in the homogeneous free energy barrier.

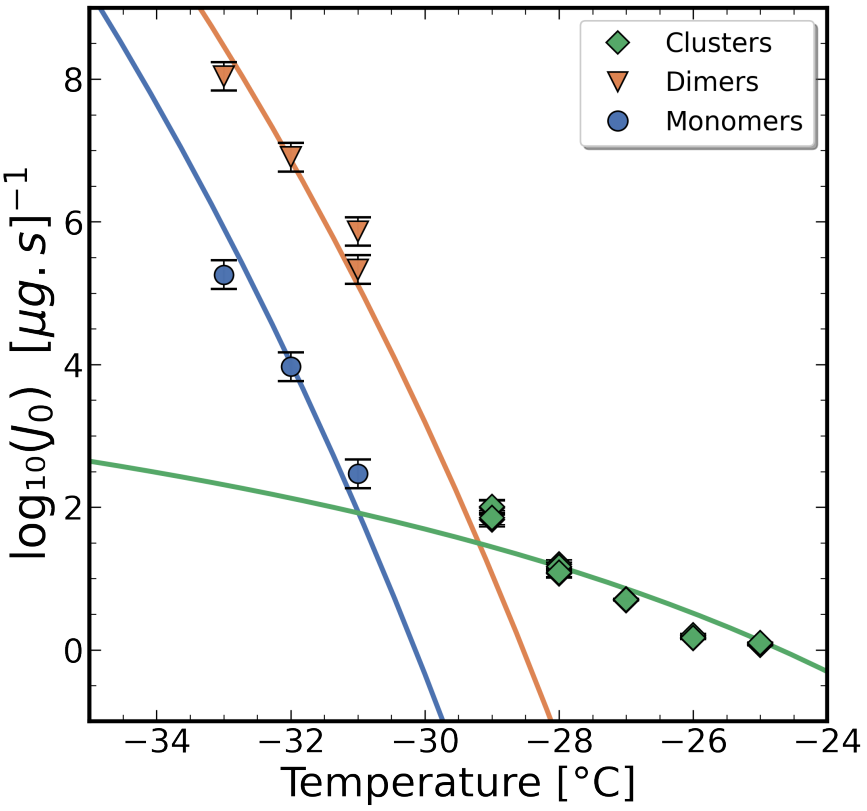

Figure 3-12: Ice nucleation rates derived from isothermal measurements of clusters, dimers and monomers of Apoferritin are presented as nucleation events per protein per unit time as a function of temperature. The data were fitted to CNT equation (3-5).

The nucleation rate as a function of temperature for Apoferritin clusters, dimers and monomers is shown in figure (3-12). All the linear log ($\frac{N_{liq}}{N_{tot}}$) plots that were considered for the figure are provided in Appendix A. The freezing rates at temperatures ranging from –25 to –29 ºC where dimers and monomers gave nearly the same values were regarded to be the freezing rates of clusters (shown in green) and where dimers and monomers gave different values, these are shown in orange and blue. The freezing rates of dimers in figure (3-12) were obtained by subtracting the experimental freezing rates of monomers. Moreover, the fitting lines in figure (3-12) have different gradients which is evidence that they are associated with different INP populations, clusters, dimers and monomers. The CNT fit to each set of points has only two free parameters, J_0 and η. The CNT parameters obtained from the fitting are summarized in table 3-3.

Table 3-3: The calculated parameters from classical nucleation theory. η [K^3] a constant that contributes to the free energy barrier, J_0 [(μg.s)$^{-1}$] the kinetic prefactor, $f(\theta)$ the shape factor.

Apoferritin component	$\boldsymbol{\eta}$ $[\boldsymbol{K^3}]$	$\boldsymbol{J_0}$ $[(\boldsymbol{\mu g}.\boldsymbol{s})^{-\mathbf{1}}]$	$\boldsymbol{f(\theta)}$
Monomer	$8.39 \pm 0.07 \times 10^6$	$10^{38 \pm 0.23}$	0.62 ± 0.005
Dimer	$6.95 \pm 0.04 \times 10^6$	$10^{35 \pm 0.16}$	0.52 ± 0.003
Cluster	$8.33 \pm 0.03 \times 10^5$	$10^{5.5 \pm 0.02}$	0.06 ± 0.0001

Apoferritin clusters were the most effective ice nucleating agents at higher temperatures due to their shape, complexity and size [158]. Their η, is $8.33 \times 10^5\ K^3$, while for the dimer, the simplest aggregate form of Apoferritin is $6.95 \times 10^6\ K^3$. Finally, the monomer is the least effective ice nucleator because it is the simplest Apoferritin form and η is $8.39 \times 10^6\ K^3$. The shape factor values show that the contact angle between the critical ice nucleus and the protein surface is greatest for monomers and smallest for clusters. J_0 values suggest that the number of ice nucleation events by the monomer is $10^{38}\ (\mu g.s)^{-1}$ while for the dimer it is $10^{35}(\mu g.s)^{-1}$ and for clusters has the fewest $10^{5.5}\ (\mu g.s)^{-1}$. The many orders magnitude difference between J_0 for the clusters and for the dimers or monomers is mainly due to there being so few clusters.

The obtained CNT parameters are strongly consistent with the previous hypothesis that the freezing, particularly at higher temperatures, is dominated by a small number of highly efficient INPs (clusters), whereas at lower temperatures a large number of less efficient INPs (dimers or monomers) start dominating the freezing. In another word, clusters are a rarer species than dimers and monomers which are the abundant form of Apoferritin. It is evident that the difference between the monomer and the dimer could be resolved from isothermal measurements, as opposed to the constant cooling rate method, which increased measurement uncertainty and made it difficult to resolve these parameters; monomers and dimers will give nearly identical values.

Furthermore, the derived CNT parameters for Apoferritin subforms, clusters, dimers, and monomers imply that there are properties associated with the protein such as size and topography that determine the ice nucleation efficiency. For example, one reason that could explain the high efficiency of Apoferritin clusters compared to its lower subforms can be attributed to their larger size. The larger size of the INP could result in a higher likelihood of ice nucleation by the particle, due to the greater surface area exposed to water. Also, a common characteristic of INP clusters or aggregates is the intricate shape complexity that emerges from the arrangement and packing of particles. C. Marcolli et al. have established a framework to investigate the governing properties behind the efficiency of soot aggregates in ice nucleation [112]. Ice nucleation on the surfaces of soot aggregates occurs through pore condensation followed by freezing. Capillary condensation mechanisms lead to the uptake of water by pores and cavities, creating confined water within these nanofeatures of the surface. The size and shape of these pores critically influence the efficiency of aggregate INPs. Moreover, the interaction between the particle and water, as determined by the contact angle, is an important factor related to the surface chemistry of the INP [159]. In the same study by C. Marcolli, two types of pores were studied: triangular pores (formed between three overlapped spherical particles) and square pores (formed between four overlapped spherical particles), which are common types of pores in tetrahedral and cubic packing arrangements. One crucial observation suggested that an efficient pore should have a balance between being compact enough to confine water and spacious enough to facilitate the formation of an ice nucleus. Additionally, the size of the pore depends on the diameter of the primary particle. High surface wettability, as indicated by a small contact angle, is an important parameter as it enables water to access small, narrow, and confined spaces such as pores and cavities. In the context of pores formed between curved surfaces, the ice initiation point occurs at the junction which is the narrowest part of the pore where curvatures meet, also known as the neck. Therefore, regions such as necks and joints can be regarded as active sites for nucleation. The study found that the ice growth of the soot triangular ring pore was limited, whereas the square ring pore was limited by capillary condensation. However, when the surface hydrophobicity of the soot aggregates increased, these limitations were minimized.

Apoferritin clusters and oligomers contain nanosized pores and voids due to monomeric overlap. This overlap gives rise to necks and junctions, serving as sites where ice nucleation commences. Thus, ice nucleation likely initiates at the narrowest points of these regions either at the exposed necks and joints where free water is present or within the confined water trapped

inside the pores and voids. This implies that the pores and voids of Apoferritin meet the requirements of achieving an optimal balance in size, facilitating both water confinement and ice nucleus accommodation, along with the contact angle between the surface and water. Also, the number of voids and junctions that the Apoferritin cluster/aggregate has contributes to its ice nucleation efficiency. These distinctive characteristics of Apoferritin clusters/aggregates may play a role in reducing the energy barrier.

Apoferritin dimers consist of a single junction between two monomeric cages. This nanosized junction confines water thus triggers freezing in those regions. This junction has been referred to a conical pore in certain studies [160,161], where ice formation initiates at the narrowest point and results in an ice ring forming between the two cages [112]. However, the critical ice ring's dimensions are influenced by the primary particle's diameter, the contact angle governing surface wettability, and notably, the angle of the formed pore that dictates the conical pore's diameter. Investigating the impact of these parameters on the immersion freezing ice nucleation efficiency of a simple structure like Apoferritin dimers could yield interesting insights. Nevertheless, this junction or conical pore serves as an active site for dimers, enhancing their performance as INPs compared to single monomeric cages lacking pores or cavities.

Single Apoferritin monomers were found to be the least efficient subform of Apoferritin. This suggests that spherical or curved INPs are less efficient than porous or complex INPs. The efficiency of curved surfaces is highly dependent on the particle's diameter and the surface chemistry, which is determined by the contact angle with the critical ice nucleus. This relationship is described in Chapter 1 using Fletcher’s shape factor equation (1-20). Hence, spherical or curved surfaces of nanoscale size are likely to be inefficient ice-nucleating particles. Considering that Apoferritin is the predominant subform and its freezing efficiency exhibits weak dependence on specific surface features for water confinement, as evident in clusters and dimers, it offers a valuable model for investigating the influence of modifications in particle surface chemistry on ice nucleation efficiency and contact angle in immersion freezing mode, without external interference from other surface attributes in the outcomes.

3.4. Conclusion

In contrast to the constant cooling rate approach, isothermal measurements have been shown to be an efficient and direct way for determining the ice nucleation rate of Apoferritin subcomponents. We have shown that at higher temperatures, the rate of freezing by monomers and dimers is essentially the same, and this is attributed to the presence of rare protein clusters that dominate the freezing, resulting in a nonlinear curve. At lower temperatures, monomers and dimers start dominating the freezing with distinct freezing rates, resulting in a linear curve. In addition, the freezing rate is proportional to the concentrations of monomers and dimers. Moreover, the same number of monomers in various droplet volumes yields a varied freezing rate. However, the non-uniform temperature inside the larger droplets could also be responsible for the observed slow freezing rate as will be discussed in depth in Chapter 4. We also obtained plausible classical nucleation theory parameters that indicated that Apoferritin clusters are rare INPs yet effective enough to dominate freezing at higher temperatures, whereas dimers were found to be more efficient than monomers.

4. SIMULATION OF DROPLET'S INNER TEMPERATURE

4.1. Introduction

The vast majority of ice nucleation measurements centre on the characteristics and efficiency of the nucleating agent. When evaluating the freezing rate of water droplets, the thermal properties of water droplets are rarely addressed and are often largely neglected. Nevertheless, there have been a number of studies on the effect of solid surface wettability on the freezing time of water droplets and the time needed for an ice front to evolve and freeze completely [162–164]. The effect of droplet volume and solid substrate wettability on the inner temperature of droplets and its correlation with their freezing rate has not been investigated in ice nucleation experiments. This gap exists because most experiments use slow cooling rates, which is not necessarily appropriate for isothermal measurements. Furthermore, the effects of volume and surface wettability may not be observable in experiments conducted with slow cooling rates. Here, we apply a finite element model to understand the significance of the non-uniform temperature gradient inside static water droplets of different volume and contact angle, as well as to predict the delay time for achieving a uniform inner temperature. The results will be used to interpret unfrozen fraction data for Apoferritin monomers, water, and buffer using an isothermal freezing approach. Later, the impact of other experimental factors such as oil and non-ionic surfactant on the freezing rate will be demonstrated.

4.2. Sample Preparation and Methods

The methods and sample preparation are described in Chapter 3. Figure (4-1) depicts a configuration of droplet arrays as utilised in the experiment.

4.2.1. Hydrophobic Coating of Silicon Substrates

Silicon substrates used for droplet assays were sprayed with commercial hydrophobic spray (Crep Protect - Rain & Stain Waterproof Protector Nano Protection), and treated in an oven at 90 – 120 ^{o}C for an hour.

4.2.2. Droplets Detection

The unfrozen droplets were detected using YOLOv5 algorithm via the Pytorch framework. The object detection algorithm YOLO, which stands for "You Only Look Once," splits images into multiple small grids or cells and the detection of an object proceeds in each individual cell [165,166]. Glenn Jocher published the algorithm in 2020, and it is open-source code that is available on GitHub here: https://github.com/ultralytics/yolov5. The algorithm was trained on 100s of images of droplets to recognise the unfrozen ones, including droplets in the image's corners as shown in figure (4-1) and the labels give the confidence (with a confidence level of ≥ 0.90) that a droplet is unfrozen.

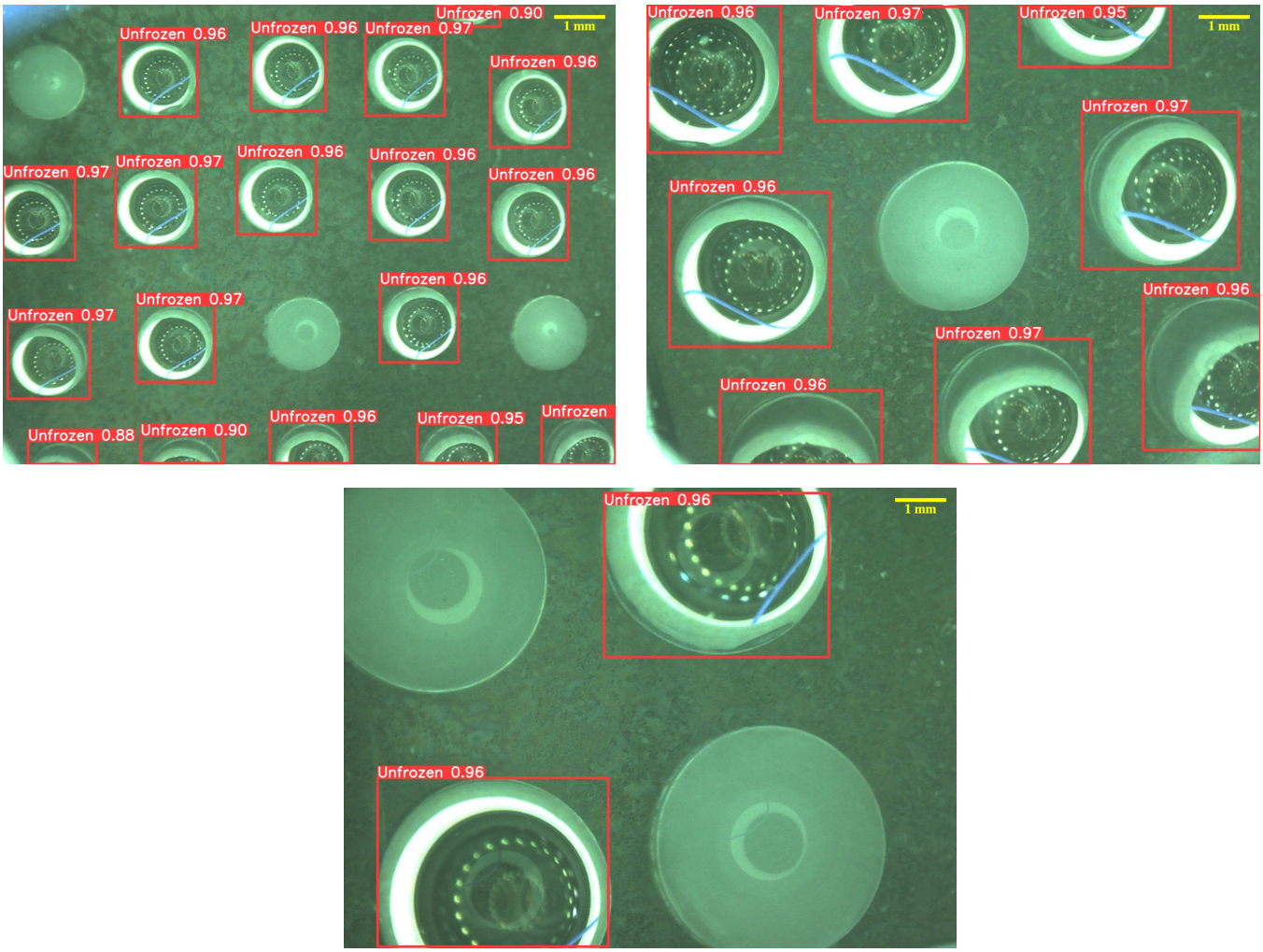

Figure 4-1: Images of droplet arrays with volumes of 1, 8, and 27 µl on silicon substrates given a hydrophobic coating. The background that the coated silicon substrate displays appears to be a condensation of droplets, but it is only the texture of the hydrophobic coating; the circular pattern seen on the unfrozen droplets is the reflection of the lighting system.

4.3. Results and Discussion

4.3.1. Freezing Rate Increasing with Time

So far, the time-dependent freezing rates of droplets addressed in Chapter 3 were mostly associated with the characteristics and distribution of nucleating agents, such as Apoferritin proteins. As was covered in the preceding Chapter, a plot of the logarithm of the unfrozen fraction associated with a nucleating agent in an isothermal experiment is generally either a straight line or a smooth curve with decreasing gradient. However, these are not the only two profiles observed in time-dependent measurements; a third case has occasionally been observed where the freezing rate seemed to rise with time [145]. Different volume droplets (1, 8, and 27 µl) with the same monomer concentration (0.82 mg/ml) can show this behaviour, (figure (4-2)), as can water droplets of 8µl with no deliberate addition of nucleating agents (figure (4-3)). For some materials, such as alkanes this has been attributed to surface crystallisation [2].

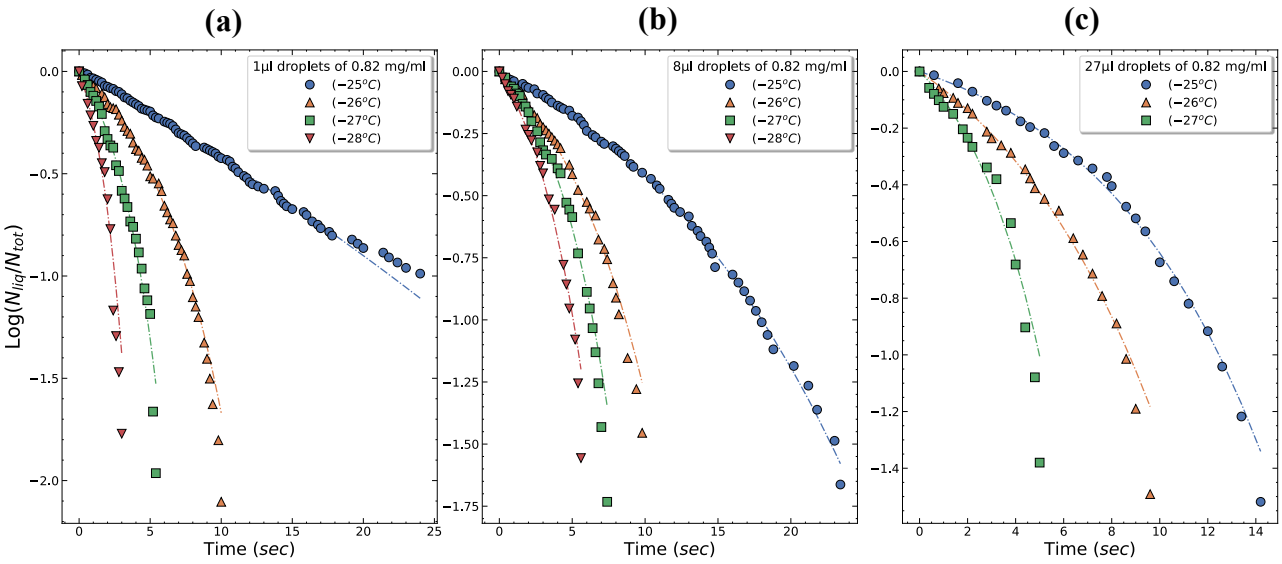

Figure 4-2: Log of unfrozen fraction of different volume droplets (1, 8, 27 µl) with the same concentration of Apoferritin monomer (0.82 mg/ml) measured as a function of time at different cooling temperatures. The droplets were deposited on substrates given a hydrophobic coating. Note that in all but one case the gradient (freezing rate) increases with time. Equation (4-1) was used to fit the curves in (a, b, c).

However, the explanation of such curves observed here for protein solutions and water, could be different, especially given the fact that their unfrozen fraction data had previously been seen to show a constant or decreasing gradient.

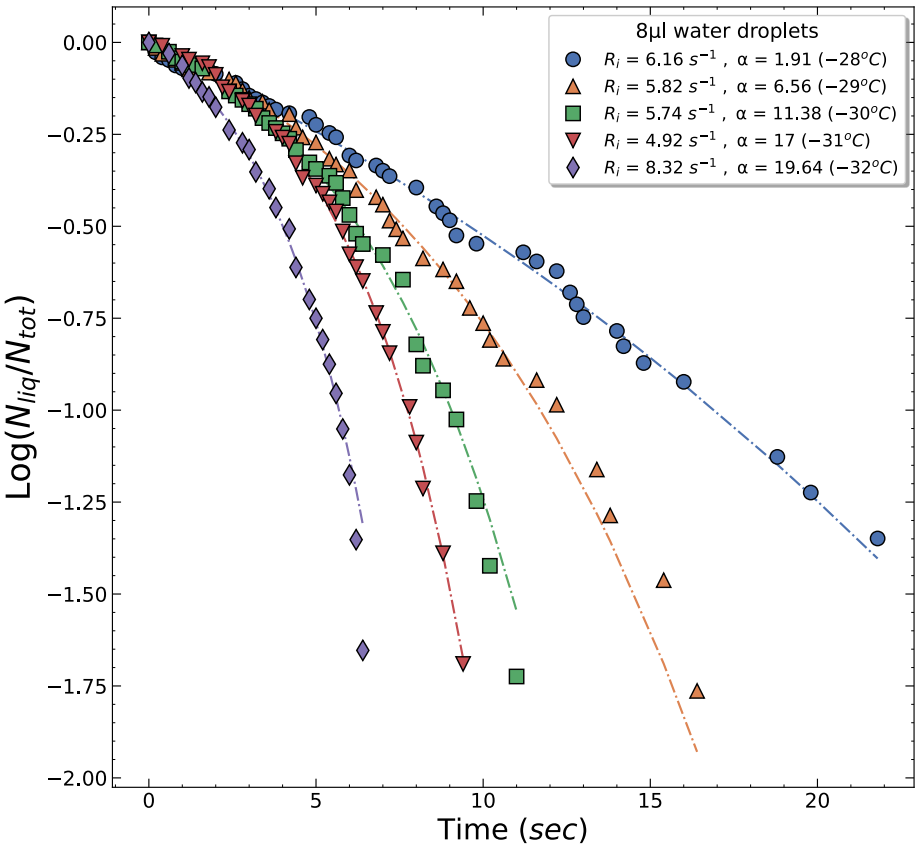

Figure 4-3: Data for 8 µl water droplets on a hydrophobic surface show that the gradient of the log of the unfrozen fraction (freezing rate) increases with time as also observed for Apoferritin monomer solutions (figure 4-2). Initial freezing rate R_i and α were determined by fitting the curves to equation (4-1).

The curves were fit using the Gompertz equation [145]:

$$\frac{N_{liq}}{N_{tot}} = \exp\left(\left[\frac{R_i}{\alpha}\right][1 - \exp(\alpha\, t)]\right) \qquad (4-1)$$

where R_i is the initial freezing rate and α is an indicator that quantifies whether the freezing rate increases or decreases over time. If $\alpha > 0$, R_i increases with time, whereas if $\alpha < 0$, R_i decreases with time, and in this case, R_i and α can be determined using the fitting methods discussed previously in Chapter 3. R_i and α were calculated for water and monomer solutions using equation (4-1), and their results are shown in figure (4-3) and (4-4). The rates of freezing increase systematically with decreasing temperature as do the α values.

Although equation (4-1) is mathematically useful in quantifying and describing this type of unfrozen fraction curve, it does not explain the physical reason for the increasing freezing rate,

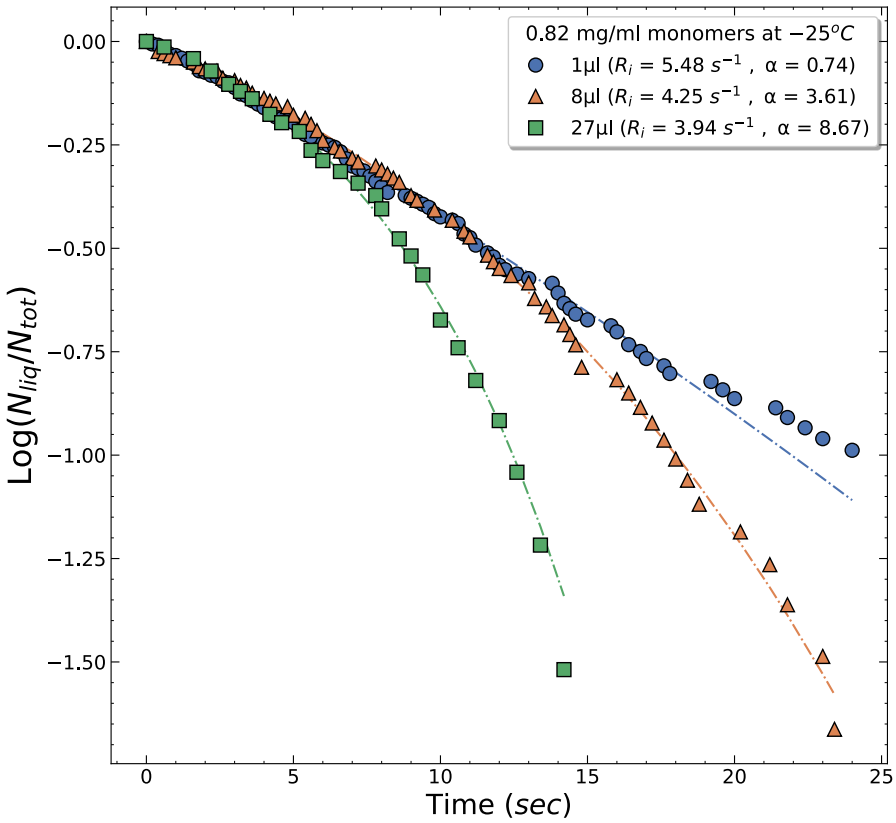

Figure 4-4: Unfrozen fraction data for 1,8 and 27 µl droplets of 0.82 mg/ml monomers at −25 °C. The data are a subset of those shown in figure 4-2. Initial freezing rate R_i and α were determined by fitting the curves to equation (4-1). It is immediately apparent that the freezing rate of 27 µl droplets increases with time more than that of 1µl and 8µl droplets. Indeed, the data for 1µl show a nearly constant freezing rate.

particularly whether it is related to the nucleation mechanism or another factor such as the droplet volume. The only difference between these experiments and those in Chapter 3 is that the hydrophobicity of the substrates was increased, resulting in a greater contact angle between the droplets and the substrate. In light of the fact that Apoferritin monomers have previously shown a constant or decreasing freezing rate, the increasing freezing rates seen here are probably not attributable to the ice nucleating agent, but rather to the droplet size and its contact angle with the substrate. The droplet volume and contact angle influence the temperature distribution inside the droplet while it cools, which in turn could affect the apparent freezing rate. To establish whether this is a likely explanation, the temperature profile inside the droplet volume should be simulated by heat transfer modelling, which was done using the finite element method described in the next section.

4.3.2. Modelling the Temperature Distribution Inside a Cooled Water Droplet

In experimental studies of ice nucleation, particularly immersion freezing experiments, the rate at which droplets freeze is generally explained by the nucleating agent's ability to nucleate ice. Although this is usually correct, there are situations in which it is important to consider the physics of heat transfer in cooled droplets, as shown previously in figure (4-2) and (4-3).

Cooling a droplet from a high temperature, such as room temperature, to a low temperature below the melting point of water may lead to a non-uniform interior temperature because of how heat is removed. Factors such as the volume, contact angle between droplet and substrate and the cooling rate determine the time needed to achieve a homogeneous temperature across the droplet. Until this time is reached, some regions inside the droplet may be colder or warmer than others, which may cause a variation in the local nucleation rate and therefore also in the mean nucleation rate that determines the freezing rate of the droplets.

Figure (4-5) illustrates a model example of the temperature distribution inside a droplet; the temperature is non-uniform at this low temperature; a sufficient delay time is required to achieve a uniform temperature throughout the droplet. Understanding how the size of the droplet, the wettability of the solid surface in contact with it and the cooling rate affect the inner temperature is crucial also to exclude the possibility that non-uniform temperatures affect the measured immersion freezing rates. A simple simulation of the heat balance inside a droplet of given volume and contact angle will be used in the next section to further investigate the temperature distribution inside a droplet.

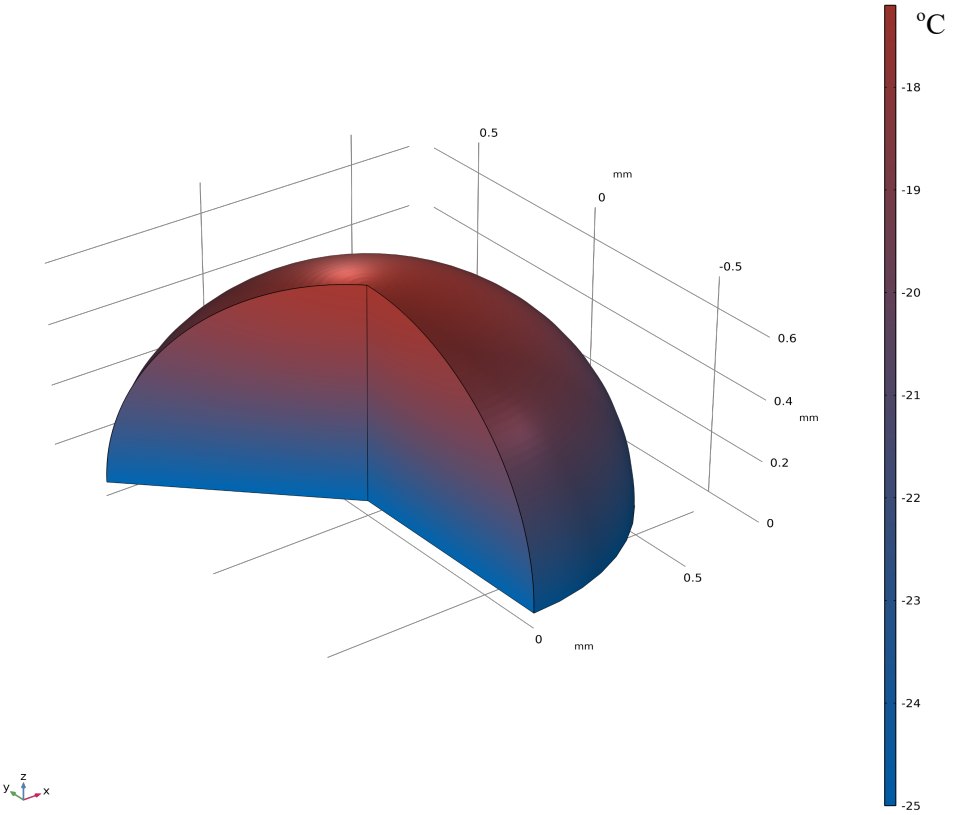

Figure 4-5: Modelling of temperature lag inside a water droplet at –25 °C and *t* = 1.5 sec. The calculation demonstrates that the temperature is not uniform across the whole droplet volume, since the lower region (dark blue) is colder than the upper region (red). The scale bar on the right indicates the temperature values inside the droplet, whilst the cartesian axes display the droplet's size in three dimensions.

i) Simulation of Static Water Droplet

COMSOL Multiphysics software was used to simulate the cooling of a static water droplet of various sizes and contact angles. Water is known to be an isotropic fluid whose physical and thermal characteristics stay constant in all three cartesian coordinates. Here, we perform the simulation using a spherical cap water droplet shape. For cooling, the heat transfer boundary conditions were determined by setting the bottom of the droplet to the programmed substrate temperature. In addition, it was presumed that the water/air interface was thermally insulating since air is a poor heat conductor. Internal convection inside the droplet was ignored as the thermal capillary flow in a cooled droplet is weak because the direction of the temperature gradient goes against buoyancy and the viscosity increases [162]. The profile of the temperature field inside a water droplet was obtained by solving the heat conduction equation as a function of time using the finite element method on the COMSOL-heat transfer platform. The heat equation formula is:

$$\frac{\partial}{\partial x}\left(k_\omega \frac{\partial T}{\partial x}\right) + \frac{\partial}{\partial y}\left(k_\omega \frac{\partial T}{\partial y}\right) + \frac{\partial}{\partial z}\left(k_\omega \frac{\partial T}{\partial z}\right) = \rho_\omega c_p \frac{\partial T}{\partial t} \qquad (4-2)$$

It can be simplified to:

$$k_\omega \nabla^2 T = \rho_\omega c_p \frac{\partial T}{\partial t} \qquad (4-3)$$

where k_ω is the thermal conductivity of water, ρ_ω the density, c_p the heat capacity at constant pressure and T is the temperature. The fundamental thermal parameters for water were obtained from COMSOL's built-in material's physics properties. Table 4-1 highlights the key water properties used in the simulation. The droplet was cooled from ambient temperature $\mathrm{T_0} = 18\ ^{\circ}\mathrm{C}$ at $t_0 = 0$ and kept for 60 seconds at three different supercooling temperatures ($-25,\ -30,\ -38\ ^{\circ}\mathrm{C}$).

Table 4-1: Key parameters used in modelling the inner temperature profile of static water droplet.

Variable	Value	Water property
ρ_ω	$997\ \mathrm{kg/m^3}$	Density
c_p	$4179\ \mathrm{J/(kg.K)}$	Heat capacity at constant pressure
k_ω	$0.613\ \mathrm{W/(m.K)}$	Thermal conductivity
l_ω	$333.5\ \mathrm{kJ/K}$	Latent heat
T_0	$18\ ^{\circ}\mathrm{C}$	Ambient temperature
T_m	$0\ ^{\circ}\mathrm{C}$	Melting temperature
T_h	$-25,\ -30,\ -38\ ^{\circ}\mathrm{C}$	Programmed temperatures

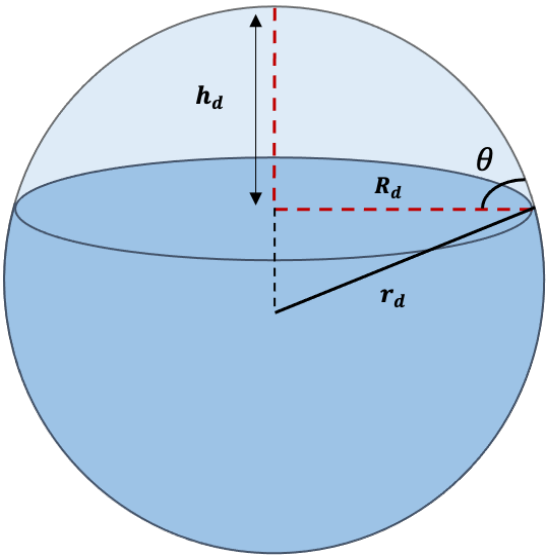

Figure 4-6: A diagram demonstrating the fundamental simulation parameters that govern the water droplet's geometrical shape. Equations (4-4) and (4-5) employ and define these parameters.

For each 0.1 second time step, the droplet's internal temperature was solved and recorded. The simulation was carried out using three different droplet volumes, 1, 8, and 27 µl. When it comes to modelling a static water droplet, the most basic geometrical shape that can be used is a simple spherical cap shape having the geometry shown in figure (4-6) and described by the following parameters [163]:

$$r_d = \frac{R_d}{\sin\theta} \qquad (4-4)$$

$$h_d = \frac{R_d(1-\cos\theta)}{\sin\theta} \qquad (4-5)$$

where r_d is the spherical cap's radius of curvature, R_d is the radius of the water/solid contact area, h_d is the hight of the spherical cap and θ is the contact angle (CA) which depends on the wettability of the solid surface.

ii) Volume and Contact Angle's Effects on a Droplet's Internal Temperature

To understand the impact of the contact angle (CA) on the shape of a droplet deposited on a solid surface, we can plot the droplet height (h_d) using equation (4-5) against different droplet radii (R_d). This allows us to observe the relationship between the contact angle and the droplet's shape (see figure 4-7). The height of the droplet, h_d, is proportional to CA, provided that if the wettability is high, the volume fraction in contact with the solid surface will decrease. This should be the case for all droplet sizes, since the wettability of the surface in contact with the droplet is distinctive of that surface. Moreover, the ratio ($h_d/2R_d$) increases as wettability decreases. In the majority of ice nucleation experiments of immersion freezing, the droplets are deposited on a solid substrate with a certain wettability.

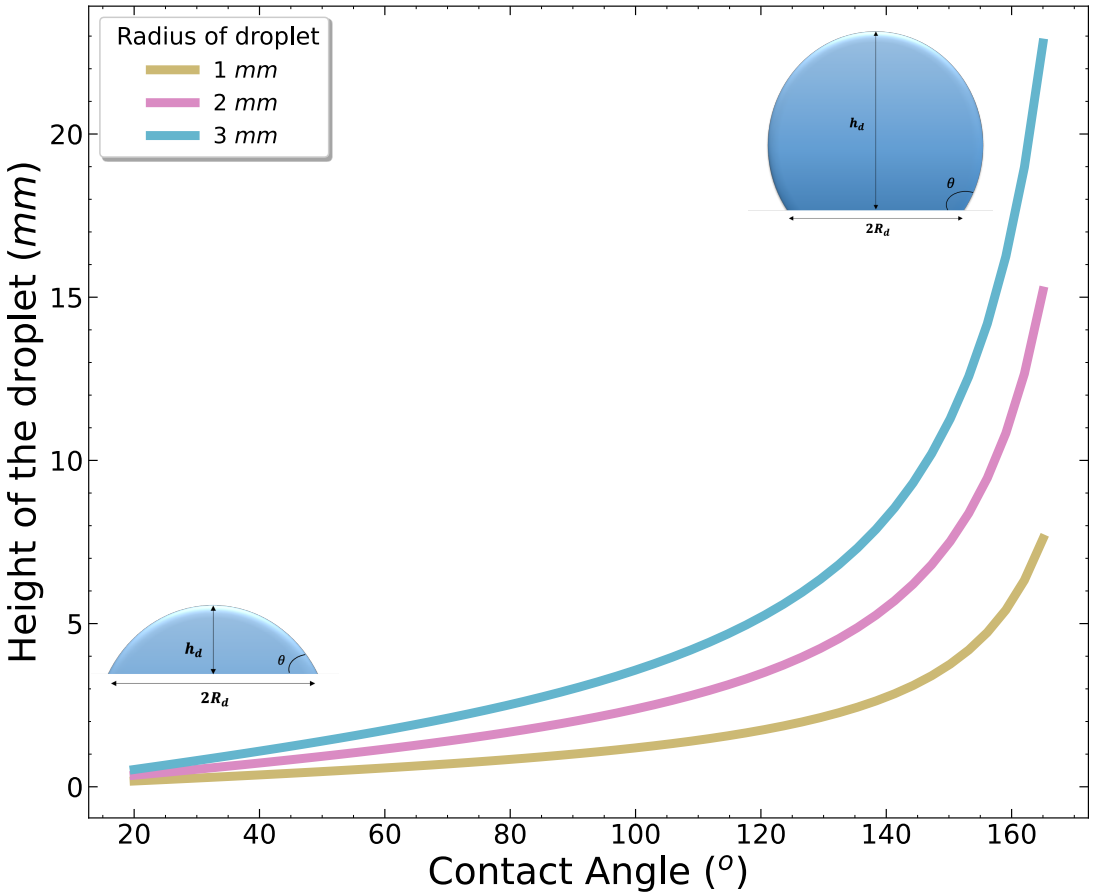

Figure 4-7: The relationship between a solid surface's wettability and the height of a droplet's spherical cap for three different radii. When the wettability is decreased, the contact angle of the droplet and its height increase, resulting in the ratio ($h_d/2R_d$) to likewise increase. As a consequence, more cooling time is required for the droplet to attain a uniform inner temperature.

In this case, heat transfer will only take place at the liquid/solid contact area of the droplets. Assuming that water is an isotropic material, if the ratio $(h_d/2R_d)$ is large due to CA, it indicates that for a droplet's whole volume to be at the same temperature, a longer delay time is required than if the ratio $(h_d/2R_d)$ is small, moreover the delay time increases as the droplet's size increases.

Figure (4-8) depicts snapshots of the temperature contour inside water droplets of 1µl size at t = 0.5 second using equation (4-2) in COMSOL for different CAs, see Appendix B for 8 and 27µl droplets. The starting temperature of the droplet was 18 ºC, and the substrate temperature was set directly to the programmed value, in this case –25ºC; thus, the simulation here did not account for the time taken by the substrate to reach this temperature from room temperature, the effect of cooling rate will be discussed in the next section. The temperature contours inside the droplet were different for each CA case, the temperature of the lowest level of the droplet's volume drops to –25 ºC faster than the temperature of the highest level. Since the temperature difference between the lowest and highest level in the droplets greatly depends on the wettability, the difference at 90º CA was in the range of ± 0.5 ºC, whereas at 140º CA the difference has increased to approximately 14 ºC. A comparison of the inner temperature as a function of the delay time taken to acquire a uniform temperature across the droplet volume at –25 ºC is shown in figure (4-9) for three different droplet volumes 1, 8 and 27 µl. The inner temperature profiles depicted in the figure were captured when 90% of the droplet's volume reached a temperature within ± 0.1°C of the programmed temperature. The red dots in figure (4-8) represent specific temperature points that exemplify this criterion.

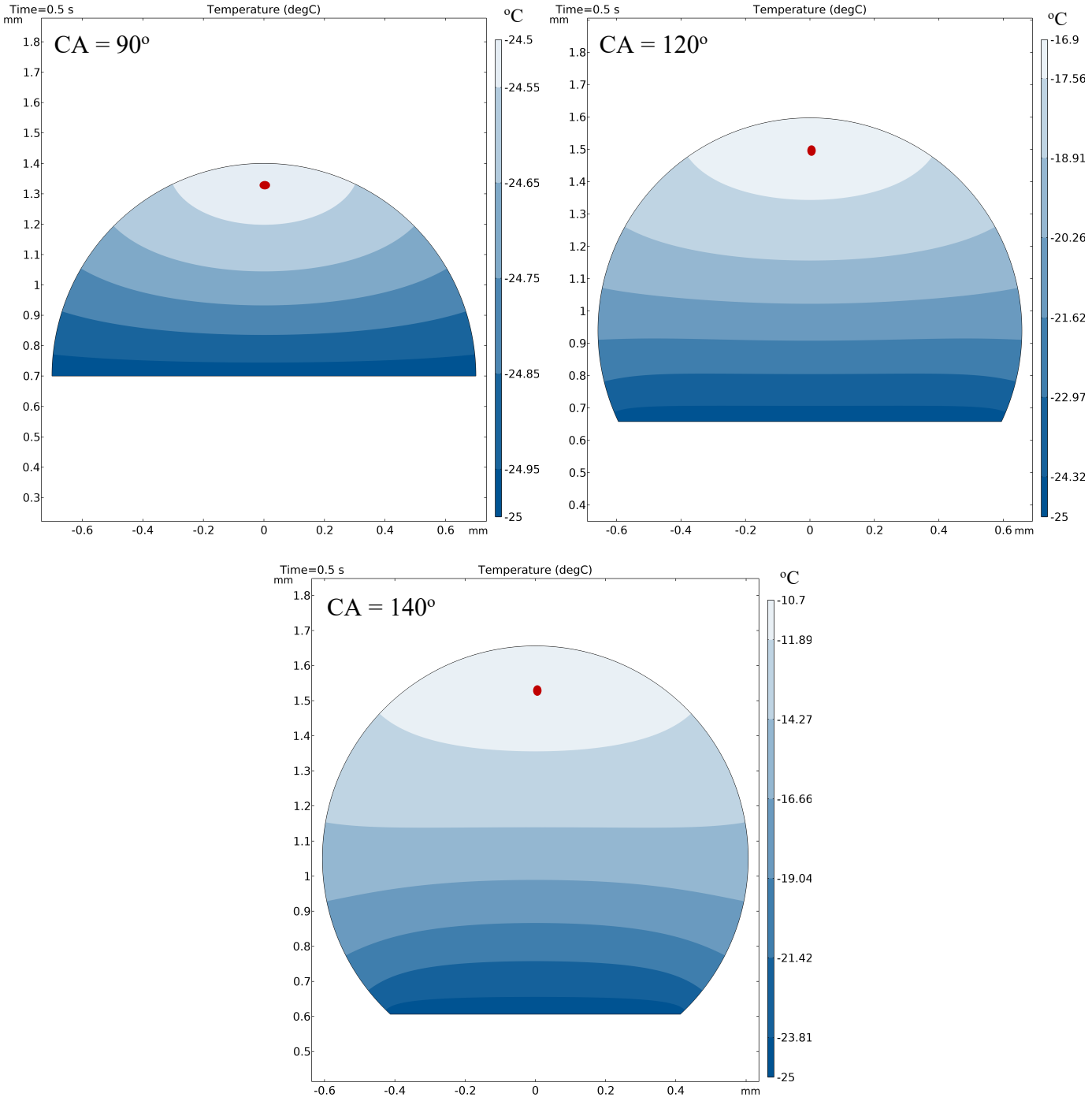

Figure 4-8: Simulation of the temperature profile inside a droplet of 1µl size at a temperature of −25 °C and contact angles of 90, 120, and 140°, respectively. At t = 0.5 seconds, the model predicts that the temperature difference between the lowest and highest levels of the droplet for 90° CA was in the range of ±0.5 °C, but for 120° and 140°, the temperature difference was 8 and 14 °C, respectively. This difference in temperature increases as the droplet's diameter increases for the same time and CA.

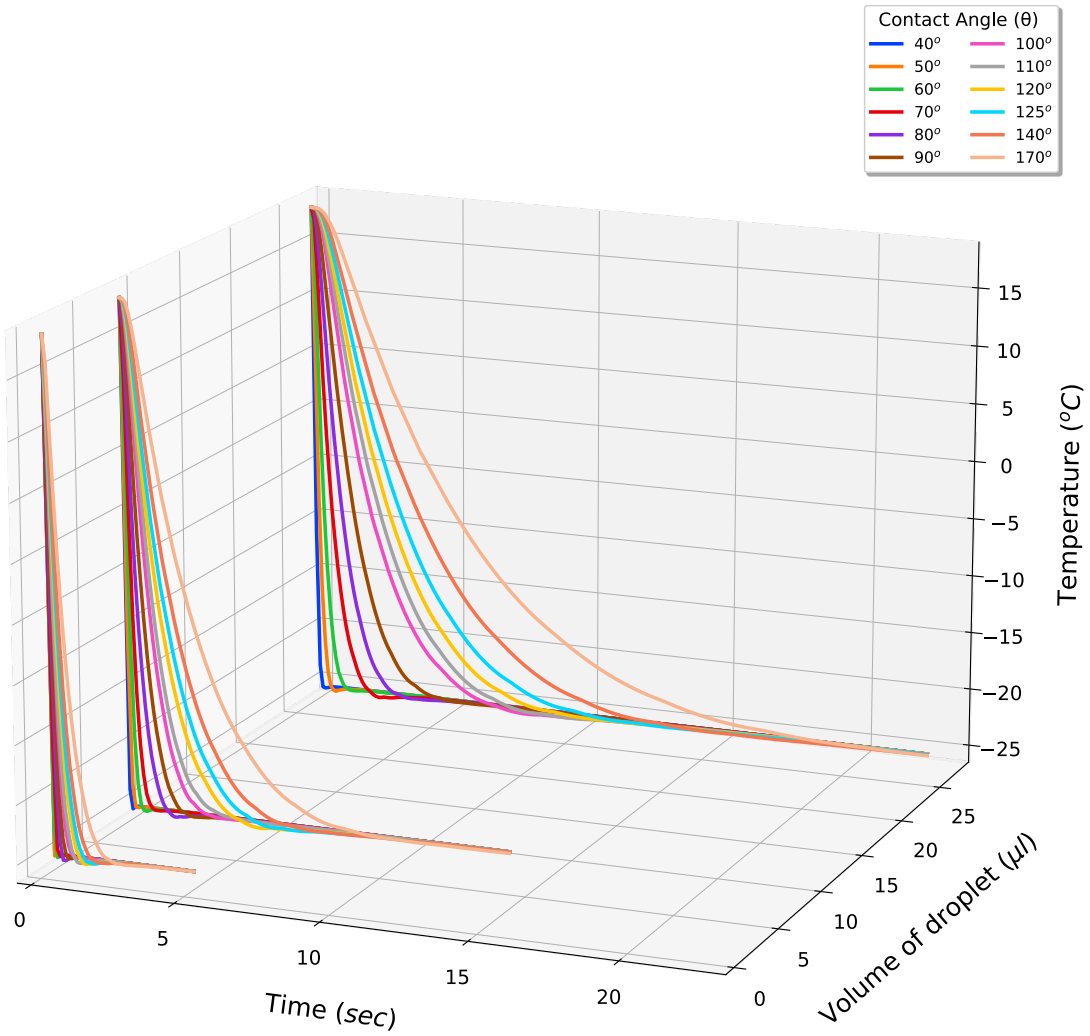

Figure 4-9: The inner temperature profiles as a function of time for 1, 8 and 27 µl droplets at various contact angles are measured at the red dots in figures (4-8), (B-1) and (B-2). It is evident that the delay time to obtain a uniform temperature inside a droplet is significantly dependent on the size of the droplet and the wettability of the solid surface. Smaller droplets approach a uniform interior temperature within ~2 seconds, whereas bigger droplets need ~10 to ~20 seconds. The initial ambient temperature of all droplets is 18 °C, and their substrate temperature is set to −25 °C.

The delay time increases as droplet size and solid surface hydrophobicity increase, and the correlation between these two factors and the delay time can be seen in figure (4-10). This correlation was obtained for three cooling temperatures, and the delay time was taken to be when 90% of the droplet's volume was within ± 0.1°C of the kept temperature.

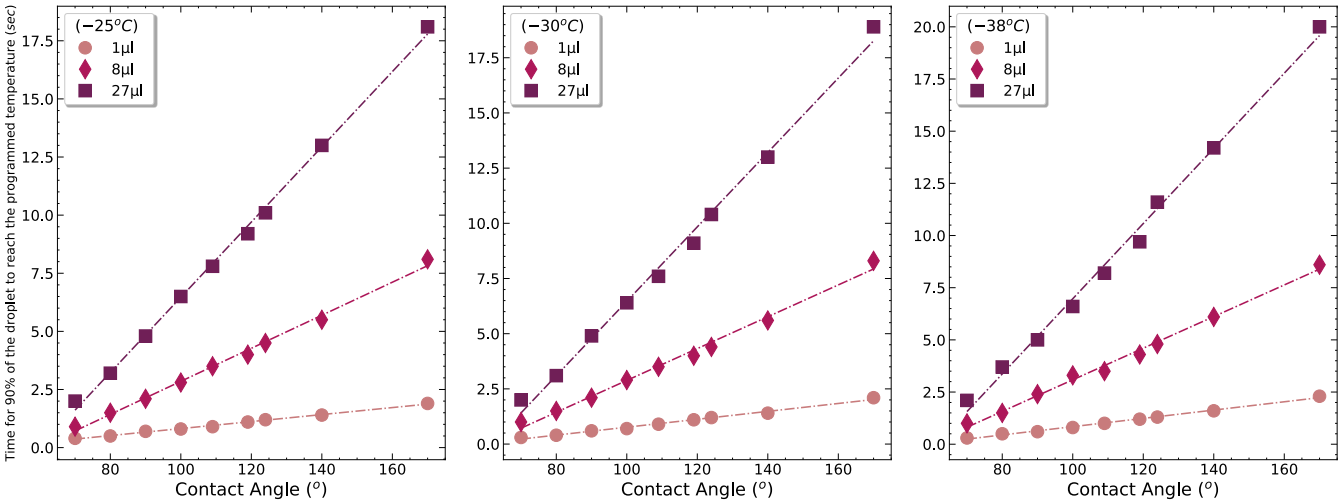

Figure 4-10: The correlation between the uniform temperature delay time and the contact angle for various cooling temperatures. The delay time is linearly proportional to CA when 90% of the droplet volume has a uniform inner temperature.

Table 4-2 provides a summary of the linear equations that resulted from fitting the respective droplet volume data. It can be concluded that for every 1° contact angle, the model predicts that the delay time will increase in proportion to the volume of the droplet. Figure (4-10) clearly illustrates a direct correlation between delay time and CA, linear fittings indicate that the delay time in seconds increases by a factor of 4 when the droplet volume is increased by a factor of 8, and increases by a factor of 10 when the droplet volume is increased by a factor of 27. This result could be used to explain the unfrozen fraction data for Apoferritin monomers and water that were presented in section (4.3.1).

Table 4-2: Straight line equations of the delay time [t] and goodness of fit [R^2] for figure (4-10).

Programmed Temperature	**Volume of the Droplet**		
	1µl	8µl	27µl
–25 °C	$t = 0.015\,\theta - 0.69$ $R^2 = 0.99$	$t = 0.07\,\theta - 4.23$ $R^2 = 0.99$	$t = 0.16\,\theta - 9.6$ $R^2 = 0.99$
–30 °C	$t = 0.018\,\theta - 1.03$ $R^2 = 0.99$	$t = 0.072\,\theta - 4.32$ $R^2 = 0.99$	$t = 0.17\,\theta - 10.37$ $R^2 = 0.99$
–38 °C	$t = 0.019\,\theta - 1.14$ $R^2 = 0.99$	$t = 0.075\,\theta - 4.48$ $R^2 = 0.99$	$t = 0.18\,\theta - 11.11$ $R^2 = 0.99$

iii) Effect of Cooling Rate on the Inner Temperature of a Droplet

We also simulated the effect of the cooling rate on the inner temperature of droplets with varying volumes and CAs. The cooling rate can be given by:

$$Cooling\ rate = \frac{[\,T_0 - T\,]}{\Delta t} \qquad (4-6)$$

where T_0 is the ambient temperature which is 18 °C, T is the programmed temperature and Δt is the set time which is the time it takes to reach the programmed temperature from the ambient temperature.

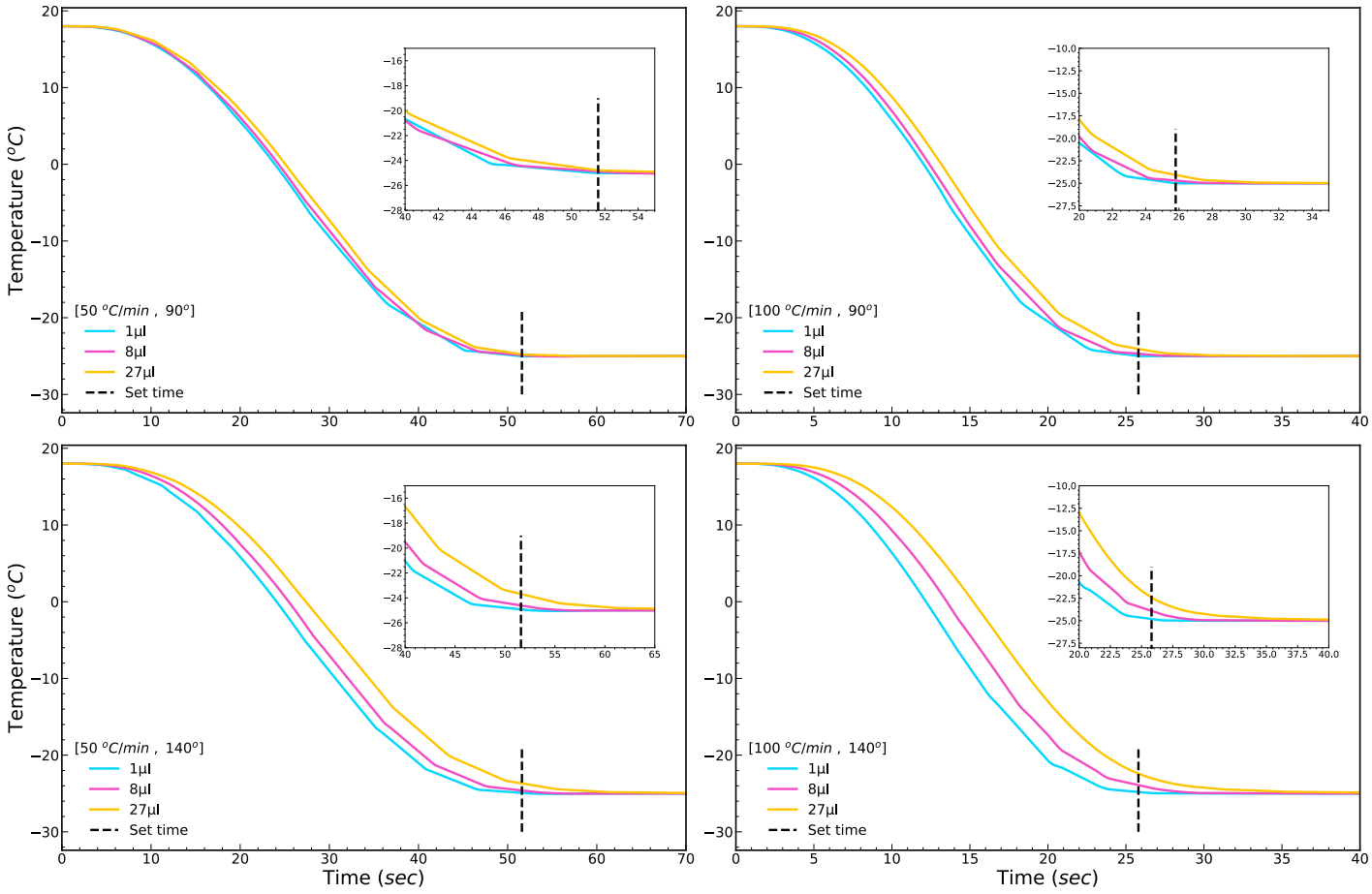

Figure 4-11: The inner temperature of 1, 8, and 27 µl droplets for 90° and 140° CAs at 50 and 100 °C/min cooling rates. The dashed line represents the calculated Δt necessary to reach the programmed temperature of –25 °C. Insets show zoomed views.

Equation (4-6) was used in order to determine the value of Δt that corresponds to a given cooling rate value in the simulation. Figure (4-11) shows examples of the inner temperature gradients inside 1,8, and 27 µl droplets when the programmed temperature was –25 ºC at two different CAs and cooling rates. Figure (4-12) summarizes the time for 90% of the droplet to reach –25 ºC at contact angles of 90º and 140º. The plots show that when using a cooling rate, in general, the time necessary to attain a uniform temperature inside a droplet decreases, especially for low CAs, as compared to no prior cooling in the previous section. When droplets of varying volumes are cooled slowly using a slow cooling rate, they reach a uniform inner temperature at the programmed temperature (–25 °C). However, when a rapid cooling rate is employed, the inner temperature becomes non-uniform at –25 °C, necessitating additional time to reach equilibrium. As a result, small droplets, such as 1µl, mostly reach a uniform inner temperature at different cooling rates and CAs at the set time, as compared to large droplets, such as 27µl, where the inner temperature is significantly influenced by the cooling rate and CAs and is not uniform at the set time, therefore slow cooling rates are preferable for cooling larger droplets. This is consistent with the simulation findings for droplets without prior cooling as discussed in section (ii).

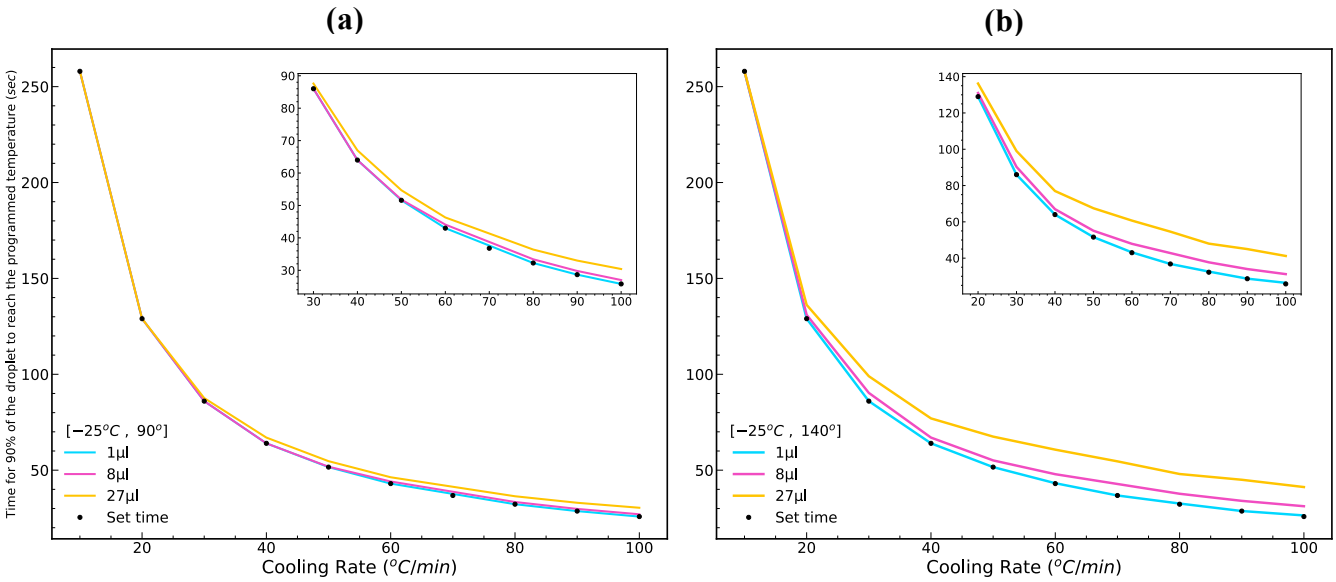

Figure 4-12: The time required for 90% of a droplet to reach the programmed temperature (–25 ºC) as a function of cooling rate for 1, 8, 27 µl droplets at (a) 90º and (b) 140º CAs. Each dot represents the calculated Δt value that corresponds to a given cooling rate. The insets show zoomed-in views.

It is important that the cooling instrument used in the experiments reach the programmed temperature at the corresponding time Δt for a given cooling rate as determined by the equation (4-6), since this affects the accuracy of the data obtained. Figure (4-13) shows the temperature profile of our experimental cooling system (the temperature recorded by the cooling stage thermocouple) at a cooling rate of 50 °C/min to reach −25 °C and an ambient temperature of 18 °C.

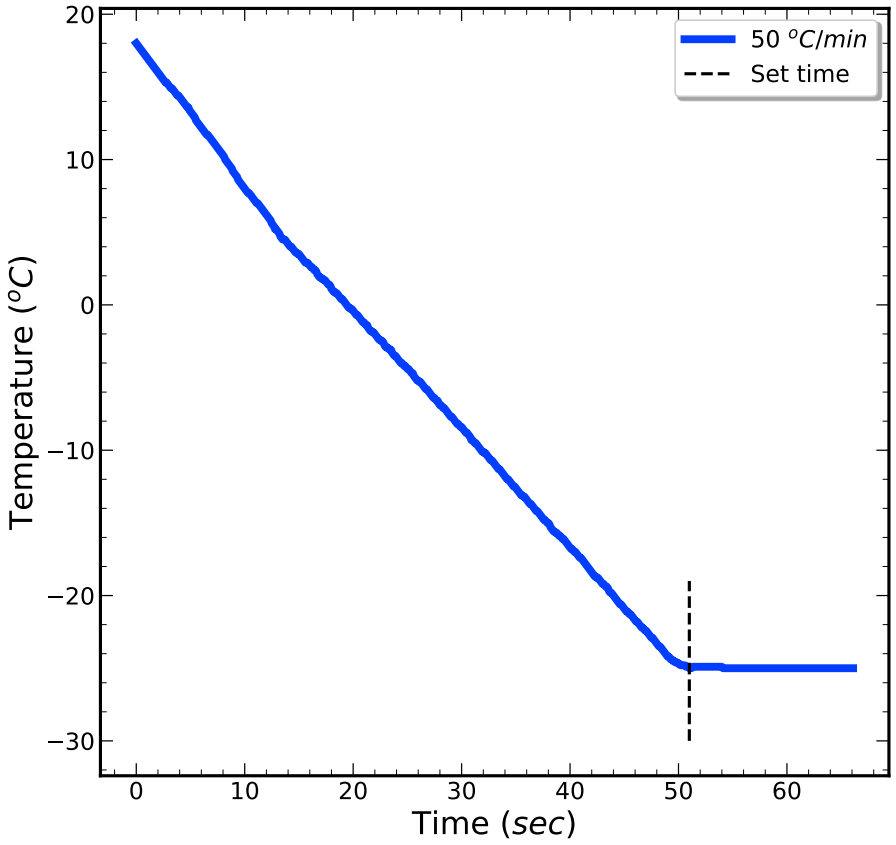

Figure 4-13: Temperature profile of the cooling system used. The cooling rate was 50 °C/min, the ambient temperature was 18 °C and the programmed temperature was −25 °C. The dashed line is the calculated Δt.

iv) Validation of the Simulation Model for the Freezing Rate of Water and Monomers

The previously reported increasing freezing rates of water and monomers with time may be interpreted in light of the simulation findings. Since the 1, 8, 27 µl droplets used in the time-dependent measurements on hydrophobic silicon substrates had contact angles of ≈120° for water and ≈110° for monomers due to proteins also lowering the contact angle on surfaces. The delay time was determined using the appropriate equations from table 4-2 and eliminated from the unfrozen fraction data for water and monomers in figures (4-3) and (4-4). The logarithm of the unfrozen fraction obtained after this correction was fitted to a straight line to estimate the freezing rate, as shown in figures (4-14) for monomers and figure (4-15) for water.

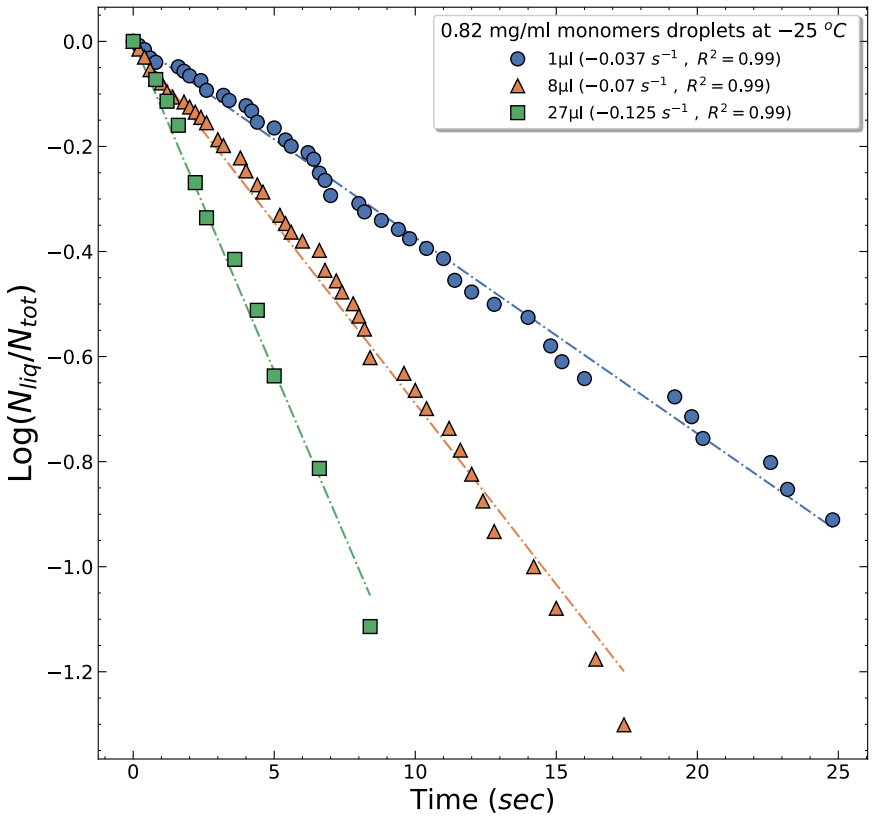

Figure 4-14: Logarithm of the unfrozen fraction data of figure (4-4) for 0.82 mg/ml Apoferritin monomers after eliminating points prior to the delay time needed to obtain near-uniform inner temperature. The data clearly illustrate that the freezing rate of monomers is linear and increases as the volume of droplets increases. Additionally, the slopes and goodness of fit R^2 are determined.

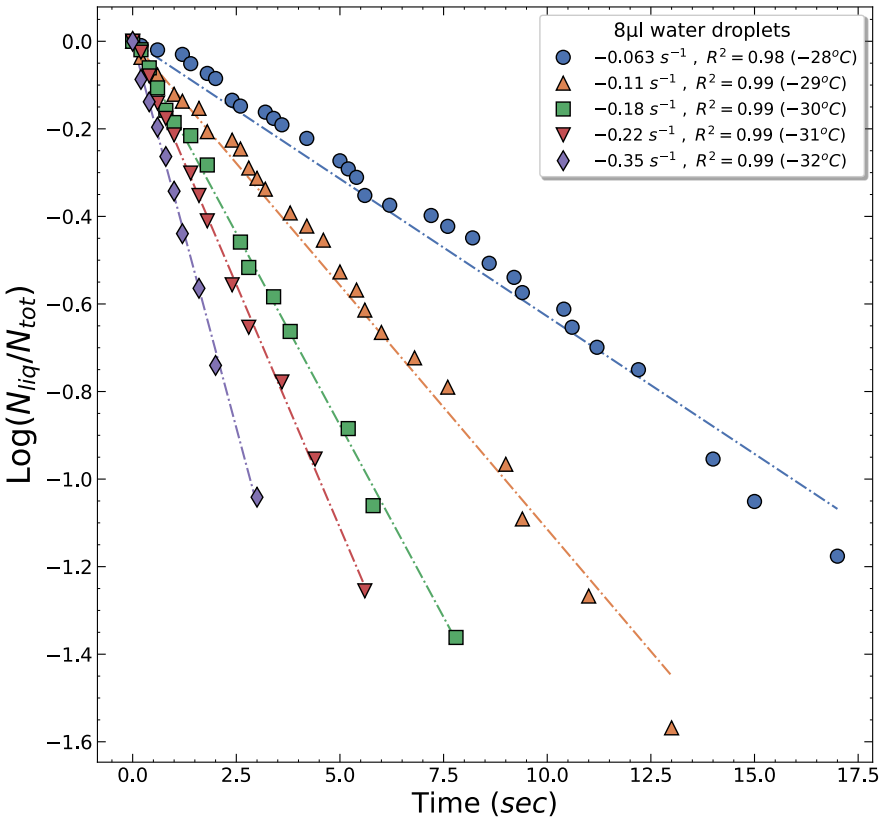

Figure 4-15: Logarithm of unfrozen fraction data of data of figure (4-3) for water after eliminating points prior to the delay time needed to obtain near-uniform inner temperature. The freezing rates are linear over time and increase when the temperature is lowered. The legend shows slopes and the goodness of fit.

The final results demonstrate that the freezing rate is nearly linear for both water and monomers. Therefore, the apparent increase in the freezing rate is really due to the delay in reaching uniform temperature inside the droplets owing to the influence of volume and high contact angles, as previously predicted by the COMSOL model. Although the droplets were cooled at a rate of 50 °C/min, which should have a greater impact on larger than smaller droplets, some of the curves, particularly for the 1µl droplets in figure (4-2) at lower temperatures, appear to require a longer delay time at the beginning than the 1 to 2 seconds calculated by the model. This can be attributed to the COMSOL simulation not including the thermal conductivity of the hydrophobic silicon substrate, since the temperature of the bottom surface of the droplet was set to the programmed temperature at $t = 0$. The poor thermal conductivity of the hydrophobic coating could contribute to an extended delay time. This extended delay time may also be noticed in suspended nanolitre droplets, particularly in oil with poor thermal conductivity, which may amplify this effect on the droplet, since their temperature may deviate from the target temperature reported by the cooling device. For

instance, if the programmed temperature is –30 ºC, it does not necessarily indicate that the temperature of the oil medium is immediately also –30 ºC, which may cause the freezing rate of droplets to increase due to the continuing cooling effect despite their small size. This also applies to levitated droplets in air due to its poor thermal conductivity [169].

The effect of the non-uniform inner temperature on the unfrozen fraction data does not always result in an increasing gradient; there are cases in which the unfrozen fraction is nearly linear for different droplet volumes, such as the 2 and 16 µl buffer droplets shown in figure (4-16). Even though the 1 µl and 16 µl droplets have the same contact angle and are cooled at the same rate, the impact of the inner temperature on the freezing rate differs between them when the programmed temperature is lowered. The freezing rate of larger droplets shows a less systematic increase, while the freezing rate of smaller droplets demonstrates a more systematic and predictable increase.

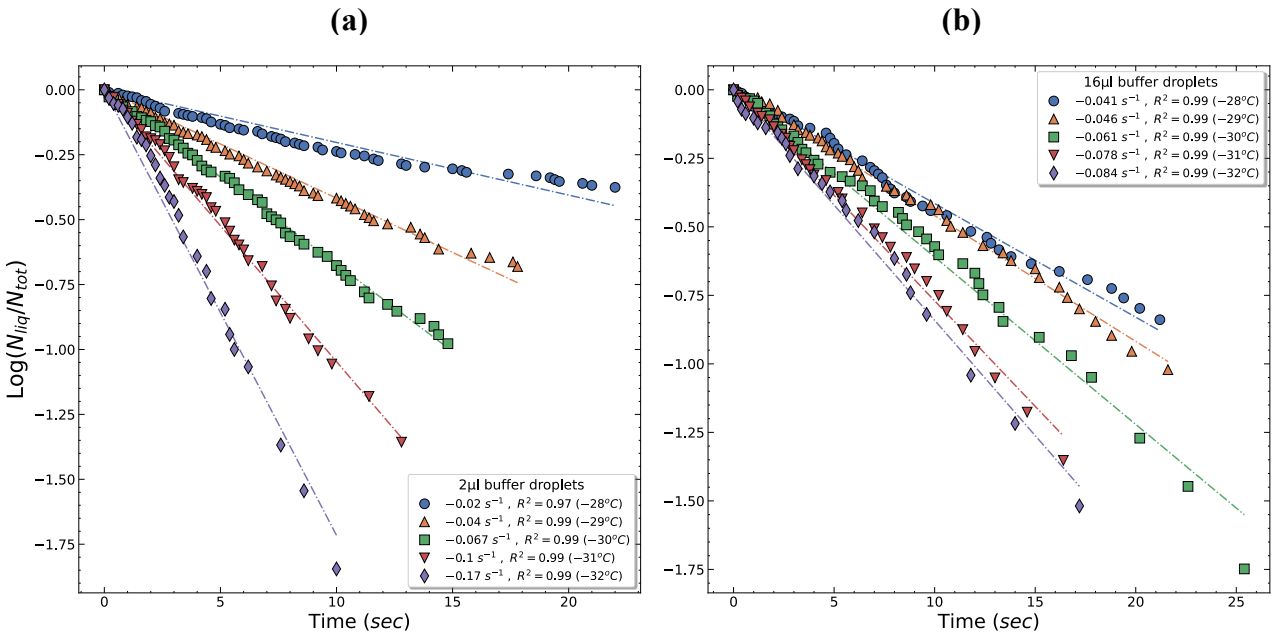

Figure 4-16: Data for two different volumes of buffer droplets at varying cooling temperatures, demonstrating a linear freezing rate. (a) demonstrates that the freezing rate of 2µl droplets increases systematically with decreasing temperature due to the short delay time necessary to establish a uniform interior temperature; hence, they are very sensitive to even the slightest temperature changes. (b) The freezing rate of 16µl droplets increases slowly with a decrease in temperature, and the increase is less systematic than that of 2µl droplets mainly as a result of their larger volume, which requires a longer delay time to achieve the desired temperature.

Figure (4-17) depicts another instance of freezing rate influenced by two different surface wettabilities (i.e. 90º and 110º) for Apoferritin monomer droplets. It strongly coincides with the simulation finding that when the contact angle between the droplet and the surface rises when the cooling rate is relatively high, the droplet is more susceptible to the non-uniform inner temperature effect, which delays its freezing. Both the 1µl and 8µl droplet freezing rates decrease at low surface wettability (hydrophobic surface) and increased at high wettability (hydrophilic surface) when they cooled at the same rate (50 ºC/min). The change in freezing rate was more pronounced for small droplets than for larger ones. This is because, as the droplet volume increases, they experience a greater non-uniform inner temperature effect, leading to a decrease in the freezing rate. In contrast, smaller droplets, acting as miniature temperature sensors, are less affected by this inner temperature impact, resulting in a more sensitive and increasing freezing rate.

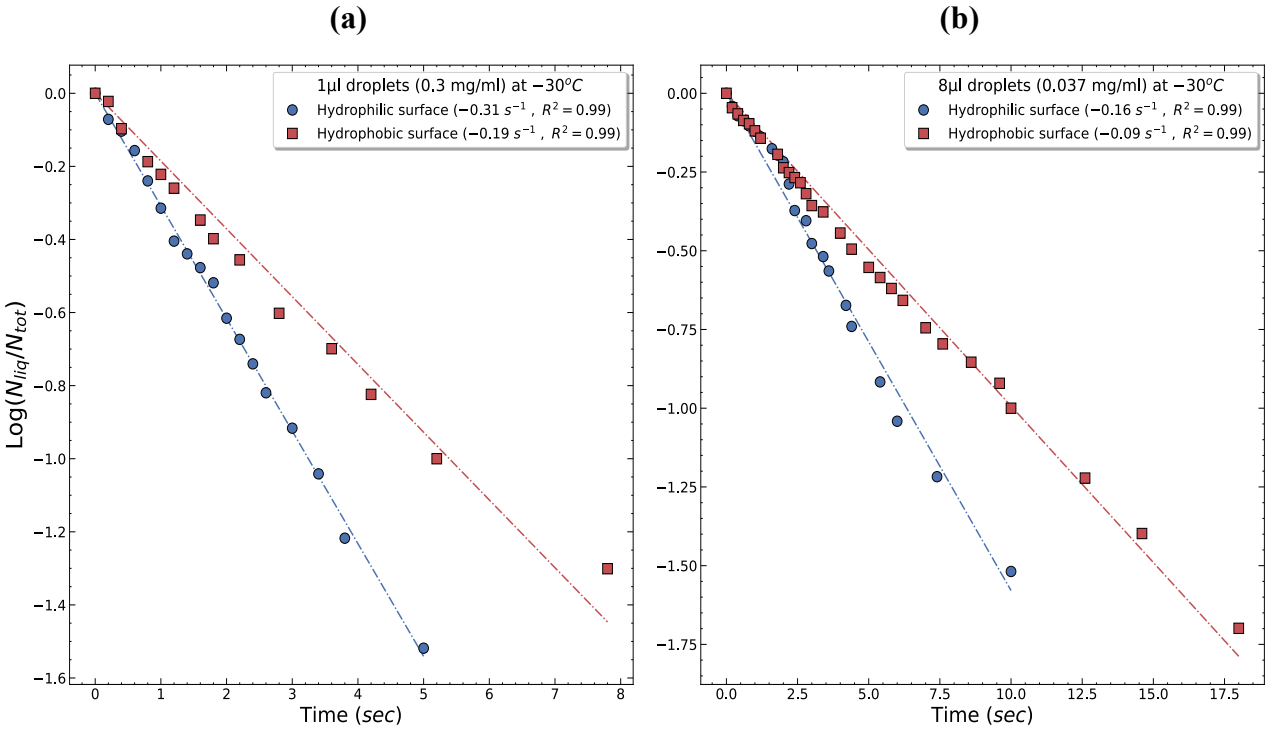

Figure 4-17: Comparison of the effect of surface wettability on monomer droplets of 1µl and 8µl size when cooled at a rate of 50 ºC/min. (a) The freezing rate of 1 µl droplets reduces when the wettability decreases and the contact angle is increased from 90º to 110º, and the same holds true for 8 µl droplets in (b), confirming the simulated association between delay time and contact angle at high cooling rate. As seen here, however, the degree of variation in freezing rate is highly dependent on droplet size. When the contact angle was reduced from 110º to 90º, there was a greater increase in the freezing rate of 1µl droplets compared to 8µl droplets.

In freeze-thaw ice nucleation experiments, the influence of the contact angle has also been detected. We observed that when a cooled droplet freezes, its volume grows and its shape alters, thus the contact angle changes and lowers when the droplet is thawed in comparison to its original CA before freezing. It was observed from the captured images that the droplet diameter increases slightly as the number of freezing-thawing cycles increases. This effect increases their freezing rate and could be mistakenly credited to the nucleation agent itself as having changed significantly. An example is shown in (figure 4-18). Although it could be argued that the increase in freezing rate is due to the accumulation of dust over time, the droplets were frozen in a well-sealed chamber during the experiments, and the number of frozen droplets of the 10th freeze-thaw cycle was nearly comparable to that of the initial sample. If the increase in freezing rate were due to dust, a number of droplets would freeze at higher temperatures, reducing the number of measured droplets.

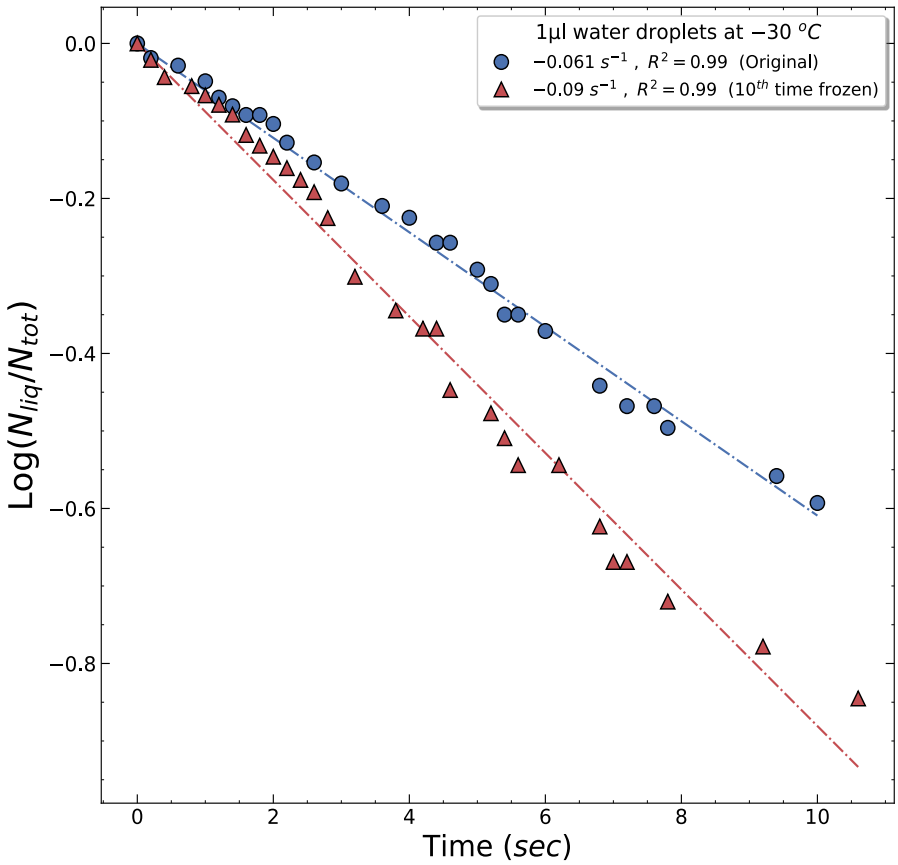

Figure 4-18: The influence of freeze-thaw cycles on the freezing rate of 1 µl droplets. The freezing rate of 10th-time frozen droplets increases because the freezing alters the droplet's shape, resulting in a reduction in the droplet's contact angle when it thaws. According to the simulation, this leads the droplet to cool and freeze more quickly.

4.3.3. Impact of an Oil Coating on the Rate of Freezing of a Droplet

One of the usual techniques used in immersion freezing measurements, primarily when freezing nanolitre or picolitre droplets, is to cover them with an oil coating or inject them into an oil medium, to form emulsions. The oil cover serves to prevent the rapid evaporation of droplets over time. The impact of the oil on the freezing rate of droplets is rarely considered and is often disregarded as a potential factor in ice nucleation. However, it is necessary to examine the influence of oil on the freezing rate in order to distinguish its effect from that of the investigated nucleating agent.

Figure (4-19) depicts 1μl droplets of Apoferritin monomers with a concentration of 0.6 mg/ml coated with a paraffin oil layer to replace their water/air interface with a water/oil interface during cooling. The freezing rate of droplets with a water/oil interface was clearly lower as compared to droplets without an oil coating, which froze faster. The freezing rate of the oil coated droplets increased consistently with decreasing temperature, like it does in the absence of oil coating. Despite the fact that the oil coating on droplets reduces their freezing rate, it does not appreciably affect the shape of the logarithm of unfrozen fraction curve; if it is linear, it remains linear, and if it is a curve, it remains a curve.

Proteins have a higher affinity for adsorption at the water/oil interface than at the water/air interface [152,170]. Although the process of protein adsorption is time dependent and requires a longer time period when compared to the time scale of the freezing experiments, it is possible that the oil-protein attraction could have some contribution to the freezing rate of the droplets. In the case of emulsions or droplets completely surrounded by oil, the oil influence on their freezing rate may increase over time due to the poor thermal conductivity of oil, which hinders droplets and oil from reaching the temperature that the cooling device records, as mentioned in the previous section.

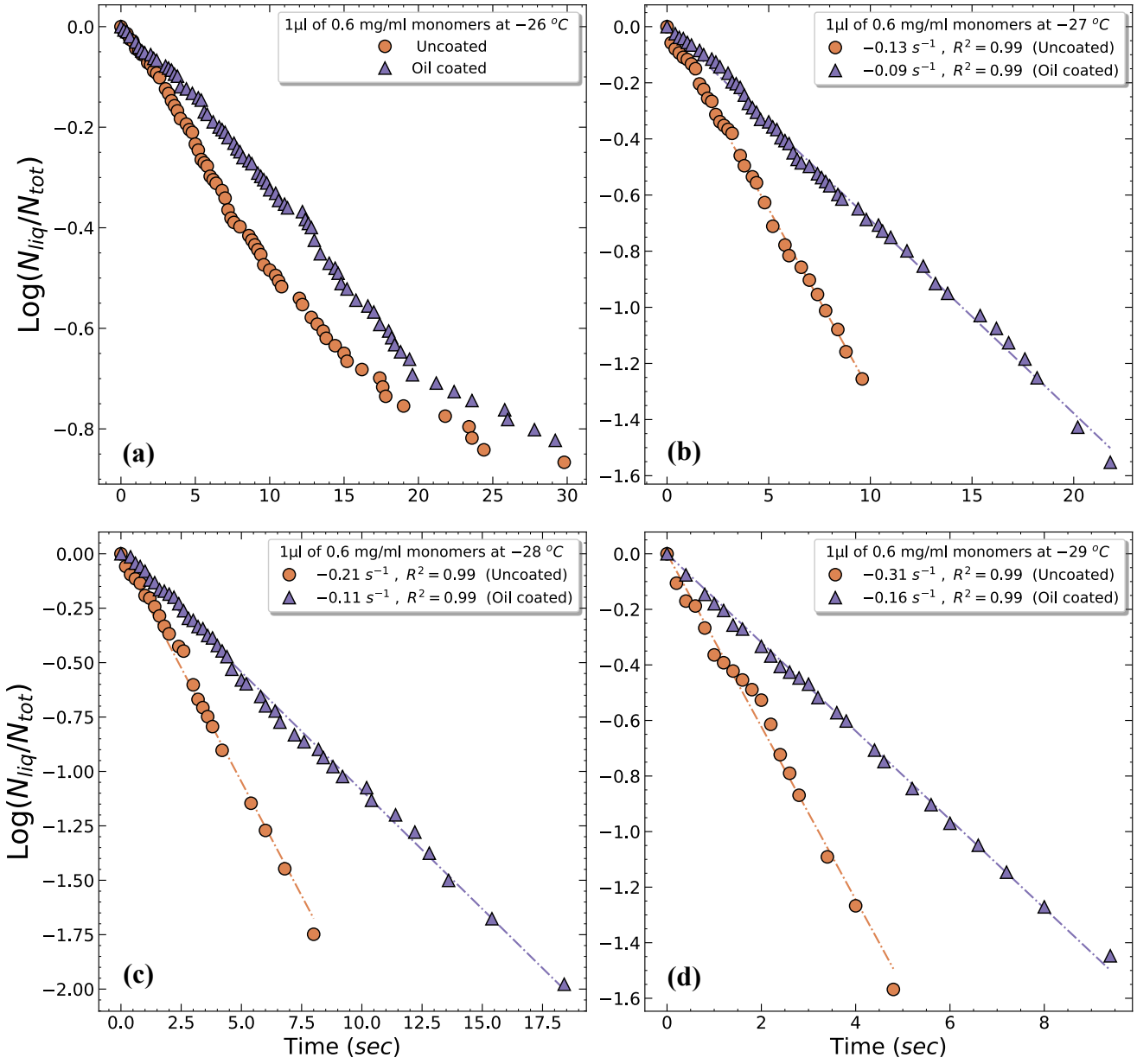

Figure 4-19: Freezing rates for paraffin oil-coated and uncoated droplets of Apoferritin monomers (0.6 mg/ml). In comparison to uncoated droplets, the oil coating of the droplets reduces their freezing rate over a range of low temperatures (a, b, c, d). The shape of the log unfrozen fraction of oil coated droplets does not change, but rather shifts toward longer freezing times. Calculated slopes are given when the log unfrozen fraction curve is linear.

4.3.4. The Influence of Non-ionic Surfactants on the Freezing Rate of Monomers

Surfactants are surface-active molecules because of their ability to segregate at the interfaces of aqueous solutions [171]. The general molecular structure is comprised of two major components: a hydrophilic group, known as the head, and a hydrophobic group, known as the tail. These two groups provide the surfactant molecule with the ability to interact with molecules containing either hydrophobic or hydrophilic groups, making them amphiphilic. The non-ionic surfactants Tween 20 and Tween 80 are neutrally charged molecules and are members of the same surfactant family known as Polysorbates. The main difference between Tween 20 and Tween 80 is that Tween 80 has a longer tail and, therefore, a greater molecular mass. These two surfactants are frequently used to stabilise proteins and enhance their water solubility. In addition, these molecules are non-invasive (do not alter or denature the protein) and are utilised to reduce the development of protein aggregates in solutions [172]. Surfactant molecules are capable of adsorption at both water/air and water/solid interfaces [171]. For instance, when 1% v/v (8 M) of surfactant Tween 80 is added to buffer droplets, as shown in figure (4-20), the droplet contact angle decreases rapidly compared to surfactant-free droplets whose contact angle remains higher on the same solid surface. This is because Tween 80 decreases the surface tension of the buffer by adsorbing its molecules at the droplet's interfaces.

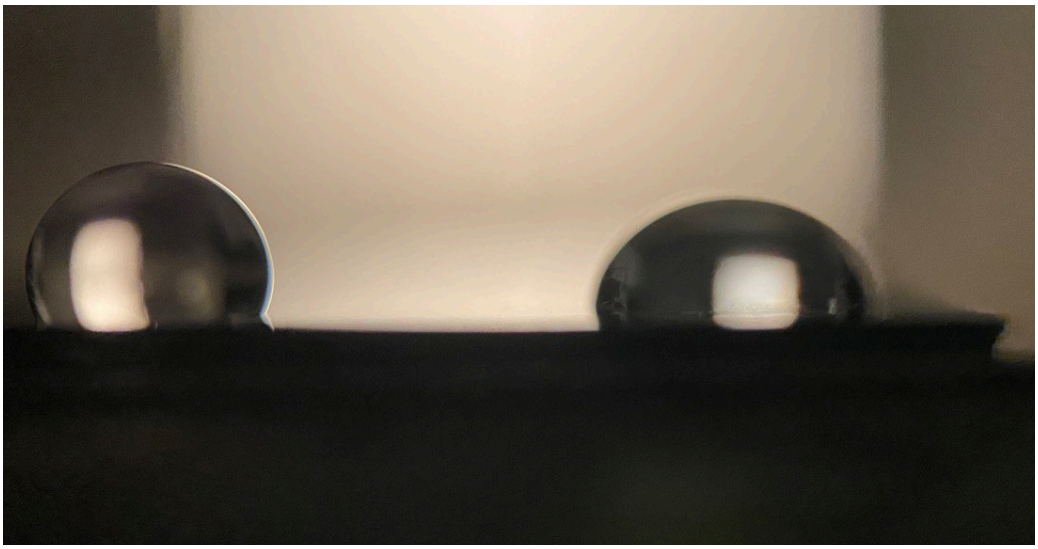

Figure 4-20: Contact angle of two buffer droplets, one without surfactant (left) of ≈120^{o} and the other with Tween 80 (1 % v/v) (right) of ≈85^{o}. The surfactant significantly lowers the contact angle between the droplet and the substrate due to the strong adsorption of Tween 80 molecules at the droplet interfaces, which decreases the surface tension of the droplet dependent on the concentration of the surfactant in the liquid.

To study the influence of surfactants on the freezing rate of proteins e.g. Apoferritin monomers, 0.7 µM of Tween 20 and Tween 80 was added to a 0.75 mg/ml solution of monomers. Since the concentration of surfactant is low (below the micelle formation threshold), it does not significantly alter the contact angle of the droplets relative to the surfactant-free droplets however the viscosity of the surfactant-protein solution has reduced. Figure (4-21) presents results for 1µl droplets with and without surfactant containing the same amount of proteins. The freezing rate decreases in the presence of surfactants.

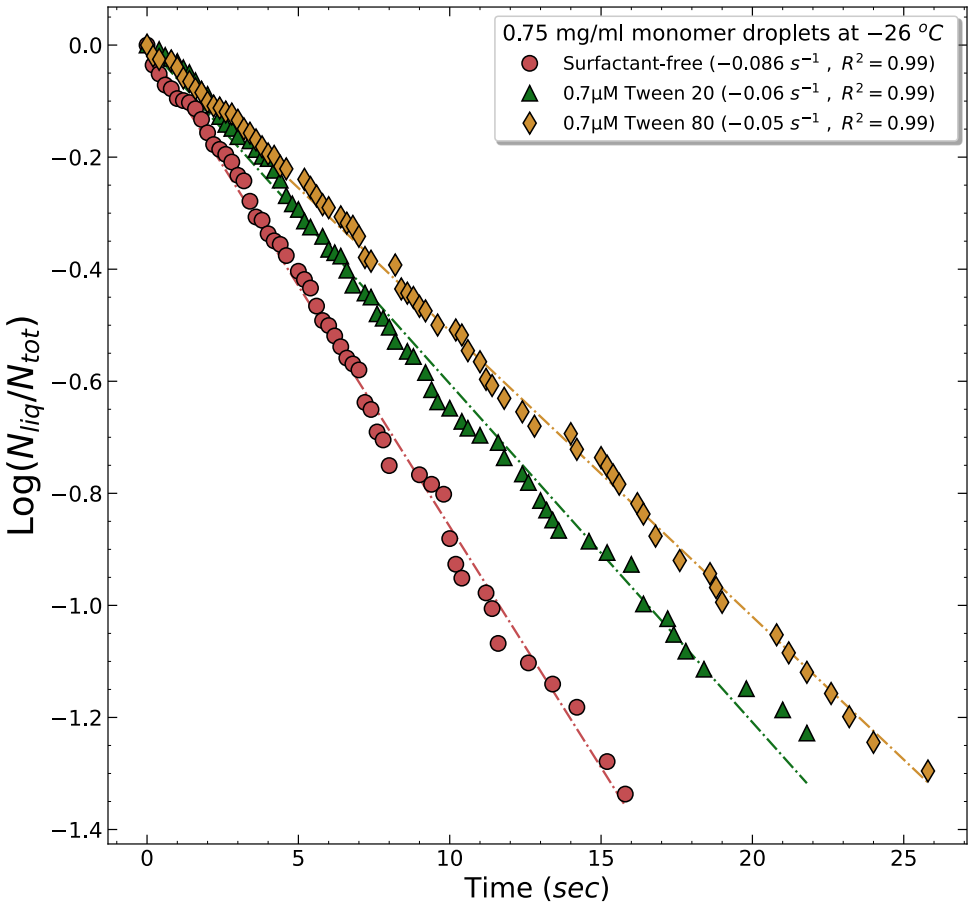

Figure 4-21: The rate of freezing of 0.75 mg/ml monomers droplets of 1µl size with 0.7 µM Tween 20 and Tween 80. Droplets with surfactants have a lower freezing rate than droplets without surfactants.

There are two possible explanations for this decrease in freezing rate: i) the addition of surfactant to the protein solution may have decreased the likelihood of protein clustering, which are most often responsible for high freezing rates of monomer droplets, particularly in high concentration proteins, such as 0.75 mg/ml, but, it's likely that such a process might take a lot longer than the experiment's time scale. [158]. ii) Since proteins and surfactants both adsorb at interfaces, they will compete to adsorb at the interfaces of the droplets. Surfactant molecules will ultimately displace proteins at water/air and water/solid interfaces over time [171,173]. Either one of these two causes or both combined could contribute to the reduction in the freezing rate of proteins when surfactants are present, in the case of explanation (ii) it indicates that proteins adsorbed at the interfaces of the droplets play a crucial role in freezing.

4.4. Conclusion

The ice nucleating agent is not always responsible for the shape of the log-unfrozen fraction curve. The volume of the droplet and the wettability of solid surface have a considerable impact on the apparent rate of freezing. A finite element model was used to compute the needed delay time for a static water droplet to achieve a uniform interior temperature as a function of the contact angle and droplet volume. The simulation reveals a linear relationship between the delay time taken to obtain uniform temperature and the contact angle of the droplets.

Moreover, the delay time increases with droplet size, resulting in a lower freezing rate for bigger droplets compared to smaller ones. In addition, there is a significant relationship between cooling rate, contact angle, and droplet volume that affects how uniform the temperature is inside a droplet. Large droplet volumes with high contact angles need to be cooled slowly to reach a uniform inner temperature.

Experimental data for water and Apoferritin monomers of varying droplet volume corroborate the simulation prediction that when droplets are deposited on a substrate with low wettability, the freezing rate will increase during the experiment due to the effect of a non-uniform temperature inside the droplets, and this effect is amplified as droplet size increases. Based on the simulation findings, points prior to the delay time were eliminated from log-unfrozen fraction data, yielding a nearly linear log-unfrozen fraction.

There are other factors that influence the freezing rate of droplets, such as the fact that oil-coated droplets freeze more slowly than uncoated droplets while maintaining the shape of the

freezing curve. The addition of non-ionic surfactants, like Tween 20 and Tween 80, to a buffer solution or protein solution will slow the freezing rate because they are surface-active molecules that adsorb at the droplet interfaces and ultimately displace proteins. Surfactants are also known to reduce protein aggregation and clustering. In conclusion, we demonstrated that the isothermal freezing approach can be highly sensitive in detecting minor experimental differences produced by sources other than the ice nucleation agent.

5. ICE NUCLEATION BY DNA ORIGAMI

5.1. Introduction

In order to get a better understanding of the process of ice nucleation, in particular the mechanism of critical nucleus formation on an INP surface, a number of studies have used a wide variety of INPs, both organic and inorganic, that are present in the atmosphere as models and examples.

However, ice nucleation is a surface process, which is influenced by INP surface characteristics such as shape and size. It is difficult to study these variables by comparing materials of different and random shapes and sizes. For instance, if we want to investigate how a particular site, such as where two surfaces meet at an angle, enhances the effectiveness of the nucleation process, it is difficult to identify a single INP where the required angle can be varied in a well-controlled manner.

Paul Rothemund developed the DNA origami technique used here, in 2006, which enables nanostructures to be designed by folding single DNA strands using a scaffold and staples [174–176]. Due to well-established protocols, DNA origami can be synthesised to build regular and complex structures with a great degree of precision, including cubes, tubes, tiles, and various more intricate and custom-made shapes [177–181]. These powerful properties of the DNA origami method make the resulting nanostructures good candidates for studying heterogeneous ice nucleation, especially in experiments where the geometry and surface properties of a single nanoparticle species can be varied in a controlled way.

Here, we examine DNA origami tiles as a model for heterogeneous ice nucleation using the. constant cooling rate and isothermal methods and interpret the findings using classical nucleation theory (CNT).

5.2. Method and Sample Preparation

5.2.1. DNA Origami Synthesis

To prepare DNA origami tiles, 100 nM of circular single-stranded DNA scaffolds (templates) were extracted from bacteriophage M13mp18; each scaffold has 2646 nucleotides. The obtained scaffolds were then mixed with 200 nM of 32 nucleotide DNA short strands known as staples. Well-folded DNA origami was produced using the DNA annealing process, which involves heating a mixture of scaffolds and staples to 95 ^{o}C and then gradually cooling to 25 ^{o}C at a rate of 1 ^{o}C per minute in 10 mM Tris-HCL buffer (pH 8),12.5 mM $MgCl_2$ and 1mM EDTA [176].

The DNA origami tiles were designed and synthesised by our University of Oxford collaborators, Jonathan Bath and Andrew Turberfield [182–187].

5.2.2. Sample Preparation for AFM Imaging

For good coverage, the DNA origami solution was diluted 10-fold with Tris-HCl buffer (pH 8) to a final concentration of 10 nM. On a freshly cleaved mica substrate, 20 µl droplets were deposited and incubated for 10 - 15 minutes at room temperature. The substrate was then rinsed with Milli-Q water multiple times. Finally, the substrate was dried with nitrogen gas and was then ready for AFM imaging [176,188].

5.2.3. Droplet Assays and Freezing Experiments

The DNA origami frozen fraction as a function of temperature, the isothermal freezing rate, and parameters from classical nucleation theory were determined using the same protocols and data analysis methods as in previous chapters.

5.3. Results and Discussion

5.3.1. DNA Origami Tiles

The Japanese term origami refers to the art of folding paper into many forms. DNA origami is the process of folding a single long DNA strand into various desired nanostructures using several short DNA strands. The long strand is referred to as the scaffold or the template, whereas the short strand is referred to as the staple [175]. The process of DNA folding is facilitated by the self-assembly of complementary base pairs of the strands. Each single strand has a unique sequence of four DNA bases, adenine (A), cytosine (C), guanine (G), and thymine (T), which pair with another strand of a complementary sequence such that (A) pairs with (T) and (G) pairs with (C) to form double-stranded DNA, which is referred to as a helix because of its resulting shape [175,188]. To generate a well-folded DNA origami tile, a combination of scaffolds and staples is normally heated to a high temperature and subsequently cooled to room temperature at a gradual cooling rate, a process known as DNA annealing. See figure (5-1) for a synopsis of this procedure.

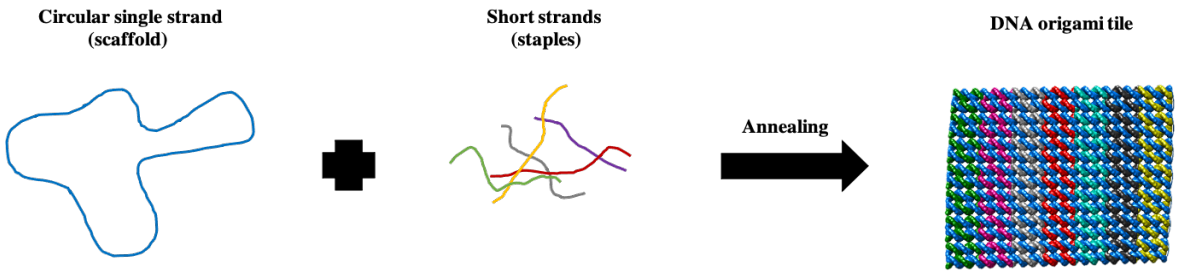

Figure 5-1: The diagram illustrates the process of DNA origami folding by annealing. When a long circular scaffold (single stranded DNA) is combined with an excess number of staples (complementary short strands) and the mixture is heated to a high temperature, such as 95 ºC, then slowly cooled to room temperature, the yielded construction is a well-folded DNA origami structure, for example a 2D rectangular shape. Each well-folded tile consists of a certain number of tightly packed DNA helices (in blue) and staples (in colours).

Proteins, unlike DNA origami, can only fold in a limited number of ways and into a small number of configurations for example, globular proteins. This limited folding capacity makes it more challenging to design proteins., whereas DNA origami can be designed into a wide range of 2D and 3D nanostructures using well-established synthesis protocols.

Prior to DNA origami synthesis, the target shape can be designed using open-source software packages such as the "caDNAno" interface, which enables users, including those with limited prior knowledge of DNA origami, to create a variety of configurations using simple, automatic built-in tools to build scaffold and staples in either square or honeycomb lattices; figure (5-2) shows a schematic example design of DNA rectangular origami [179].

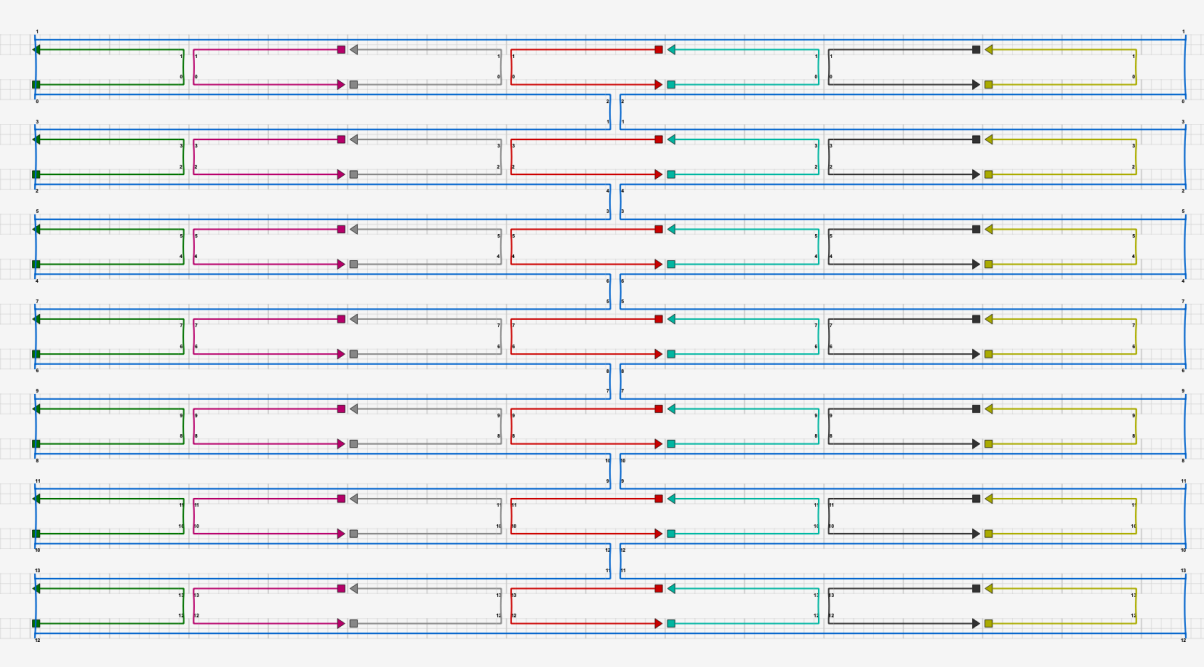

Figure 5-2: A schematic illustration of a simple rectangular DNA origami design using the caDNAno interface. The model depicts a lengthy scaffold in blue with U-shaped short staples shown in various colours and a square DNA lattice.

To reduce the time and cost of the synthesis process, the efficiency of the designed origami structure can be simulated and monitored by submitting the caDNAno model to another online open-source programme, such as "CanDo" which will predict the flexibility of the DNA nanostructure in a solution at room temperature with images and video simulations of the results, as demonstrated in figure (5-3) for an origami tile [189].

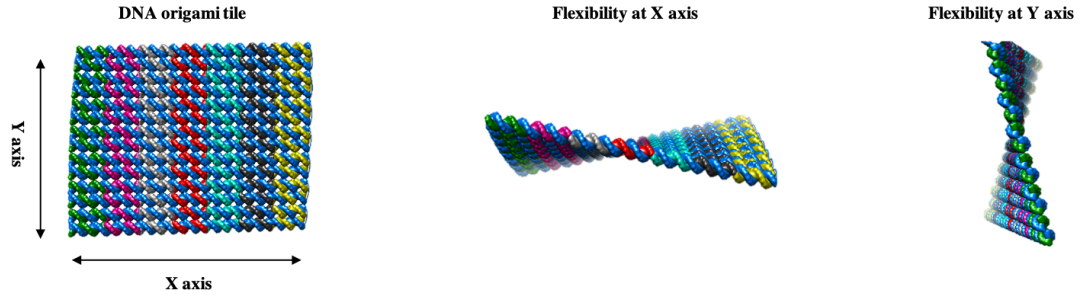

Figure 5-3: CanDo website simulation results after submitting a caDNAno design. The simulation predicts the flexibility of a DNA origami rectangle in a solution at 25 ^{o}C ambient temperature. The flexibility was simulated for the X and Y side views of the tile's height and width, indicating that the origami tiles fluctuate in aqueous solutions.

The scaffold used in origami synthesis is often extracted from the bacteriophage M13mp18 genome, which comprises around 7249 nucleotides that may be trimmed to the necessary length which determines the size of the origami structure, while the staples have approximately 32 nucleotides [174,175,188,190]. The theoretical diameter of double-stranded DNA is approximately 2.25 nm, which determines the thickness of a simple rectangular DNA origami tile, as shown in figure (5-4).

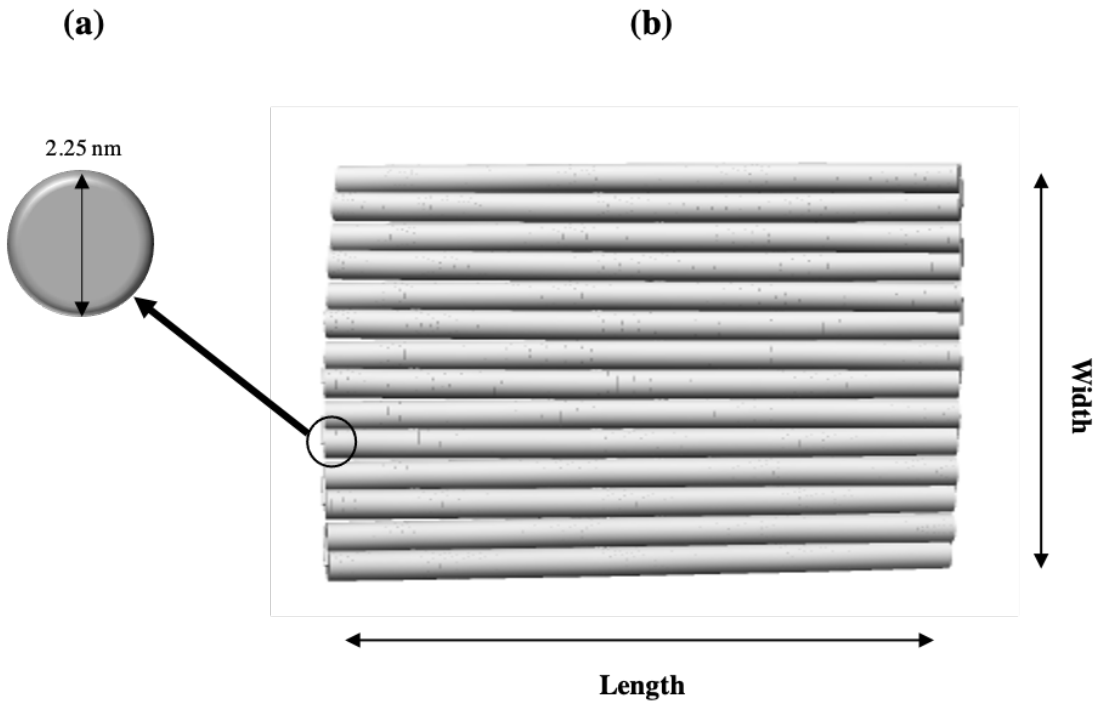

Figure 5-4: Dimensions of the DNA origami tile. (a) A side view of a single DNA helix has a diameter of around 2.25 nm which is equal to the thickness of a single DNA tile. (b) The length of the simplified double-stranded DNA cylinders is equal to the length of the origami tile, and the sum of the diameters of all the cylinders equals the width.

Moreover, the length of the tile corresponds to the length of a single helix that has been approximated as a cylinder, while the width corresponds to the sum of the diameters of all the cylinders [188]. In this chapter, rectangular DNA origami tiles with a monomer size (a single well-folded DNA origami tile) of 80 nm x 40 nm in buffer solution [176] were used for ice nucleation measurements. Figure (5-5) shows an Atomic Force Microscopy (AFM) image of well-folded DNA tiles.

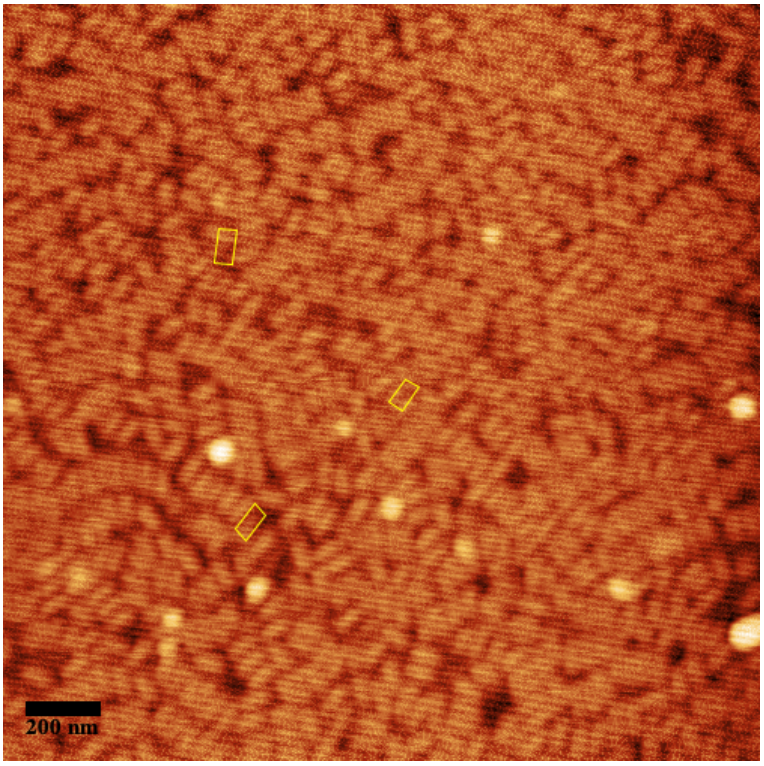

Figure 5-5: AFM image of 10 nM DNA origami rectangles deposited on a mica substrate. The tiles were used in further freezing experiments. The image demonstrates excellent coverage; the X and Y dimensions of a single tile (monomer) are about 80 nm x 40 nm. The yellow frames indicate individual tiles.

5.3.2. Frozen Fraction of DNA Origami Tiles

In order to apply the DNA origami technique in ice nucleation studies, it is necessary to determine if basic DNA origami structures, such as rectangles, can induce water freezing in the first place. It is also necessary to determine if the effectiveness of freezing is specific to DNA strands or to the origami structure. The samples studied included quenched origami tiles (S1), unannealed DNA (S2), well-folded DNA origami tiles (S3), templates (S4), staples (S5), and buffer (S6). Table 5-1 summarises preparation procedures of the samples used in the freezing experiments of 1µl droplet assays.

Table 5-1: DNA origami samples.

Sample	Preparation
Quenched DNA origami tiles (S1)	Well-folded DNA origami tiles were heated to 96 °C and cooled rapidly to 0 °C at a rate of 100 °C/min.
Unannealed DNA (S2)	A mixture of staples and template in a 2:1 stoichiometric ratio in buffer.
Well-folded DNA origami (S3)	(S2) mixture is annealed by cooling from 96 °C to 25 °C at 1 °C /min.
DNA template (S4)	2646 nucleotide single-stranded circular DNA at a concentration of 100 nM.
DNA staples (S5)	A mixture of 32 nucleotide DNA short strands at a concentration of 200 nM.
Buffer (S6)	12.5 mM ($MgCl_2$), 1 mM (EDTA), 10 mM (Tris-HCl) at pH 8.0.

Figure (5-6) illustrates the frozen fraction of each sample as a function of temperature using a constant cooling rate approach. DNA origami tiles (S3) freeze at higher temperatures than the individual DNA components, templates (S4) and staples (S5), which both freeze at temperatures very close to those of the buffer (S6). It is evident that the freezing process is not particular to the DNA components, but rather to the physical surface of the DNA origami structure, since it is a more efficient INP compared to the same concentration of templates and even twice the concentration of staples.

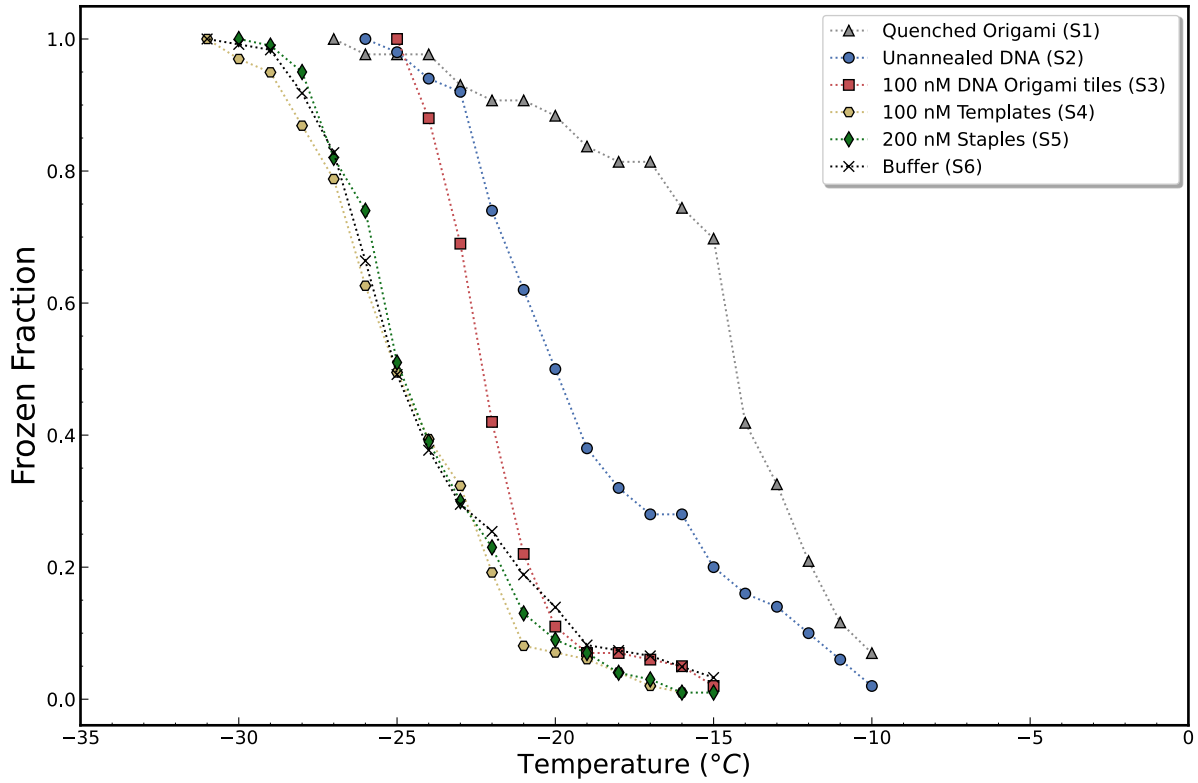

Figure 5-6: The frozen fraction of 1µl droplets containing DNA origami or components as a function of temperature. It demonstrates that well-folded DNA origami tiles (S3) are more effective INPs than templates (S4) and staples (S5) that freeze near the buffer freezing temperature (S6). Unannealed origami (S2) and quenched origami (S1) both freeze at higher temperatures possibly due to aggregation.

On the other hand, the data for a combination of DNA components (S2) demonstrates that the droplets freeze at a higher temperature than well-folded tiles. Since templates and staples have complementary DNA base pairs, these single strands will automatically self-assemble to form double stranded DNA; however, if the mixture is not annealed, the resultant structure will be poorly folded origami with irregular structures, and likely forming DNA aggregates. This could explain why they freeze at higher temperatures than properly folded tiles that have undergone the annealing process, which exhibit a narrower range of freezing temperatures.

The slow cooling rate of the heated DNA mixture during the annealing process is a crucial factor in the production of homogeneous DNA origami structures. For instance, when origami tiles were formed by rapid cooling (quenching) from a high temperature (96 ºC), amorphous and less homogeneous origami structures could be formed as well as aggregations [191]. The freezing point of quenched origami (S1) has shifted toward higher temperatures than well-annealed origami (S3), and droplets freeze over a wider range of temperatures. The wide range

of freezing temperatures of (S1) and (S2) is comparable with the wide range of freezing temperatures observed in Chapter 2 for Apoferritin oligomers due to the presence of aggregates.

5.3.3. Comparing Experimental Findings with Existing Literature

The ice nucleation efficiency of nucleic acids has yet to receive thorough investigation. However, a recent study by A. Alsante et al. [98] examined the freezing ability of DNA and RNA using a constant cooling rate method to determine the frozen fraction of nucleic acids. The main distinction between DNA (Deoxyribonucleic Acid) and RNA (Ribonucleic Acid) lies in their structures. DNA is a double-stranded molecule with a deoxyribose sugar backbone, while RNA is typically single-stranded with a ribose sugar backbone and contains the base uracil (U) instead of thymine (T) [192].

For the freezing study, two sources of DNA were used. DNA 1 was obtained from herring sperm at a concentration of 0.5 mg/ml, whereas DNA 2 was extracted from laboratory-grown Synechococcus elongatus and measured at a lower concentration of $5x10^{-4}$ mg/ml. Droplets containing DNA 1 exhibited freezing temperatures ranging from −14 to −26 °C, while DNA 2 droplets began freezing at lower temperatures between −18 to −26 °C due to their lower concentration. Interestingly, the freezing temperature range of DNA is comparable to that of DNA origami tiles (S3) with a concentration of around 0.08 mg/ml, ranging from −15 to −26 °C. This implies that double-stranded DNA could potentially exhibit similar effectiveness as the origami tiles. It is essential to distinguish whether the freezing is induced by the predominant DNA molecules, either double-stranded or origami tiles, or by the rare effective INPs such as aggregates or poorly folded origami. Therefore, in the next section, we will conduct isothermal measurements on the annealed (S3) and unannealed (S2) DNA origami samples to address this question.

Droplets containing RNA molecules from Escherichia coli at a concentration of 0.5 mg/ml were found to freeze within a range of −13.5 to −26 ºC, which is similar to the freezing range of DNA. Despite being single-stranded, RNA molecules exhibited higher freezing ranges compared to DNA templates (S4) (single-stranded DNA), which we found to exhibit weak ice activity. This suggest that RNA either functions as better INPs or indicates the presence of some aggregates in the sample. the paper did not provide additional details regarding the size, length, or purity state of the DNA and RNA samples used, aside from their sources.

A. Alsante et al. categorized nucleic acids as moderately effective and not highly effective INPs. However, our findings demonstrated that DNA aggregates, such as the quenched origami (S1) and unannealed DNA (S2), can also serve as highly effective INPs, freezing at higher temperature ranges starting from −10 ºC.

Moreover, the freezing temperatures observed in 1 µl droplets containing DNA origami tiles have displayed a higher freezing range in contrast to the freezing behaviour of Apoferritin subforms, dimers and monomers. However, this could also be attributed to the larger surface area of DNA origami compared to the spherical cages of Apoferritin dimers and monomers. Nevertheless, our results indicate that Apoferritin oligomers are one of the most efficient INPs, surpassing even DNA origami aggregates (S1) and (S2). Nonetheless, the advantage of employing the DNA origami technique lies in its ability to design complex and intricate structures that mimic the complexity of aggregates, potentially leading to the development of improved INPs.

5.3.4. DNA Origami Tiles Freezing Rate

In order to determine the freezing rate of the origami rectangles' droplets, isothermal measurements are helpful. When freezing the same amount of annealed (well-folded) and unannealed (partially folded) origami tiles, (S2) and (S3) samples, the log of unfrozen fraction as a function of time differs for both as shown in figure (5-7).

Droplets of well-folded origami tiles freeze at a constant rate over time, and the mean freezing rate increases as the temperature decreases. The droplets with unannealed origami, on the other hand, freeze at different rates over time, since the log of unfrozen fraction curves at different temperatures are non-linear, even at temperatures where the freezing rate for well-folded tiles is constant.

The data suggest that the source of the linear log-unfrozen fraction is homogeneous DNA origami structures (annealed), while the source of the curved log-unfrozen fraction is heterogeneous origami structures, poorly folded origami, and larger DNA strand aggregates. This is in line with the frozen fraction data, which suggest that unannealed origami forms more efficient INPs than well-folded origami, not only because they cause freezing at warmer temperatures, but also because the log ($\frac{N_{liq}}{N_{tot}}$) remains non-linear at lower temperatures. This indicates that there are different amorphous origami structures with different freezing abilities distributed in the droplets, resulting in a range of freezing rates. This is consistent with the broader frozen fraction curves for unannealed origami (S2) compared to the well-folded tiles (S3) in figure (5-6).

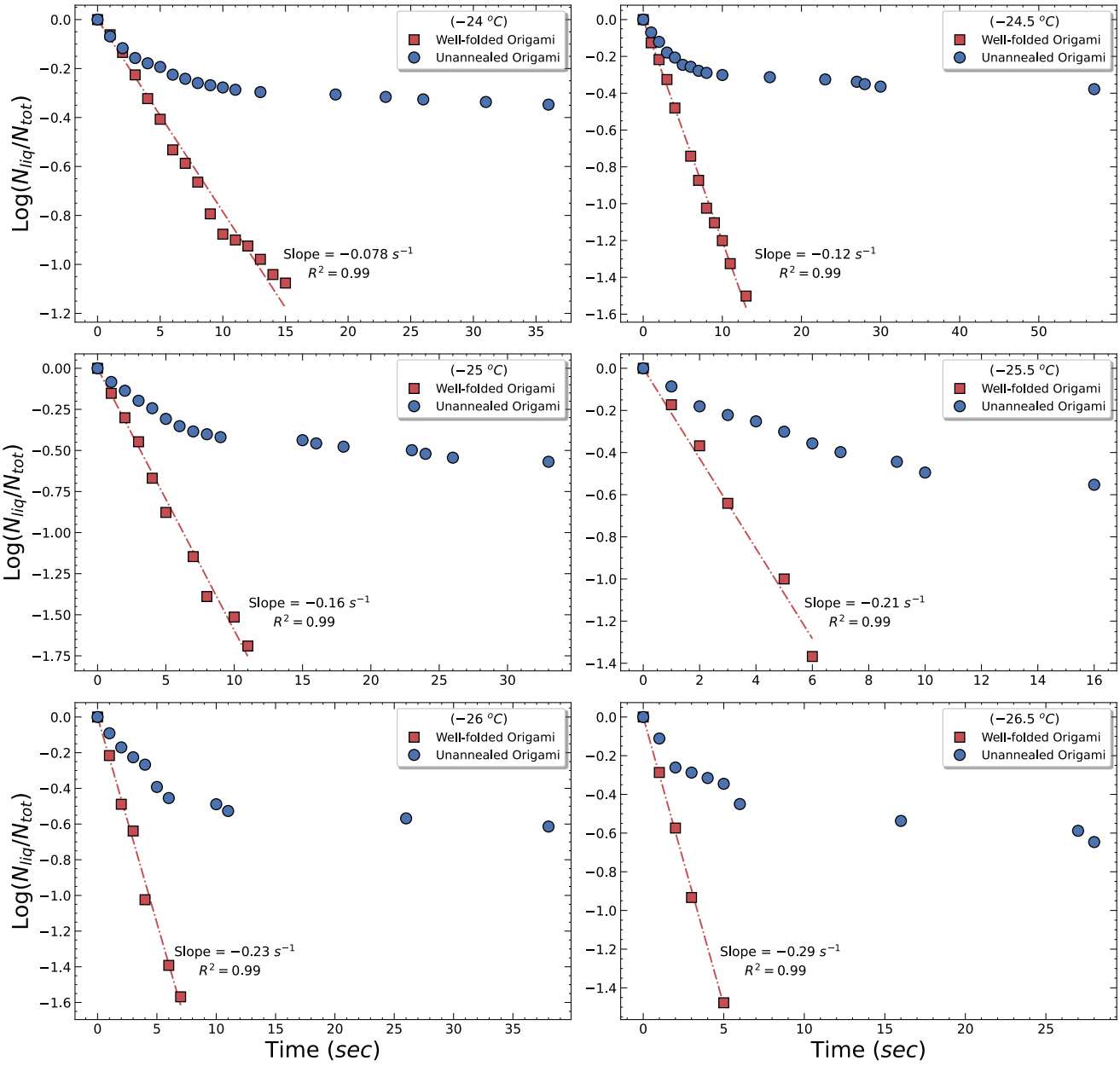

Figure 5-7: Log of the unfrozen fraction of 1µl droplets of well-folded (S3) and unannealed (S2) origami containing the same mass of DNA. 100 nM well-folded tiles display a single, mean freezing rate increasing with decreasing temperature, whereas at the same temperatures, unannealed origami shows a range of freezing rates due to its less homogeneous DNA structures. The data for well-folded origami were fitted to a straight line.

5.3.5. Fitting Data to Classical Nucleation Theory (CNT)

To determine the ice nucleation rate for the DNA origami tiles, the mean freezing rates previously obtained from isothermal freezing experiments at different supercooling temperatures were fitted using equation (3-5) to derive the key CNT parameters. Figure (5-8) compares the heterogeneous nucleation rates of DNA origami monomers (tiles) and Apoferritin monomers (spherical protein cages), which were explored in Chapter 3. J_0 and η are the only two free parameters in the CNT fit to each set of points. The parameters determined from the fitting are shown in table 5-2.

Table 5-2: Key parameters of classical nucleation theory (CNT). η [K^3] a constant that contributes to the free energy barrier, J_0 [(µg.s)$^{-1}$] the kinetic factor, $f(\theta)$ the shape factor.

Biomolecule	$\boldsymbol{\eta}$ $[\boldsymbol{K^3}]$	$\boldsymbol{J_0}$ $[(\boldsymbol{\mu g}\,.\boldsymbol{s})^{-\mathbf{1}}]$	$\boldsymbol{f(\theta)}$
Monomer	$8.39 \pm 0.07 \times 10^6$	$10^{38 \pm 0.23}$	0.62 ± 0.005
Dimer	$6.95 \pm 0.04 \times 10^6$	$10^{35 \pm 0.16}$	0.52 ± 0.003
Cluster	$8.33 \pm 0.03 \times 10^5$	$10^{5.5 \pm 0.02}$	0.06 ± 0.0001
DNA origami tile	$2.46 \pm 0.01 \times 10^6$	$10^{18 \pm 0.05}$	0.18 ± 0.001

The CNT parameters suggest that DNA origami tiles are a more efficient INP than Apoferritin monomers and dimers, since DNA origami requires a lower energy barrier to nucleate ice than protein. As a consequence, the reduction in the nucleation barrier caused by DNA origami is greater, according to the shape factor values $f(\theta)$. This efficacy of DNA tiles may be attributed to their greater surface area compared to Apoferritin monomers, which enhances the probability of freezing at higher temperatures. Additionally, DNA tiles are flat, though flexible while Apoferritin monomers have curved surfaces. The nucleation rate for DNA origami increases with decreasing temperature, reaching a value of approximately $J_0 \approx 10^{18}\ (\mu g.s)^{-1}$,which is nearly equal to the nucleation rate range for Apoferritin monomers.

Based on the obtained CNT parameters, it is evident that DNA origami tiles exhibit higher ice nucleation efficiency compared to spherical Apoferritin monomers and dimers, although they are less efficient than Apoferritin clusters. DNA origami tiles, similar to Apoferritin monomers, lack specific active sites such as pores or voids. Therefore, the enhanced efficiency of DNA origami tiles likely stems from their larger surface area in comparison to Apoferritin monomers. A single origami tile approximately has a surface area of ~6880 nm², whereas a single Apoferritin monomer has an area of ~452.38 nm². This implies that a single DNA origami tile offers around 15 times more exposed surface area to water than an Apoferritin

monomer, significantly increasing the probability of interacting with water molecules and thereby enhancing the likelihood of ice nucleation on its surface. Fletcher's equation discussed in Chapter 1 demonstrates that curved surface nucleation efficiency can be evaluated using the parameter $x = \frac{R}{r_c}$, where R is the radius of the spherical INP and r_c is the radius of the critical ice nucleus. The energy barrier required to initiate a stable ice nucleus by a spherical particle can be reduced when the particle's radius is sufficiently large to be treated as a flat surface, which occurs when $x \gg 1$. This aligns with the notion that DNA origami tile here represents a flat surface with a considerable surface area for initiating a stable ice nucleus, in contrast to spherical Apoferritin monomer. Furthermore, this suggests that an INP with a large surface area may facilitate ice nucleation better than a smaller INP with an active site on the surface such as dimers with a conical pore. Another significant contributing factor to the ice nucleation efficiency of DNA origami tile is the contact angle between its surface and the ice nucleus. The shape factor value $f(\theta)$ indicates higher wettability and a smaller contact angle, implying a higher degree of interaction between water molecules and the origami surface.

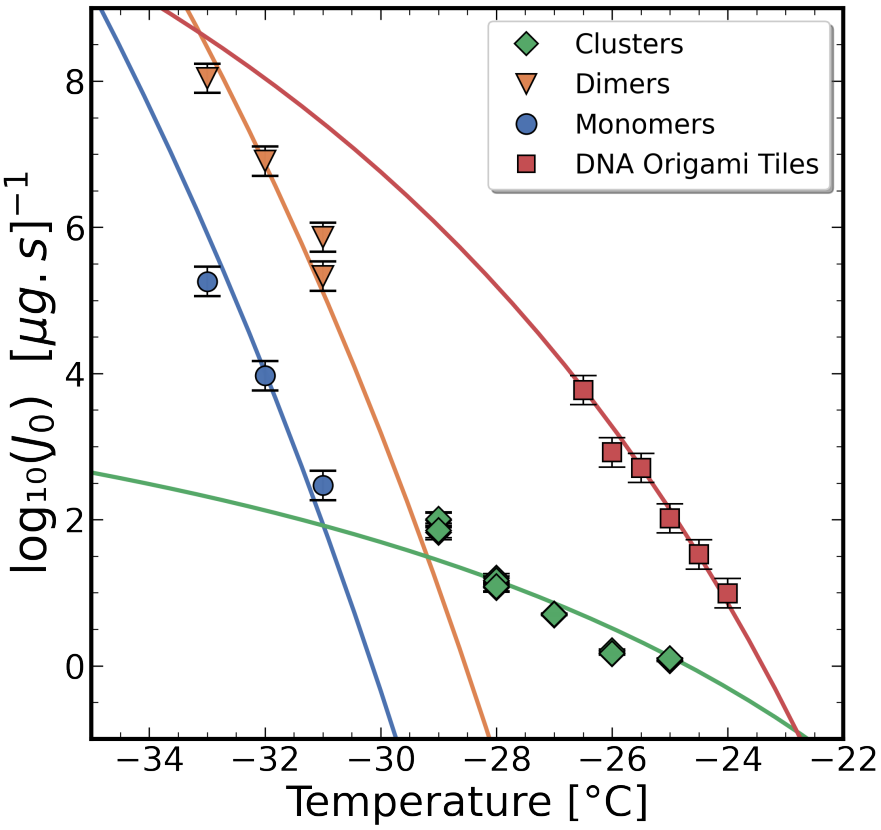

Figure 5-8: The nucleation rate of DNA origami tiles and Apoferritin subforms as a function of supercooling temperature (Apoferritin subforms were previously evaluated in Chapter 3). The freezing rates (s^{-1}) retrieved from the time-dependent tests were normalised by concentration (nM) and droplet volume (cm^3) prior to being fitted to the CNT model. It is clear that DNA origami is efficient since it initiates freezing at higher temperatures than Apoferritin monomers and dimers and has a lower energy barrier to overcome.

5.4. Conclusion

The ice nucleation ability of DNA origami was explored in this chapter. Annealed origami was found to be more effective as INPs than the DNA building blocks, namely scaffolds and staples, indicating that the physical structure of the origami is the most significant factor in the freezing process. In addition, we employed the isothermal freezing technique to cleanly extract the freezing rate of the origami; the result demonstrated a single freezing rate due to the homogeneous origami structures in the droplets.

When the results were fitted to classical nucleation theory (CNT) to determine the nucleation rate of the DNA origami tiles, an excellent agreement was obtained for plausible values of the parameters. It is intriguing that DNA origami has a lower energy barrier than proteins e.g. Apoferritin monomers. This is promising as it suggests that DNA origami might serve as an appropriate potential model for future research on the nucleation of ice. Because it is possible to produce homogeneous structures, this will help a great deal in reducing the amount of uncertainty in experimental observations by allowing for the detection of the characteristic freezing rate associated with a single geometry.

6. CONCLUSIONS AND RECOMMENDATIONS

The key outcome of this research is a better understanding of the role that biomolecules play in the nucleation of ice in the atmosphere. The nucleation rate obtained from constant cooling rate method was less reliable because it was not obtained directly, but rather by converting the frozen fraction data into nucleation events as a function of temperature, which likely resulted in propagation of the uncertainties in the data, making it difficult to determine the nucleation rate by Apoferritin clusters from that by smaller subforms such as dimers and monomers.

Furthermore, it was possible to obtain distinct nucleation rates for each Apoferritin subform by using the isothermal approach to directly determine the freezing rate from experimental data. In addition, plausible classical nucleation theory parameters were derived for clusters, dimers, and monomers.

Nonetheless, droplet volume, contact angle between the droplet and substrate, and the cooling rate of droplets may restrict the accuracy of the measured isothermal freezing rate of droplets, particularly for larger droplet sizes. Simulations using a finite element method showed that the inner temperature of a droplet is not uniform and requires a longer time to reach the programmed temperature when any or all of the aforementioned factors are increased, resulting in a freezing rate that increases over time or slowly increases with decreasing temperatures. As a result, it is critical to optimise these parameters prior to any isothermal measurements. For example, it is interesting to compare the effect of protein concentration in droplets of different volumes to study whether the protein is adsorbed at the droplet interfaces (i.e. water/air or water/solid interfaces). The size of the droplets to be compared should be small rather than large to minimise the effect of inner temperature gradients. Alternatively, if the droplets must be large, it is preferable to work with small contact angle droplets or to use a slow cooling rate to cool the droplet to the programmed temperature in order to maintain a uniform inner temperature. In light of these conditions, it is recommended that additional research be conducted to investigate the role of droplet interfaces in the ice nucleation process induced by proteins or surfactants, which will enhance our understanding of the working mechanism of biomolecular ice nucleating agents in immersed freezing using isothermal measurements to facilitate comparisons of freezing rates.

Finally, the ice nucleation efficiency of DNA origami tiles was investigated using constant cooling rate and isothermal measurements, and its classical nucleation theory parameters were compared to those of Apoferritin monomers. DNA origami is an intriguing biomolecule ice nucleating agent, and further research should be conducted on the DNA origami ice nucleation process. For instance, synthesize an ice nucleating particle with specified geometrical features that are nanoscale in size, as well as with great reproducibility and purity, in contrast to proteins, which have limited range of forms and a higher tendency to aggregate. In addition, the surface chemistry of DNA origami can be chemically functionalized, which is an interesting property that enables a deeper understanding of the ice bonding process at the surface of the ice nucleating agent. In summary, DNA origami provides a novel model for investigating the heterogeneous ice nucleation process.

APPENDIX A

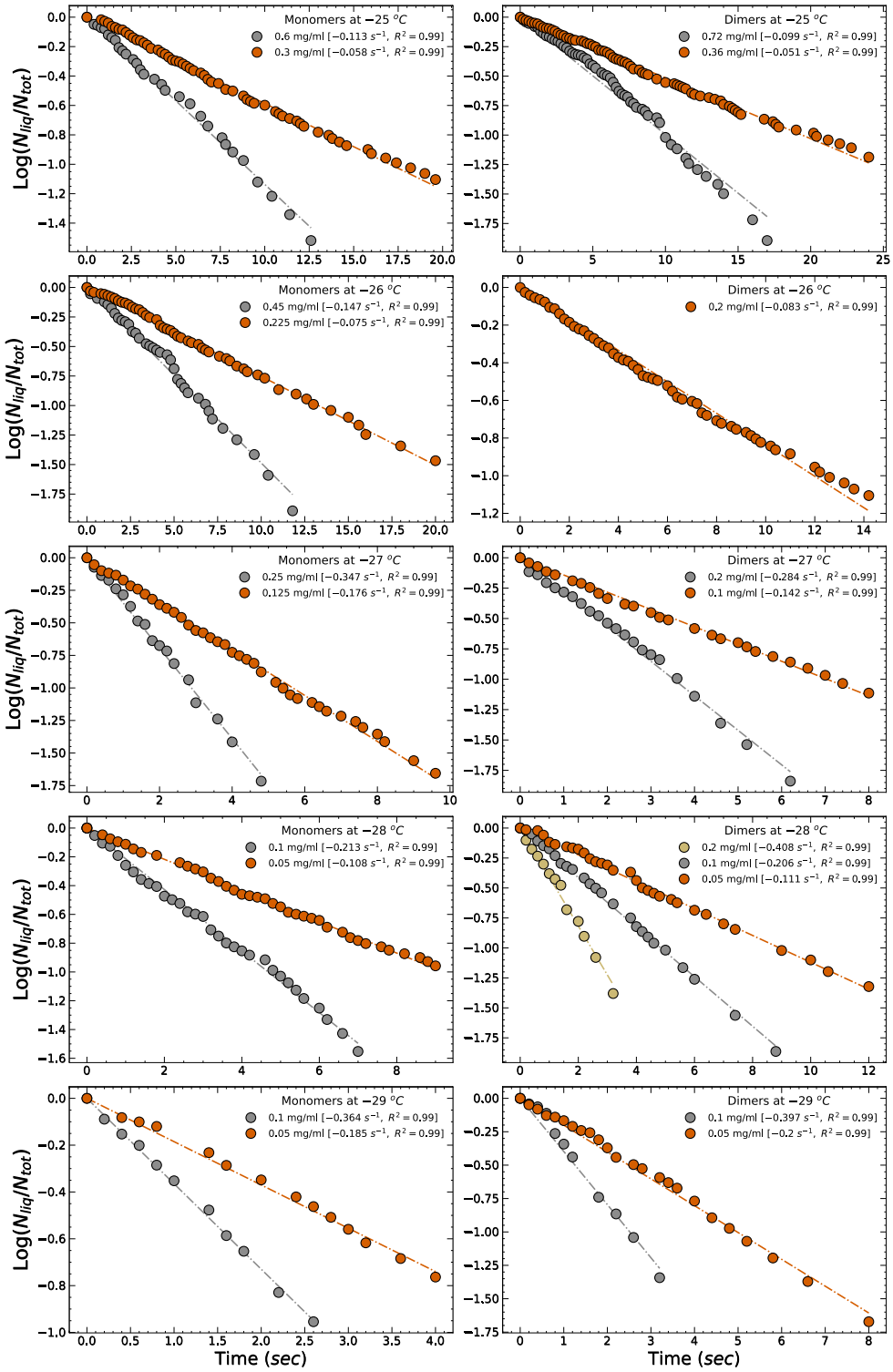

Figure A-1: Apoferritin monomers/cluster and dimers/cluster data for 2µl droplets used in figure (3-12) to represent the clusters (in green). The slopes and goodness of fit are shown in the legends.

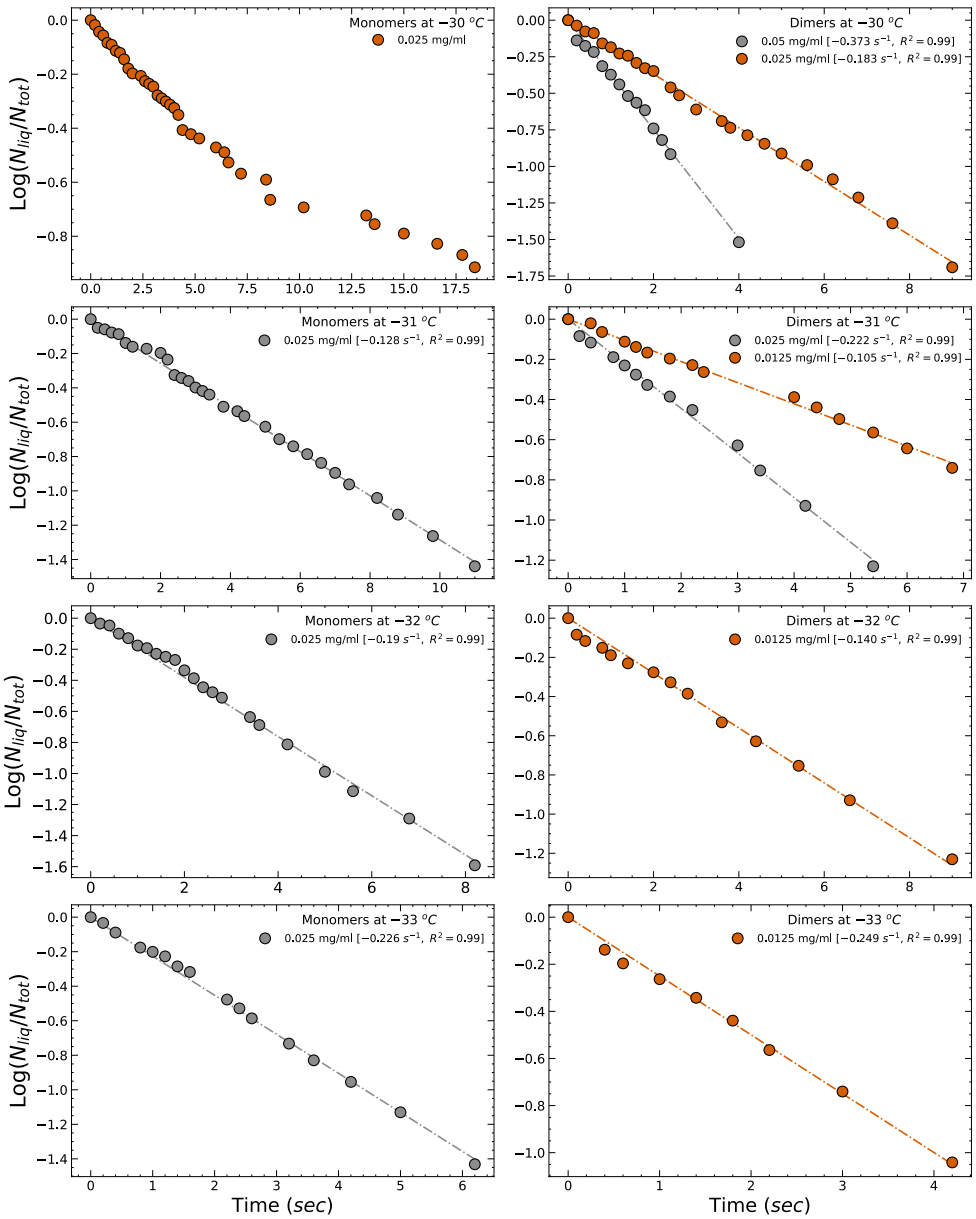

Figure A-2: Apoferritin monomers and dimers data for 2µl droplets, only linear log ($\frac{N_{liq}}{N_{tot}}$) were considered in figure (3-12). The slopes and goodness of fit are given in the legends.

APPENDIX B

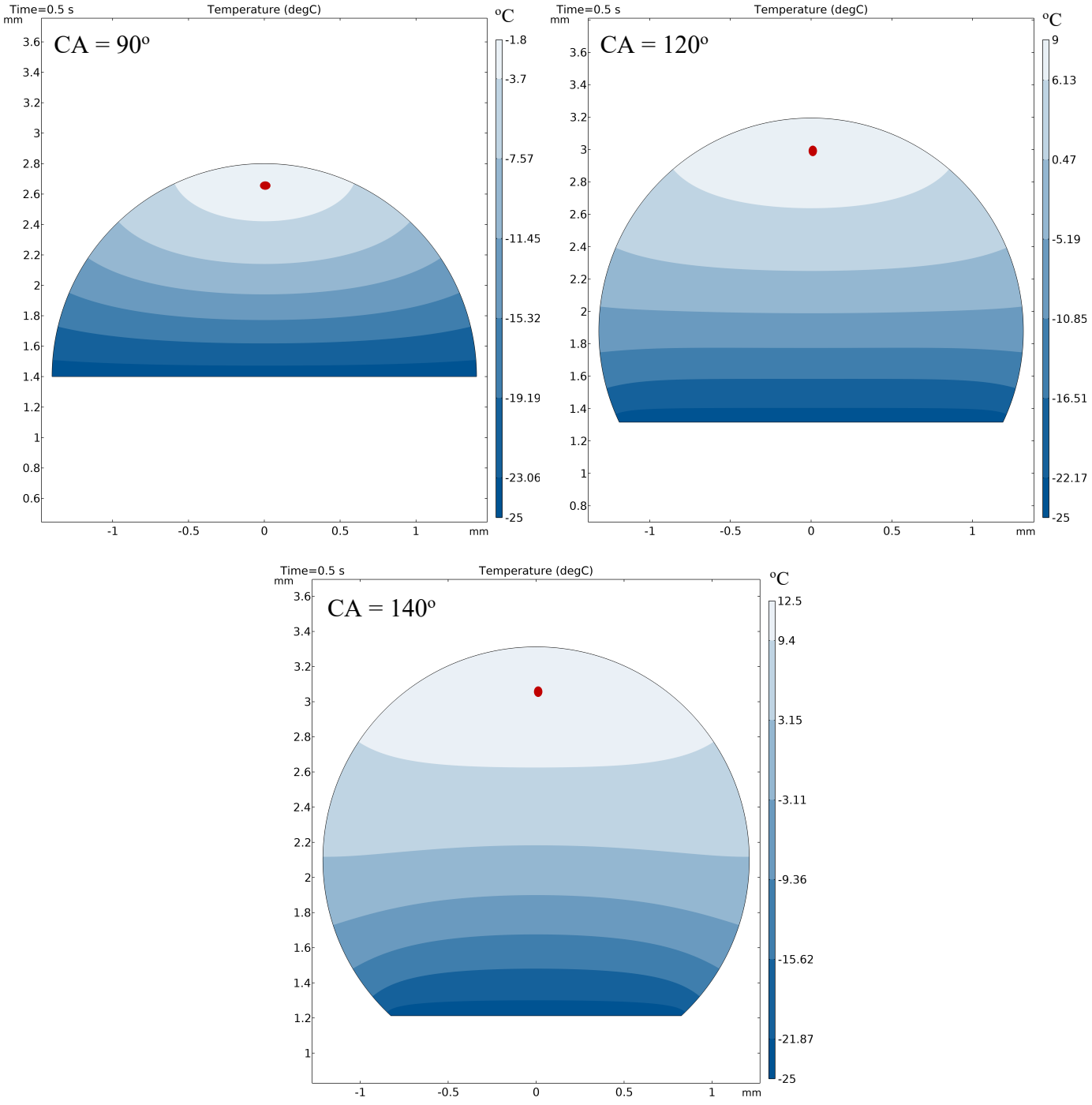

Figure B-1: Simulation of the temperature profile inside a droplet of 8µl size at a temperature of –25 °C and contact angles of 90, 120, and 140 °, respectively at t = 0.5 seconds.

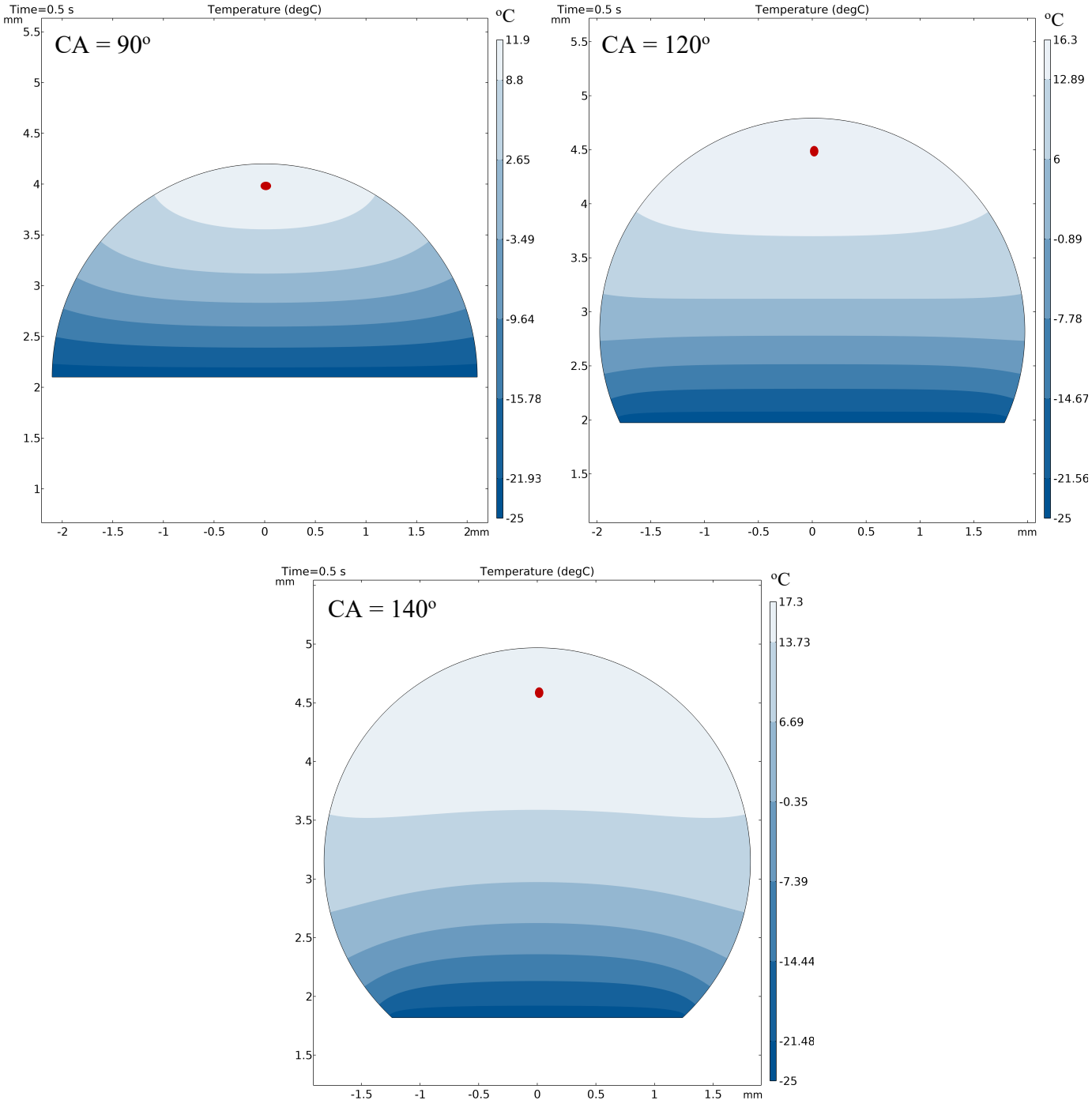

Figure B-2: Simulation of the temperature profile inside a droplet of 27µl size at a temperature of –25 ºC and contact angles of 90, 120, and 140 º, respectively at t = 0.5 seconds.

BIBLIOGRAPHY

[1] N. Maeda, Brief overview of ice nucleation, Molecules. 26 (2021). https://doi.org/10.3390/molecules26020392.

[2] S. Gai, Z. Peng, B. Moghtaderi, J. Yu, E. Doroodchi, Ice nucleation of water droplet containing solid particles under weak ultrasonic vibration, Ultrason. Sonochem. 70 (2021) 105301. https://doi.org/10.1016/j.ultsonch.2020.105301.

[3] Y. Zhao, Q. Guo, T. Lin, P. Cheng, A review of recent literature on icing phenomena: Transport mechanisms, their modulations and controls, Int. J. Heat Mass Transf. 159 (2020). https://doi.org/10.1016/j.ijheatmasstransfer.2020.120074.

[4] M. Yamazaki, A. Jemcov, H. Sakaue, A review on the current status of icing physics and mitigation in aviation, Aerospace. 8 (2021). https://doi.org/10.3390/aerospace8070188.

[5] Z.A. Kanji, L.A. Ladino, H. Wex, Y. Boose, M. Burkert-Kohn, D.J. Cziczo, M. Krämer, Overview of Ice Nucleating Particles, Meteorol. Monogr. 58 (2017) 1.1-1.33. https://doi.org/10.1175/AMSMONOGRAPHS-D-16-0006.1.

[6] M.O. Andreae, D. Rosenfeld, Aerosol-cloud-precipitation interactions. Part 1. The nature and sources of cloud-active aerosols, Earth-Science Rev. 89 (2008) 13–41. https://doi.org/10.1016/j.earscirev.2008.03.001.

[7] C. Hoose, O. Möhler, Heterogeneous ice nucleation on atmospheric aerosols: A review of results from laboratory experiments, Atmos. Chem. Phys. 12 (2012) 9817–9854. https://doi.org/10.5194/acp-12-9817-2012.

[8] B.J. Murray, D. O 'sullivan, J.D. Atkinson, M.E. Webb, Ice nucleation by particles immersed in supercooled cloud dropletsw, Chem. Soc. Rev. Chem. Soc. Rev. 41 (2012) 6519–6554. https://doi.org/10.1039/c2cs35200a.

[9] I. Coluzza, J. Creamean, M.J. Rossi, H. Wex, P.A. Alpert, V. Bianco, Y. Boose, C. Dellago, L. Felgitsch, J. Fröhlich-Nowoisky, H. Herrmann, S. Jungblut, Z.A. Kanji, G. Menzl, B. Moffett, C. Moritz, A. Mutzel, U. Pöschl, M. Schauperl, J. Scheel, E.

Stopelli, F. Stratmann, H. Grothe, D.G. Schmale, Perspectives on the future of ice nucleation research: Research needs and Unanswered questions identified from two international workshops, Atmosphere (Basel). 8 (2017). https://doi.org/10.3390/atmos8080138.

[10] O.B. France, C.G. France, C.H. Germany, A.J. Uk, Clouds and aerosols, Clim. Chang. 2013 Phys. Sci. Basis Work. Gr. I Contrib. to Fifth Assess. Rep. Intergov. Panel Clim. Chang. 9781107057 (2013) 571–658. https://doi.org/10.1017/CBO9781107415324.016.

[11] D.A. Knopf, P.A. Alpert, B. Wang, The Role of Organic Aerosol in Atmospheric Ice Nucleation: A Review, ACS Earth Sp. Chem. 2 (2018) 168–202. https://doi.org/10.1021/acsearthspacechem.7b00120.

[12] S. Huang, W. Hu, J. Chen, Z. Wu, D. Zhang, P. Fu, Overview of biological ice nucleating particles in the atmosphere, Environ. Int. 146 (2021) 106197. https://doi.org/10.1016/j.envint.2020.106197.

[13] P.J. Demott, A.J. Prenni, G.R. McMeeking, R.C. Sullivan, M.D. Petters, Y. Tobo, M. Niemand, O. Möhler, J.R. Snider, Z. Wang, S.M. Kreidenweis, Integrating laboratory and field data to quantify the immersion freezing ice nucleation activity of mineral dust particles, Atmos. Chem. Phys. 15 (2015) 393–409. https://doi.org/10.5194/acp-15-393-2015.

[14] L. Kaufmann, C. Marcolli, J. Hofer, V. Pinti, C.R. Hoyle, T. Peter, Ice nucleation efficiency of natural dust samples in the immersion mode, Atmos. Chem. Phys. 16 (2016) 11177–11206. https://doi.org/10.5194/acp-16-11177-2016.

[15] C.M. Archuleta, P.J. DeMott, S.M. Kreidenweis, Ice nucleation by surrogates for atmospheric mineral dust and mineral dust/sulfate particles at cirrus temperatures, Atmos. Chem. Phys. 5 (2005) 2617–2634. https://doi.org/10.5194/acp-5-2617-2005.

[16] D.A. Knopf, T. Koop, Heterogeneous nucleation of ice on surrogates of mineral dust, J. Geophys. Res. Atmos. 111 (2006) 1–10. https://doi.org/10.1029/2005JD006894.

[17] J.D. Atkinson, B.J. Murray, M.T. Woodhouse, T.F. Whale, K.J. Baustian, K.S. Carslaw, S. Dobbie, D. O'Sullivan, T.L. Malkin, The importance of feldspar for ice

nucleation by mineral dust in mixed-phase clouds, Nature. 498 (2013) 355–358. https://doi.org/10.1038/nature12278.

[18] T. Zolles, J. Burkart, T. Häusler, B. Pummer, R. Hitzenberger, H. Grothe, Identification of ice nucleation active sites on feldspar dust particles, J. Phys. Chem. A. 119 (2015) 2692–2700. https://doi.org/10.1021/jp509839x.

[19] D. O'Sullivan, B.J. Murray, J.F. Ross, M.E. Webb, The adsorption of fungal ice-nucleating proteins on mineral dusts: A terrestrial reservoir of atmospheric ice-nucleating particles, Atmos. Chem. Phys. 16 (2016) 7879–7887. https://doi.org/10.5194/acp-16-7879-2016.

[20] M. Chatziparaschos, N. Daskalakis, S. Myriokefalitakis, N. Kalivitis, A. Nenes, M. Goncalves Ageitos, M. Costa-Suros, C. Perez Garcia-Pando, M. Zanoli, M. Vrekoussis, M. Kanakidou, Role of K-feldspar and quartz in global ice nucleation by mineral dust in mixed-phase clouds, Atmos. Chem. Phys. 23 (2023) 1785–1801. https://doi.org/10.5194/acp-23-1785-2023.

[21] Q. Chen, Y. Yin, H. Jiang, Z. Chu, L. Xue, R. Shi, X. Zhang, J. Chen, The Roles of Mineral Dust as Cloud Condensation Nuclei and Ice Nuclei During the Evolution of a Hail Storm, J. Geophys. Res. Atmos. 124 (2019) 14262–14284. https://doi.org/10.1029/2019JD031403.

[22] C. Marcolli, B. Nagare, A. Welti, U. Lohmann, Ice nucleation efficiency of AgI: Review and new insights, Atmos. Chem. Phys. 16 (2016) 8915–8937. https://doi.org/10.5194/acp-16-8915-2016.

[23] G. Roudsari, O.H. Pakarinen, B. Reischl, H. Vehkamäki, Atomistic and coarse-grained simulations reveal increased ice nucleation activity on silver iodide surfaces in slit and wedge geometries, Atmos. Chem. Phys. 22 (2022) 10099–10114. https://doi.org/10.5194/acp-22-10099-2022.

[24] G. Bai, D. Gao, Z. Liu, X. Zhou, J. Wang, Probing the critical nucleus size for ice formation with graphene oxide nanosheets, Nature. 576 (2019) 437–441. https://doi.org/10.1038/s41586-019-1827-6.

[25] C. Zhang, Y. Wang, J. Wang, X. Zhou, Size of Nanoscale Domains in Inhomogeneous

Surfaces Determines Ice Nucleation, J. Phys. Chem. C. 126 (2022) 13373–13380. https://doi.org/10.1021/acs.jpcc.2c02647.

[26] T. Häusler, P. Gebhardt, D. Iglesias, C. Rameshan, S. Marchesan, D. Eder, H. Grothe, Ice Nucleation Activity of Graphene and Graphene Oxides, J. Phys. Chem. C. 122 (2018) 8182–8190. https://doi.org/10.1021/acs.jpcc.7b10675.

[27] A.K. Metya, J.K. Singh, Ice Nucleation on a Graphite Surface in the Presence of Nanoparticles, J. Phys. Chem. C. 122 (2018) 19056–19066. https://doi.org/10.1021/acs.jpcc.8b05989.

[28] C.I. Biggs, C. Packer, S. Hindmarsh, M. Walker, N.R. Wilson, J.P. Rourke, M.I. Gibson, Impact of sequential surface-modification of graphene oxide on ice nucleation, Phys. Chem. Chem. Phys. 19 (2017) 21929–21932. https://doi.org/10.1039/c7cp03219f.

[29] M. Joghataei, F. Ostovari, S. Atabakhsh, N. Tobeiha, Heterogeneous Ice Nucleation by Graphene Nanoparticles, Sci. Rep. 10 (2020) 1–9. https://doi.org/10.1038/s41598-020-66714-2.

[30] G.P. Schill, M.A. Tolbert, Heterogeneous ice nucleation on simulated sea-spray aerosol using Raman microscopy, J. Phys. Chem. C. 118 (2014) 29234–29241. https://doi.org/10.1021/jp505379j.

[31] M.J. Wolf, A. Coe, L.A. Dove, M.A. Zawadowicz, K. Dooley, S.J. Biller, Y. Zhang, S.W. Chisholm, D.J. Cziczo, Investigating the Heterogeneous Ice Nucleation of Sea Spray Aerosols Using Prochlorococcus as a Model Source of Marine Organic Matter, Environ. Sci. Technol. 53 (2019) 1139–1149. https://doi.org/10.1021/acs.est.8b05150.

[32] M.J. Wolf, M. Goodell, E. Dong, L.A. Dove, C. Zhang, L.J. Franco, C. Shen, E.G. Rutkowski, D.N. Narducci, S. Mullen, A.R. Babbin, D.J. Cziczo, A link between the ice nucleation activity and the biogeochemistry of seawater, Atmos. Chem. Phys. 20 (2020) 15341–15356. https://doi.org/10.5194/acp-20-15341-2020.

[33] R.J. Perkins, M.G. Vazquez De Vasquez, E.E. Beasley, T.C.J. Hill, E.A. Stone, H.C. Allen, P.J. Demott, Relating Structure and Ice Nucleation of Mixed Surfactant Systems Relevant to Sea Spray Aerosol, J. Phys. Chem. A. 124 (2020) 8806–8821.

https://doi.org/10.1021/acs.jpca.0c05849.

[34] B.A. Mitts, X. Wang, D.D. Lucero, C.M. Beall, G.B. Deane, P.J. DeMott, K.A. Prather, Importance of Supermicron Ice Nucleating Particles in Nascent Sea Spray, Geophys. Res. Lett. 48 (2021) 1–10. https://doi.org/10.1029/2020GL089633.

[35] R. Wagner, J. Kaufmann, O. Möhler, H. Saathoff, M. Schnaiter, R. Ullrich, T. Leisner, Heterogeneous Ice Nucleation Ability of NaCl and Sea Salt Aerosol Particles at Cirrus Temperatures, J. Geophys. Res. Atmos. 123 (2018) 2841–2860. https://doi.org/10.1002/2017JD027864.

[36] E.K. Wilbourn, D.C.O. Thornton, C. Ott, J. Graff, P.K. Quinn, T.S. Bates, R. Betha, L.M. Russell, M.J. Behrenfeld, S.D. Brooks, Ice Nucleation by Marine Aerosols Over the North Atlantic Ocean in Late Spring, J. Geophys. Res. Atmos. 125 (2020) 1–17. https://doi.org/10.1029/2019JD030913.

[37] P.A. Alpert, W.P. Kilthau, R.E. O'Brien, R.C. Moffet, M.K. Gilles, B. Wang, A. Laskin, J.Y. Aller, D.A. Knopf, Ice-nucleating agents in sea spray aerosol identified and quantified with a holistic multimodal freezing model, Sci. Adv. 8 (2022) 1–12. https://doi.org/10.1126/sciadv.abq6842.

[38] M. Dymarska, B.J. Murray, L. Sun, M.L. Eastwood, D.A. Knopf, A.K. Bertram, Deposition ice nucleation on soot at temperatures relevant for the lower troposphere, J. Geophys. Res. Atmos. 111 (2006) 1–9. https://doi.org/10.1029/2005JD006627.

[39] O. Möhler, S. Büttner, C. Linke, M. Schnaiter, H. Saathoff, O. Stetzer, R. Wagner, M. Krämer, A. Mangold, V. Ebert, U. Schurath, Effect of sulfuric acid coating on heterogeneous ice nucleation by soot aerosol particles, J. Geophys. Res. D Atmos. 110 (2005) 1–12. https://doi.org/10.1029/2004JD005169.

[40] F. Mahrt, K. Kilchhofer, C. Marcolli, P. Grönquist, R.O. David, M. Rösch, U. Lohmann, Z.A. Kanji, The Impact of Cloud Processing on the Ice Nucleation Abilities of Soot Particles at Cirrus Temperatures, J. Geophys. Res. Atmos. 125 (2020) 1–23. https://doi.org/10.1029/2019JD030922.

[41] K. Gao, Z.A. Kanji, Impacts of Simulated Contrail Processing and Organic Content Change on the Ice Nucleation of Soot Particles, Geophys. Res. Lett. 49 (2022).

https://doi.org/10.1029/2022GL099869.

[42] F. Mahrt, C. Marcolli, R.O. David, P. Grönquist, E.J. Barthazy Meier, U. Lohmann, Z.A. Kanji, Ice nucleation abilities of soot particles determined with the Horizontal Ice Nucleation Chamber, Atmos. Chem. Phys. 18 (2018) 13363–13392. https://doi.org/10.5194/acp-18-13363-2018.

[43] R. Iannone, D.I. Chernoff, A. Pringle, S.T. Martin, A.K. Bertram, The ice nucleation ability of one of the most abundant types of fungal spores found in the atmosphere, Atmos. Chem. Phys. 11 (2011) 1191–1201. https://doi.org/10.5194/acp-11-1191-2011.

[44] C.E. Morris, D.C. Sands, C. Glaux, J. Samsatly, S. Asaad, A.R. Moukahel, F.L.T. Gonçalves, E.K. Bigg, Urediospores of rust fungi are ice nucleation active at >-10 °c and harbor ice nucleation active bacteria, Atmos. Chem. Phys. 13 (2013) 4223–4233. https://doi.org/10.5194/acp-13-4223-2013.

[45] B.G. Pummer, L. Atanasova, H. Bauer, J. Bernardi, I.S. Druzhinina, J. Fröhlich-Nowoisky, H. Grothe, Spores of many common airborne fungi reveal no ice nucleation activity in oil immersion freezing experiments, Biogeosciences. 10 (2013) 8083–8091. https://doi.org/10.5194/bg-10-8083-2013.

[46] D.I. Haga, S.M. Burrows, R. Iannone, M.J. Wheeler, R.H. Mason, J. Chen, E.A. Polishchuk, U. Pöschl, A.K. Bertram, Ice nucleation by fungal spores from the classes agaricomycetes, ustilaginomycetes, and eurotiomycetes, and the effect on the atmospheric transport of these spores, Atmos. Chem. Phys. 14 (2014) 8611–8630. https://doi.org/10.5194/acp-14-8611-2014.

[47] J. Fröhlich-Nowoisky, T.C.J. Hill, B.G. Pummer, P. Yordanova, G.D. Franc, U. Pöschl, Ice nucleation activity in the widespread soil fungus Mortierella alpina, Biogeosciences. 12 (2015) 1057–1071. https://doi.org/10.5194/bg-12-1057-2015.

[48] D. O'Sullivan, B.J. Murray, J.F. Ross, T.F. Whale, H.C. Price, J.D. Atkinson, N.S. Umo, M.E. Webb, The relevance of nanoscale biological fragments for ice nucleation in clouds, Sci. Rep. 5 (2015) 1–7. https://doi.org/10.1038/srep08082.

[49] M. Hummel, C. Hoose, B. Pummer, C. Schaupp, J. Fröhlich-Nowoisky, O. Möhler, Simulating the influence of primary biological aerosol particles on clouds by

heterogeneous ice nucleation, Atmos. Chem. Phys. 18 (2018) 15437–15450. https://doi.org/10.5194/acp-18-15437-2018.

[50] C.F. Weber, Polytrichum commune spores nucleate ice and associated microorganisms increase the temperature of ice nucleation activity onset, Aerobiologia (Bologna). 32 (2016) 353–361. https://doi.org/10.1007/s10453-015-9395-1.

[51] K. Diehl, C. Quick, S. Matthias-Maser, S.K. Mitra, R. Jaenicke, The ice nucleating ability of pollen Part I: Laboratory studies in deposition and condensation freezing modes, Atmos. Res. 58 (2001) 75–87. https://doi.org/10.1016/S0169-8095(01)00091-6.

[52] K. Diehl, S. Matthias-Maser, R. Jaenicke, S.K. Mitra, The ice nucleating ability of pollen: Part II. Laboratory studies in immersion and contact freezing modes, Atmos. Res. 61 (2002) 125–133. https://doi.org/10.1016/S0169-8095(01)00132-6.

[53] N. von Blohn, S.K. Mitra, K. Diehl, S. Borrmann, The ice nucleating ability of pollen: Part III: New laboratory studies in immersion and contact freezing modes including more pollen types, Atmos. Res. 78 (2005) 182–189. https://doi.org/10.1016/j.atmosres.2005.03.008.

[54] B.G. Pummer, H. Bauer, J. Bernardi, S. Bleicher, H. Grothe, Suspendable macromolecules are responsible for ice nucleation activity of birch and conifer pollen, Atmos. Chem. Phys. 12 (2012) 2541–2550. https://doi.org/10.5194/acp-12-2541-2012.

[55] K. Dreischmeier, C. Budke, L. Wiehemeier, T. Kottke, T. Koop, Boreal pollen contain ice-nucleating as well as ice-binding “antifreeze” polysaccharides, (2017). https://doi.org/10.1038/srep41890.

[56] K.A. Murray, N.L.H. Kinney, C.A. Griffiths, M. Hasan, M.I. Gibson, T.F. Whale, Pollen derived macromolecules serve as a new class of ice-nucleating cryoprotectants, Sci. Rep. 12 (2022) 1–11. https://doi.org/10.1038/s41598-022-15545-4.

[57] B.H. Matthews, A.N. Alsante, S.D. Brooks, Pollen Emissions of Subpollen Particles and Ice Nucleating Particles, ACS Earth Sp. Chem. (2023). https://doi.org/10.1021/acsearthspacechem.3c00014.

[58] L. Eickhoff, K. Dreischmeier, A. Zipori, V. Sirotinskaya, C. Adar, N. Reicher, I. Braslavsky, Y. Rudich, T. Koop, Contrasting Behavior of Antifreeze Proteins: Ice Growth Inhibitors and Ice Nucleation Promoters, J. Phys. Chem. Lett. 10 (2019) 966–972. https://doi.org/10.1021/acs.jpclett.8b03719.

[59] J.H. Wang, A comprehensive evaluation of the effects and mechanisms of antifreeze proteins during low-temperature preservation, Cryobiology. 41 (2000) 1–9. https://doi.org/10.1006/cryo.2000.2265.

[60] K.E. Zachariassen, E. Kristiansen, Ice Nucleation and Antinucleation in Nature, Cryobiology. 41 (2000) 257–279. https://doi.org/10.1006/cryo.2000.2289.

[61] J.G. Duman, Animal ice-binding (antifreeze) proteins and glycolipids: An overview with emphasis on physiological function, J. Exp. Biol. 218 (2015) 1846–1855. https://doi.org/10.1242/jeb.116905.

[62] P.W. Wilson, K.E. Osterday, A.F. Heneghan, A.D.J. Haymet, Type I antifreeze proteins enhance ice nucleation above certain concentrations, J. Biol. Chem. 285 (2010) 34741–34745. https://doi.org/10.1074/jbc.M110.171983.

[63] A. Hudait, N. Odendahl, Y. Qiu, F. Paesani, V. Molinero, Ice-Nucleating and Antifreeze Proteins Recognize Ice through a Diversity of Anchored Clathrate and Ice-like Motifs, J. Am. Chem. Soc. 140 (2018) 4905–4912. https://doi.org/10.1021/jacs.8b01246.

[64] K. Liu, C. Wang, J. Ma, G. Shi, X. Yao, H. Fang, Y. Song, J. Wang, Janus effect of antifreeze proteins on ice nucleation, Proc. Natl. Acad. Sci. U. S. A. 113 (2016) 14739–14744. https://doi.org/10.1073/pnas.1614379114.

[65] L.R. Maki, E.L. Galyan, M.M. Chang-Chien, D.R. Caldwell, Ice nucleation induced by pseudomonas syringae., Appl. Microbiol. 28 (1974) 456–459. https://doi.org/10.1128/aem.28.3.456-459.1974.

[66] N. Cochet, P. Widehem, Ice crystallization by Pseudomonas syringae, Appl. Microbiol. Biotechnol. 54 (2000) 153–161. https://doi.org/10.1007/s002530000377.

[67] P. Amato, M. Joly, C. Schaupp, E. Attard, O. Möhler, C.E. Morris, Y. Brunet, A.M.

Delort, Survival and ice nucleation activity of bacteria as aerosols in a cloud simulation chamber, Atmos. Chem. Phys. 15 (2015) 6455–6465. https://doi.org/10.5194/acp-15-6455-2015.

[68] R.B. Pietsch, B.A. Vinatzer, D.G. Schmale, Diversity and abundance of ice nucleating strains of Pseudomonas syringae in a Freshwater Lake in Virginia, USA, Front. Microbiol. 8 (2017) 1–11. https://doi.org/10.3389/fmicb.2017.00318.

[69] K.C. Failor, D.G. Schmale, B.A. Vinatzer, C.L. Monteil, Ice nucleation active bacteria in precipitation are genetically diverse and nucleate ice by employing different mechanisms, ISME J. 11 (2017) 2740–2753. https://doi.org/10.1038/ismej.2017.124.

[70] Y.J. Han, H.J. Song, C.W. Lee, N.H. Ly, S.W. Joo, J.H. Lee, S.J. Kim, S.Y. Park, Biophysical characterization of soluble Pseudomonas syringae ice nucleation protein InaZ fragments, Int. J. Biol. Macromol. 94 (2017) 634–641. https://doi.org/10.1016/j.ijbiomac.2016.10.062.

[71] M.L. Ling, H. Wex, S. Grawe, J. Jakobsson, J. Löndahl, S. Hartmann, K. Finster, T. Boesen, T. Šantl-Temkiv, Effects of Ice Nucleation Protein Repeat Number and Oligomerization Level on Ice Nucleation Activity, J. Geophys. Res. Atmos. (2018). https://doi.org/10.1002/2017JD027307.

[72] M.L. Ling, I.P.G. Marshall, B. Rosati, L. Schreiber, T. Boesen, K. Finster, T. Šantl-Temkiv, Properties relevant to atmospheric dispersal of the ice-nucleation active Pseudomonas syringae strain R10.79 isolated from rain water, Aerobiologia (Bologna). 37 (2021) 225–241. https://doi.org/10.1007/s10453-020-09682-4.

[73] R. Schwidetzky, M. Lukas, A. YazdanYar, A.T. Kunert, U. Pöschl, K.F. Domke, J. Fröhlich-Nowoisky, M. Bonn, T. Koop, Y. Nagata, K. Meister, Specific Ion–Protein Interactions Influence Bacterial Ice Nucleation, Chem. - A Eur. J. 27 (2021) 7402–7407. https://doi.org/10.1002/chem.202004630.

[74] R. Pandey, K. Usui, R.A. Livingstone, S.A. Fischer, J. Pfaendtner, E.H.G. Backus, Y. Nagata, J. Fröhlich-Nowoisky, L. Schmüser, S. Mauri, J.F. Scheel, D.A. Knopf, U. Pöschl, M. Bonn, T. Weidner, Ice-nucleating bacteria control the order and dynamics of interfacial water, Sci. Adv. 2 (2016) 1–9. https://doi.org/10.1126/sciadv.1501630.

[75] S.J. Roeters, T.W. Golbek, M. Bregnhøj, T. Drace, S. Alamdari, W. Roseboom, G. Kramer, T. Šantl-Temkiv, K. Finster, J. Pfaendtner, S. Woutersen, T. Boesen, T. Weidner, Ice-nucleating proteins are activated by low temperatures to control the structure of interfacial water, Nat. Commun. 12 (2021) 1–9. https://doi.org/10.1038/s41467-021-21349-3.

[76] D.G. Georgakopoulos, Biological ice nucleators in snow samples from Greece, Atmosphere (Basel). 12 (2021). https://doi.org/10.3390/atmos12111461.

[77] M.P. Adams, N.S. Atanasova, S. Sofieva, J. Ravantti, A. Heikkinen, Z. Brasseur, J. Duplissy, D.H. Bamford, B.J. Murray, Ice nucleation by viruses and their potential for cloud glaciation, Biogeosciences. 18 (2021) 4431–4444. https://doi.org/10.5194/bg-18-4431-2021.

[78] M.I. Daily, M.D. Tarn, T.F. Whale, B.J. Murray, An evaluation of the heat test for the ice-nucleating ability of minerals and biological material, Atmos. Meas. Tech. 15 (2022) 2635–2665. https://doi.org/10.5194/amt-15-2635-2022.

[79] A. Rocchi, A. Sotomayor-Garcia, M. Cabrera-Brufau, E. Berdalet, M. Dall'Osto, D. Vaqué, Abundance and activity of sympagic viruses near the Western Antarctic Peninsula, Polar Biol. 45 (2022) 1363–1378. https://doi.org/10.1007/s00300-022-03073-w.

[80] M.A. Holden, J.M. Campbell, F.C. Meldrum, B.J. Murray, H.K. Christenson, Active sites for ice nucleation differ depending on nucleation mode, Proc. Natl. Acad. Sci. U. S. A. 118 (2021) 1–9. https://doi.org/10.1073/pnas.2022859118.

[81] G.C. Sosso, T.F. Whale, M.A. Holden, P. Pedevilla, B.J. Murray, A. Michaelides, Unravelling the origins of ice nucleation on organic crystals, Chem. Sci. 9 (2018) 8077–8088. https://doi.org/10.1039/c8sc02753f.

[82] N.B. Magee, A. Miller, M. Amaral, A. Cumiskey, Mesoscopic surface roughness of ice crystals pervasive across a wide range of ice crystal conditions, Atmos. Chem. Phys. 14 (2014) 12357–12371. https://doi.org/10.5194/acp-14-12357-2014.

[83] G. Bakradze, K. Morgenstern, Temperature-dependent Shape Changes of Ice Nanoclusters on Ag(100), ChemPhysChem. 19 (2018) 2858–2862.

https://doi.org/10.1002/cphc.201800696.

[84] G.C. Sosso, P. Sudera, A.T. Backes, T.F. Whale, J. Fröhlich-Nowoisky, M. Bonn, A. Michaelides, E.H.G. Backus, The role of structural order in heterogeneous ice nucleation, Chem. Sci. 13 (2022) 5014–5026. https://doi.org/10.1039/d1sc06338c.

[85] H. Memon, J. Wang, X. Hou, Interdependence of Surface Roughness on Icephobic Performance: A Review, Materials (Basel). 16 (2023) 4607. https://doi.org/10.3390/ma16134607.

[86] X. Wu, V. V. Silberschmidt, Z.T. Hu, Z. Chen, When superhydrophobic coatings are icephobic: Role of surface topology, Surf. Coatings Technol. 358 (2019) 207–214. https://doi.org/10.1016/j.surfcoat.2018.11.039.

[87] T. Khaleque, S. Goel, Repurposing superhydrophobic surfaces into icephobic surfaces, Mater. Today Proc. 64 (2022) 1526–1532. https://doi.org/10.1016/j.matpr.2022.05.585.

[88] M. Ganguly, S. Dib, P.A. Ariya, Purely Inorganic Highly Efficient Ice Nucleating Particle, ACS Omega. 3 (2018) 3384–3395. https://doi.org/10.1021/acsomega.7b01830.

[89] R.W. Saunders, O. Möhler, M. Schnaiter, S. Benz, R. Wagner, H. Saathoff, P.J. Connolly, R. Burgess, B.J. Murray, M. Gallagher, R. Wills, J.M.C. Plane, An aerosol chamber investigation of the heterogeneous ice nucleating potential of refractory nanoparticles, Atmos. Chem. Phys. 10 (2010) 1227–1247. https://doi.org/10.5194/acp-10-1227-2010.

[90] K. Tai, Y. Liu, S.J. Dillon, In situ cryogenic transmission electron microscopy for characterizing the evolution of solidifying water ice in colloidal systems, Microsc. Microanal. 20 (2014) 330–337. https://doi.org/10.1017/S1431927613014128.

[91] J. Nehete, R. Bhambar, M. Narkhede, S. Gawali, Natural proteins: Sources, isolation, characterization and applications, Pharmacogn. Rev. 7 (2013) 107–116. https://doi.org/10.4103/0973-7847.120508.

[92] K.E. Sapsford, K.M. Tyner, B.J. Dair, J.R. Deschamps, I.L. Medintz, Analyzing

nanomaterial bioconjugates: A review of current and emerging purification and characterization techniques, Anal. Chem. 83 (2011) 4453–4488. https://doi.org/10.1021/ac200853a.

[93] P.K. Sorger, H.R. Pelham, Purification and characterization of a heat-shock element binding protein from yeast., EMBO J. 6 (1987) 3035–3041. https://doi.org/10.1002/j.1460-2075.1987.tb02609.x.

[94] K. Nagaraju, R. Reddy, N. Reddy, A review on protein functionalized carbon nanotubes, J. Appl. Biomater. Funct. Mater. 13 (2015) e301–e312. https://doi.org/10.5301/jabfm.5000231.

[95] R. Cagliani, F. Gatto, G. Bardi, Protein adsorption: A feasible method for nanoparticle functionalization?, Materials (Basel). 12 (2019) 1–11. https://doi.org/10.3390/ma12121991.

[96] L. Xu, S.L. Kuan, T. Weil, Contemporary Approaches for Site-Selective Dual Functionalization of Proteins, Angew. Chemie - Int. Ed. 60 (2021) 13757–13777. https://doi.org/10.1002/anie.202012034.

[97] M. Cascajo-Castresana, R.O. David, M.A. Iriarte-Alonso, A.M. Bittner, C. Marcolli, Protein aggregates nucleate ice: the example of apoferritin, Atmos. Chem. Phys. 20 (2020) 3291–3315. https://doi.org/10.5194/acp-20-3291-2020.

[98] A.N. Alsante, D.C.O. Thornton, S.D. Brooks, Ice nucleation catalyzed by the photosynthesis enzyme RuBisCO and other abundant biomolecules, Commun. Earth Environ. 4 (2023) 1–9. https://doi.org/10.1038/s43247-023-00707-7.

[99] G.C. Sosso, J. Chen, S.J. Cox, M. Fitzner, P. Pedevilla, A. Zen, A. Michaelides, Crystal Nucleation in Liquids: Open Questions and Future Challenges in Molecular Dynamics Simulations, Chem. Rev. 116 (2016) 7078–7116. https://doi.org/10.1021/acs.chemrev.5b00744.

[100] T.H. Zhang, X.Y. Liu, Experimental modelling of single-particle dynamic processes in crystallization by controlled colloidal assembly, Chem. Soc. Rev. 43 (2014) 2324–2347. https://doi.org/10.1039/c3cs60398a.

[101] Z. Zhang, Y. Liu, Control of ice nucleation: freezing and antifreeze strategies, 7116 | Chem. Soc. Rev. 47 (2018) 7116. https://doi.org/10.1039/c8cs00626a.

[102] A.O. Tipeev, E.D. Zanotto, Nucleation kinetics in supercooled Ni50Ti50: Computer simulation data corroborate the validity of the Classical Nucleation Theory, Chem. Phys. Lett. 735 (2019) 136749. https://doi.org/10.1016/j.cplett.2019.136749.

[103] V.I. Khvorostyanov, J.A. Curry, The theory of ice nucleation by heterogeneous freezing of deliquescent mixed CCN. Part I: Critical radius, energy and nucleation rate, J. Atmos. Sci. 61 (2004) 2676–2691. https://doi.org/10.1175/JAS3266.1.

[104] L. Ickes, A. Welti, C. Hoose, U. Lohmanna, Classical Nucleation Theory of homogeneous freezing of water: Thermodynamic and kinetic parameters, Phys. Chem. Chem. Phys. 17 (2015) 5514–5537. https://doi.org/10.1039/c4cp04184d.

[105] B. Cheng, C. Dellago, M. Ceriotti, Theoretical prediction of the homogeneous ice nucleation rate: Disentangling thermodynamics and kinetics, Phys. Chem. Chem. Phys. 20 (2018) 28732–28740. https://doi.org/10.1039/c8cp04561e.

[106] E. Sanz, C. Vega, J.R. Espinosa, R. Caballero-Bernal, J.L.F. Abascal, C. Valeriani, Homogeneous ice nucleation at moderate supercooling from molecular simulation, J. Am. Chem. Soc. 135 (2013) 15008–15017. https://doi.org/10.1021/ja4028814.

[107] R. Cabriolu, T. Li, Ice nucleation on carbon surface supports the classical theory for heterogeneous nucleation, Phys. Rev. E - Stat. Nonlinear, Soft Matter Phys. 91 (2015) 1–7. https://doi.org/10.1103/PhysRevE.91.052402.

[108] N.H. Fletcher, Size effect in heterogeneous nucleation, J. Chem. Phys. 29 (1958) 572–576. https://doi.org/10.1063/1.1744540.

[109] X.Y. Liu, A new kinetic model for three-dimensional heterogeneous nucleation, J. Chem. Phys. 111 (1999) 1628–1635. https://doi.org/10.1063/1.479391.

[110] X.Y. Liu, N. Du, Zero-sized effect of nano-particles and inverse homogeneous nucleation: Principles of freezing and antifreeze, J. Biol. Chem. 279 (2004) 6124–6131. https://doi.org/10.1074/jbc.M310487200.

[111] G. Vali, P.J. DeMott, O. Möhler, T.F. Whale, Technical Note: A proposal for ice

nucleation terminology, Atmos. Chem. Phys. 15 (2015) 10263–10270. https://doi.org/10.5194/acp-15-10263-2015.

[112] C. Marcolli, F. Mahrt, B. Kärcher, Soot PCF: Pore condensation and freezing framework for soot aggregates, Atmos. Chem. Phys. 21 (2021) 7791–7843. https://doi.org/10.5194/acp-21-7791-2021.

[113] G. Vali, Interpretation of freezing nucleation experiments: singular and stochastic; sites and surfaces, Atmos. Chem. Phys. 14 (2014) 5271–5294. https://doi.org/10.5194/acp-14-5271-2014.

[114] P.J. Connolly, O. Möhler, P.R. Field, H. Saathoff, R. Burgess, T. Choularton, M. Gallagher, Studies of heterogeneous freezing by three different desert dust samples, Atmos. Chem. Phys. 9 (2009) 2805–2824. https://doi.org/10.5194/acp-9-2805-2009.

[115] C. Budke, T. Koop, BINARY: An optical freezing array for assessing temperature and time dependence of heterogeneous ice nucleation, Atmos. Meas. Tech. 8 (2015) 689–703. https://doi.org/10.5194/amt-8-689-2015.

[116] A. Andersson, Mechanisms for log normal concentration distributions in the environment, Sci. Rep. 11 (2021) 1–7. https://doi.org/10.1038/s41598-021-96010-6.

[117] C. Marcolli, S. Gedamke, T. Peter, B. Zobrist, Efficiency of immersion mode ice nucleation on surrogates of mineral dust, Atmos. Chem. Phys. 7 (2007) 5081–5091. https://doi.org/10.5194/acp-7-5081-2007.

[118] E. Pach, A. Verdaguer, Pores Dominate Ice Nucleation on Feldspars, J. Phys. Chem. C. 123 (2019) 20998–21004. https://doi.org/10.1021/acs.jpcc.9b05845.

[119] A. Peckhaus, A. Kiselev, T. Hiron, M. Ebert, T. Leisner, A comparative study of K-rich and Na/Ca-rich feldspar ice-nucleating particles in a nanoliter droplet freezing assay, Atmos. Chem. Phys. 16 (2016) 11477–11496. https://doi.org/10.5194/acp-16-11477-2016.

[120] P.A. Alpert, J.Y. Aller, D.A. Knopf, Ice nucleation from aqueous NaCl droplets with and without marine diatoms, Atmos. Chem. Phys. 11 (2011) 5539–5555. https://doi.org/10.5194/acp-11-5539-2011.

[121] S. Hartmann, M. Ling, L.S.A. Dreyer, A. Zipori, K. Finster, S. Grawe, L.Z. Jensen, S. Borck, N. Reicher, T. Drace, D. Niedermeier, N.C. Jones, S. V. Hoffmann, H. Wex, Y. Rudich, T. Boesen, T. Šantl-Temkiv, Structure and Protein-Protein Interactions of Ice Nucleation Proteins Drive Their Activity, Front. Microbiol. 13 (2022). https://doi.org/10.3389/fmicb.2022.872306.

[122] M. Kim, Y. Rho, K. Sik Jin, B. Ahn, S. Jung, H. Kim, M. Ree, pH-Dependent Structures of Ferritin and Apoferritin in Solution: Disassembly and Reassembly, Biomacromolecules. 12 (2011) 1629–1640. https://doi.org/10.1021/bm200026v.

[123] C.J. Russo, L.A. Passmore, Ultrastable gold substrates for electron cryomicroscopy, Science (80-.). 346 (2014) 1377–1380. https://doi.org/10.1126/science.1259530.

[124] S.H. Choi, K. Choi, I. Chan Kwon, H.J. Ahn, The incorporation of GALA peptide into a protein cage for an acid-inducible molecular switch, Biomaterials. 31 (2010) 5191–5198. https://doi.org/10.1016/j.biomaterials.2010.03.016.

[125] D. Yang, K. Matsubara, M. Yamaki, S. Ebina, K. Nagayama, Heterogeneities in ferritin dimers as characterized by gel filtration, nuclear magnetic resonance, electrophoresis, transmission electron microscopy, and gene engineering techniques, Biochim. Biophys. Acta (BBA)/Protein Struct. Mol. 1206 (1994) 173–179. https://doi.org/10.1016/0167-4838(94)90205-4.

[126] R. Ghirlando, R. Mutskova, C. Schwartz, Enrichment and characterization of ferritin for nanomaterial applications, Nanotechnology. 27 (2015). https://doi.org/10.1088/0957-4484/27/4/045102.

[127] L. Zhang, J.B. Bailey, R.H. Subramanian, F.A. Tezcan, Hyperexpandable, self-healing macromolecular crystals with integrated polymer networks, Nature. 557 (2018) 86–91. https://doi.org/10.1038/s41586-018-0057-7.

[128] Y. Niitsu, I. Listowsky, Mechanisms for the Formation of Ferritin Oligomers, Biochemistry. 12 (1973) 4690–4695. https://doi.org/10.1021/bi00747a023.

[129] B.. Thomas, D. Carter, F. Rosenberger, Effect of microheterogeneity on horse spleen apoferritin crystallization, J. Cryst. Growth. 187 (1998) 499–510. https://doi.org/10.1016/S0022-0248(98)00033-5.

[130] D.N. Petsev, B.R. Thomas, S.T. Yau, P.G. Vekilov, Interactions and aggregation of apoferritin molecules in solution: Effects of added electrolytes, Biophys. J. 78 (2000) 2060–2069. https://doi.org/10.1016/S0006-3495(00)76753-1.

[131] H. Schägger, G. von Jagow, Blue native electrophoresis for isolation of membrane protein complexes in enzymatically active form, Anal. Biochem. 199 (1991) 223–231. https://doi.org/10.1016/0003-2697(91)90094-A.

[132] I. Wittig, H.P. Braun, H. Schägger, Blue native PAGE, Nat. Protoc. 1 (2006) 418–428. https://doi.org/10.1038/nprot.2006.62.

[133] L.G.J. Nijtmans, N.S. Henderson, I.J. Holt, Blue Native electrophoresis to study mitochondrial and other protein complexes, Methods. 26 (2002) 327–334. https://doi.org/10.1016/S1046-2023(02)00038-5.

[134] R. Van Coster, J. Smet, E. George, L. De Meirleir, S. Seneca, J. Van Hove, G. Sebire, H. Verhelst, J. De Bleecker, B. Van Vlem, P. Verloo, J. Leroy, Blue native polyacrylamide gel electrophoresis: A powerful tool in diagnosis of oxidative phosphorylation defects, Pediatr. Res. 50 (2001) 658–665. https://doi.org/10.1203/00006450-200111000-00020.

[135] Z. Emami Bistgani, S.A. Siadat, A. Bakhshandeh, A. Ghasemi Pirbalouti, M. Hashemi, Interactive effects of drought stress and chitosan application on physiological characteristics and essential oil yield of Thymus daenensis Celak, Crop J. 5 (2017) 407–415. https://doi.org/10.1016/j.cj.2017.04.003.

[136] R. Seevaratnam, B.P. Patel, M.J. Hamadeh, Comparison of total protein concentration in skeletal muscle as measured by the Bradford and Lowry assays, J. Biochem. 145 (2009) 791–797. https://doi.org/10.1093/jb/mvp037.

[137] T. Zor, Z. Selinger, Linearization of the Bradford protein assay increases its sensitivity: Theoretical and experimental studies, Anal. Biochem. 236 (1996) 302–308. https://doi.org/10.1006/abio.1996.0171.

[138] V.A. Spencer, J.R. Davie, Isolation of Proteins Cross-linked to DNA by Cisplatin, 2003. https://doi.org/10.1385/1-59259-169-8:747.

[139] M. Kim, Y. Rho, K.S. Jin, B. Ahn, S. Jung, H. Kim, M. Ree, pH-Dependent Structures of Ferritin and Apoferritin in Solution: Disassembly and Reassembly, Biomacromolecules. 12 (2011) 1629–1640. https://doi.org/10.1021/bm200026v.

[140] J.D. Atkinson, B.J. Murray, D. O'Sullivan, Rate of homogenous nucleation of ice in supercooled water, J. Phys. Chem. A. 120 (2016) 6513–6520. https://doi.org/10.1021/acs.jpca.6b03843.

[141] P.A. Alpert, D.A. Knopf, Analysis of isothermal and cooling-rate-dependent immersion freezing by a unifying stochastic ice nucleation model, Atmos. Chem. Phys. 16 (2016) 2083–2107. https://doi.org/10.5194/acp-16-2083-2016.

[142] T.P. Wright, M.D. Petters, The role of time in heterogeneous freezing nucleation, J. Geophys. Res. Atmos. 118 (2013) 3731–3743. https://doi.org/10.1002/jgrd.50365.

[143] J. Chen, Z. Wu, J. Chen, N. Reicher, X. Fang, Y. Rudich, M. Hu, Size-resolved atmospheric ice-nucleating particles during East Asian dust events, Atmos. Chem. Phys. 21 (2021) 3491–3506. https://doi.org/10.5194/acp-21-3491-2021.

[144] E.C. Maters, D.B. Dingwell, C. Cimarelli, D. Müller, T.F. Whale, B.J. Murray, The importance of crystalline phases in ice nucleation by volcanic ash, Atmos. Chem. Phys. 19 (2019) 5451–5465. https://doi.org/10.5194/acp-19-5451-2019.

[145] R.P. Sear, Quantitative studies of crystal nucleation at constant supersaturation: Experimental data and models, CrystEngComm. 16 (2014) 6506–6522. https://doi.org/10.1039/c4ce00344f.

[146] D.A. Knopf, P.A. Alpert, A. Zipori, N. Reicher, Y. Rudich, Stochastic nucleation processes and substrate abundance explain time-dependent freezing in supercooled droplets, Npj Clim. Atmos. Sci. 3 (2020) 1–9. https://doi.org/10.1038/s41612-020-0106-4.

[147] H. Wu, M.H. Engelhard, J. Wang, D.R. Fisher, Y. Lin, Synthesis of lutetium phosphate-apoferritin core-shell nanoparticles for potential applications in radioimmunoimaging and radioimmunotherapy of cancers, J. Mater. Chem. 18 (2008) 1779–1783. https://doi.org/10.1039/b717613a.

[148] L. Zhang, M. Knez, Spherical nanoscale protein templates for biomedical applications: a review on ferritin, J. Nanosci. Lett. 2 (2012).

[149] E. Falvo, E. Tremante, A. Arcovito, M. Papi, N. Elad, A. Boffi, V. Morea, G. Conti, G. Toffoli, G. Fracasso, P. Giacomini, P. Ceci, Improved Doxorubicin Encapsulation and Pharmacokinetics of Ferritin-Fusion Protein Nanocarriers Bearing Proline, Serine, and Alanine Elements, Biomacromolecules. 17 (2016) 514–522. https://doi.org/10.1021/acs.biomac.5b01446.

[150] K. Li, C. Sun, T. Klose, J. Irimia-Dominguez, F.S. Vago, R. Vidal, W. Jiang, Sub-3 Å apoferritin structure determined with full range of phase shifts using a single position of volta phase plate, J. Struct. Biol. 206 (2019) 225–232. https://doi.org/10.1016/j.jsb.2019.03.007.

[151] V. Mitropoulos, A. Mütze, P. Fischer, Mechanical properties of protein adsorption layers at the air/water and oil/water interface: A comparison in light of the thermodynamical stability of proteins, Adv. Colloid Interface Sci. 206 (2014) 195–206. https://doi.org/10.1016/j.cis.2013.11.004.

[152] J. Bergfreund, P. Bertsch, P. Fischer, Adsorption of proteins to fluid interfaces: Role of the hydrophobic subphase, J. Colloid Interface Sci. 584 (2021) 411–417. https://doi.org/10.1016/j.jcis.2020.09.118.

[153] R.A. Latour, Fundamental Principles of the Thermodynamics and Kinetics of Protein Adsorption to Material Surfaces, Colloids Surfaces B Biointerfaces. 191 (2020) 110992. https://doi.org/10.1016/j.colsurfb.2020.110992.

[154] V. Hlady, J. Buijs, H.P. Jennissen, [26] Methods for studying protein adsorption, in: Methods Enzymol., 1999: pp. 402–429. https://doi.org/10.1016/S0076-6879(99)09028-X.

[155] W. Norde, Adsorption of Proteins at Solid-Liquid Interfaces, Cells Mater. 5 (1995) 97–112.

[156] Y. Jia, X.Y. Liu, Self-assembly of protein at aqueous solution surface in correlation to protein crystallization, Appl. Phys. Lett. 86 (2005) 1–4. https://doi.org/10.1063/1.1846153.

[157] L. Martínez-Balbuena, A. Arteaga-Jiménez, E. Hernández-Zapata, C. Márquez-Beltrán, Applicability of the Gibbs Adsorption Isotherm to the analysis of experimental surface-tension data for ionic and nonionic surfactants, Adv. Colloid Interface Sci. 247 (2017) 178–184. https://doi.org/10.1016/j.cis.2017.07.018.

[158] S.Y. Fung, C. Keyes, J. Duhamel, P. Chen, Concentration effect on the aggregation of a self-assembling oligopeptide, Biophys. J. 85 (2003) 537–548. https://doi.org/10.1016/S0006-3495(03)74498-1.

[159] N.M. Persiantseva, O.B. Popovicheva, N.K. Shonija, Wetting and hydration of insoluble soot particles in the upper troposphere, J. Environ. Monit. 6 (2004) 939–945. https://doi.org/10.1039/b407770a.

[160] C. Marcolli, Technical note: Fundamental aspects of ice nucleation via pore condensation and freezing including Laplace pressure and growth into macroscopic ice, Atmos. Chem. Phys. 20 (2020) 3209–3230. https://doi.org/10.5194/acp-20-3209-2020.

[161] E. Jantsch, T. Koop, Cloud Activation via Formation of Water and Ice on Various Types of Porous Aerosol Particles, ACS Earth Sp. Chem. 5 (2021) 604–617. https://doi.org/10.1021/acsearthspacechem.0c00330.

[162] G. Chaudhary, R. Li, Freezing of water droplets on solid surfaces: An experimental and numerical study, Exp. Therm. Fluid Sci. 57 (2014) 86–93. https://doi.org/10.1016/j.expthermflusci.2014.04.007.

[163] Y. Yao, C. Li, Z. Tao, R. Yang, Numerical simulation of water droplet freezing process on cold surface, ASME Int. Mech. Eng. Congr. Expo. Proc. 8 (2017) 1–8. https://doi.org/10.1115/IMECE2017-71175.

[164] L. Karlsson, A.L. Ljung, T.S. Lundström, Modelling the dynamics of the flow within freezing water droplets, Heat Mass Transf. Und Stoffuebertragung. 54 (2018) 3761–3769. https://doi.org/10.1007/s00231-018-2396-1.

[165] G. Plastiras, C. Kyrkou, T. Theocharides, Efficient convnet-based object detection for unmanned aerial vehicles by selective tile processing, ACM Int. Conf. Proceeding Ser. (2018). https://doi.org/10.1145/3243394.3243692.

[166] G.P. Rutkowski, I. Azizov, E. Unmann, M. Dudek, B.A. Grimes, Microfluidic droplet detection via region-based and single-pass convolutional neural networks with comparison to conventional image analysis methodologies, Mach. Learn. with Appl. 7 (2022) 100222. https://doi.org/10.1016/j.mlwa.2021.100222.

[167] I.M. Weidinger, J. Klein, P. Stöckel, E. Biller, H. Baumgärtel, T. Leisner, The Freezing of n-Alkanes C15H32 and C 17H36 An Unsual Mechanism of Homogeneous Nucleation, Zeitschrift Fur Phys. Chemie. 217 (2003) 1597–1611. https://doi.org/10.1524/zpch.217.12.1597.20473.

[168] J. Kim, J. Park, H. Shim, K. Koo, Effect of Amphiphilic Additives on Nucleation of Hexahydro-1,3,5-trinitro-1,3,5-triazine, Cryst. Growth Des. 13 (2013) 4688–4694. https://doi.org/10.1021/cg4006423.

[169] D. Duft, T. Leisner, Laboratory evidence for volume-dominated nucleation of ice in supercooled water microdroplets, Atmos. Chem. Phys. 4 (2004) 1997–2000. https://doi.org/10.5194/acp-4-1997-2004.

[170] J. Bergfreund, P. Bertsch, S. Kuster, P. Fischer, Effect of Oil Hydrophobicity on the Adsorption and Rheology of β-Lactoglobulin at Oil-Water Interfaces, Langmuir. 34 (2018) 4929–4936. https://doi.org/10.1021/acs.langmuir.8b00458.

[171] F. Staniscia, H. V. Guzman, M. Kanduč, Tuning Contact Angles of Aqueous Droplets on Hydrophilic and Hydrophobic Surfaces by Surfactants, J. Phys. Chem. B. 126 (2022) 3374–3384. https://doi.org/10.1021/acs.jpcb.2c01599.

[172] A.D. Gonçalves, C. Alexander, C.J. Roberts, S.G. Spain, S. Uddin, S. Allen, The effect of protein concentration on the viscosity of a recombinant albumin solution formulation †, (2016). https://doi.org/10.1039/c5ra21068b.

[173] M. Rabe, A. Kerth, A. Blume, P. Garidel, Albumin displacement at the air–water interface by Tween (Polysorbate) surfactants, Eur. Biophys. J. 49 (2020) 533–547. https://doi.org/10.1007/s00249-020-01459-4.

[174] M. Loretan, I. Domljanovic, M. Lakatos, C. Rüegg, G.P. Acuna, DNA origami as emerging technology for the engineering of fluorescent and plasmonic-based biosensors, Materials (Basel). 13 (2020). https://doi.org/10.3390/ma13092185.

[175] R.M. Zadegan, M.L. Norton, Structural DNA nanotechnology: From design to applications, Int. J. Mol. Sci. 13 (2012) 7149–7162. https://doi.org/10.3390/ijms13067149.

[176] K.E. Dunn, F. Dannenberg, T.E. Ouldridge, M. Kwiatkowska, A.J. Turberfield, J. Bath, Guiding the folding pathway of DNA origami, Nature. 525 (2015) 82–86. https://doi.org/10.1038/nature14860.

[177] A. Rajendran, M. Endo, H. Sugiyama, Dna origami: Synthesis and self-assembly, Curr. Protoc. Nucleic Acid Chem. 1 (2012) 1–18. https://doi.org/10.1002/0471142700.nc1209s48.

[178] H. Chen, T.W. Weng, M.M. Riccitelli, Y. Cui, J. Irudayaraj, J.H. Choi, Understanding the mechanical properties of DNA origami tiles and controlling the kinetics of their folding and unfolding reconfiguration, J. Am. Chem. Soc. 136 (2014) 6995–7005. https://doi.org/10.1021/ja500612d.

[179] S.M. Douglas, A.H. Marblestone, S. Teerapittayanon, A. Vazquez, G.M. Church, W.M. Shih, Rapid prototyping of 3D DNA-origami shapes with caDNAno, Nucleic Acids Res. 37 (2009) 5001–5006. https://doi.org/10.1093/nar/gkp436.

[180] S.M. Douglas, H. Dietz, T. Liedl, B. Högberg, F. Graf, W.M. Shih, Self-assembly of DNA into nanoscale three-dimensional shapes, Nature. 459 (2009) 414–418. https://doi.org/10.1038/nature08016.

[181] C.E. Castro, F. Kilchherr, D.N. Kim, E.L. Shiao, T. Wauer, P. Wortmann, M. Bathe, H. Dietz, A primer to scaffolded DNA origami, Nat. Methods. 8 (2011) 221–229. https://doi.org/10.1038/nmeth.1570.

[182] K.G. Young, B. Najafi, W.M. Sant, S. Contera, A.A. Louis, J.P.K. Doye, A.J. Turberfield, J. Bath, Reconfigurable T-junction DNA Origami, Angew. Chemie. 132 (2020) 16076–16080. https://doi.org/10.1002/ange.202006281.

[183] E. Benson, R. Carrascosa Marzo, J. Bath, A.J. Turberfield, Strategies for Constructing and Operating DNA Origami Linear Actuators, Small. 17 (2021) 1–8. https://doi.org/10.1002/smll.202007704.

[184] E. Silvester, B. Vollmer, V. Pražák, D. Vasishtan, E.A. Machala, C. Whittle, S. Black, J. Bath, A.J. Turberfield, K. Grünewald, L.A. Baker, DNA origami signposts for identifying proteins on cell membranes by electron cryotomography, Cell. 184 (2021) 1110-1121.e16. https://doi.org/10.1016/j.cell.2021.01.033.

[185] E. Benson, R.C. Marzo, J. Bath, A.J. Turberfield, A DNA molecular printer capable of programmable positioning and patterning in two dimensions, Sci. Robot. 7 (2022) 1–9. https://doi.org/10.1126/scirobotics.abn5459.

[186] M.A.B. Baker, A.J. Tuckwell, J.F. Berengut, J. Bath, F. Benn, A.P. Duff, A.E. Whitten, K.E. Dunn, R.M. Hynson, A.J. Turberfield, L.K. Lee, Dimensions and Global Twist of Single-Layer DNA Origami Measured by Small-Angle X-ray Scattering, ACS Nano. 12 (2018) 5791–5799. https://doi.org/10.1021/acsnano.8b01669.

[187] F. Benn, N.E.C. Haley, A.E. Lucas, E. Silvester, S. Helmi, R. Schreiber, J. Bath, A.J. Turberfield, Chiral DNA Origami Nanotubes with Well-Defined and Addressable Inside and Outside Surfaces, Angew. Chemie. 130 (2018) 7813–7816. https://doi.org/10.1002/ange.201800275.

[188] V. Korpelainen, V. Linko, J. Seppä, A. Lassila, M.A. Kostiainen, DNA origami structures as calibration standards for nanometrology, Meas. Sci. Technol. 28 (2017). https://doi.org/10.1088/1361-6501/28/3/034001.

[189] D.N. Kim, F. Kilchherr, H. Dietz, M. Bathe, Quantitative prediction of 3D solution shape and flexibility of nucleic acid nanostructures, Nucleic Acids Res. 40 (2012) 2862–2868. https://doi.org/10.1093/nar/gkr1173.

[190] J. Bush, S. Singh, M. Vargas, E. Oktay, C.-H. Hu, R. Veneziano, Synthesis of DNA Origami Scaffolds: Current and Emerging Strategies, Molecules. 25 (2020) 3386. https://doi.org/10.3390/molecules25153386.

[191] T. Watanabe, Y. Sato, H. Otaka, I. Kawamata, S. Murata, S.I.M. Nomura, DNA origami “quick” refolding inside of a micron-sized compartment, Molecules. 25 (2020) 1–10. https://doi.org/10.3390/molecules25010008.

[192] B. Cayrol, F. Geinguenaud, J. Lacoste, F. Busi, J. Le Dérout, O. Piétrement, E. Le Cam, P. Régnier, C. Lavelle, V. Arluison, Auto-assembly of E. coli DsrA small

noncoding RNA: Molecular characteristics and functional consequences, RNA Biol. 6 (2009) 434–445. https://doi.org/10.4161/rna.6.4.8949.